SINGLE PION PRODUCTION WITH FORWARD - GOING NUCLEONS, IN π^-P INTERACTIONS IN THE RANGE 670 TO 1300 MEV/C

JAMES ROGER HOLMES

A Thesis submitted for the Degree of

DOCTOR OF PHILOSOPHY

in the

UNIVERSITY OF LONDON

Physics Department,
Imperial College,
London, S.W.7.

January, 1972.

ABSTRACT

A description is presented of a general 'missing mass' type of experiment used to study π^-p interactions, concentrating here on single pion production processes in the incident momentum range from 670 to 1300 Mev/c.

The experiment involved the detection and the identification of those recoiling nucleons which were produced in a small forward cone of angles about the incident beam axis. The dipion system was also identified (in a decay array sensitive to both charged and neutral particles), and its missing mass calculated by measuring the incident pion momentum and the nucleon time-of-flight in the final state.

Although it has been the aim to provide a self-contained description of the experiment, most emphasis has been laid on the analysis and interpretation of the data, with which the author was primarily concerned, while only a general outline of the experimental design and characteristics has been presented.

The most prominent features observed in the data were two enhancements in the $\pi^-\pi^0 p$ final state, at incident momenta of 755 and 1070 Mev/c. Various interpretations of the enhancements have been discussed.

ACKNOWLEDGEMENTS

I would like to take this opportunity to thank Professors C.C.Butler and P.T.Mathews for the pleasure of partaking in the research of the High Energy Physics Group at Imperial College; and to thank the Science Research Council for their support during the three years of my research.

I wish to thank, as strongly as ever I can, both my supervisor, Dr.D.A.Garbutt, and my Group Leader, Dr.D.M.Binnie, for their continued help and guidance; I owe a considerable debt of gratitude to them both.

I also extend my gratitude to all my colleagues at both Imperial College and the Rutherford Laboratory for much encouragement, and many informative and helpful discussions: to Dr.S.L.Baker, Dr.L.Camilleri, Mr.A.Duane, Mr.R.J.Gray, Mr.R.F.Hobbs, Dr.W.G.Jones, Mr.J.Keyne, Dr.M.Lewis, Mr.D.Miller, Mr.D.J.Scholes, Dr.I.Siotis, and Dr.P.N.Upadhyay.

Finally, and most important to me, I want to thank my wife, Pamela, for her unselfish encouragement and endurance.

CONTENTS

Chapter One

An outline of the experiment.

1.1 Introduction.

Most of the established baryon resonances have been detected in direct s-channel "formation experiments", in which a nucleon target is bombarded by a beam of pions or kaons at several closely-spaced incident momenta. When the total energy in the centre-of-mass of this initial system coincides with the mass of a baryon resonance, the presence of the latter may be detected by a suitable analysis of any of the final states corresponding to its decay modes. The analysis may simply consist of observing enhancements in the cross-sections for these final states, or may involve a more sophisticated approach - as in phase shift analysis.

On the other hand, the restriction of practical experiments to nucleon targets has meant that, to date, the formation of meson resonances has been possible in only two types of interaction. In the first, experiments involving intersecting electron - positron beams have been used to detect the formation of vector mesons; in the second, searches for mesons with masses greater than twice that of the proton have been made, using antiproton - proton collisions. Because of these limitations, the spectrum of meson resonances has been studied extensively in "production experiments". Here the presence of a meson is observed as an enhancement in either the effective mass of a particular group, or in the missing mass of a general group of particles in a multi-body final state.

In particular, the technique of missing mass spectroscopy has been developed in "counter experiments" where there is a high degree of statistical accuracy. In 1966 the Counter Group at Imperial College proposed such an experiment: a search for meson resonances, $X^{\bar{o}}$, present in reactions of the type $\pi^- + p \longrightarrow X^{\bar{o}} + N$, would be undertaken in the following way. The incident momentum of the pion would be varied in closely-spaced intervals; at each momentum, recoiling nucleons, N, produced close to threshold, would be detected and timed over a known distance. A resonance would be seen as a systematic variation in the number of detected nucleons (section 1.2). The advantages would include the simultaneous measurement of proton and neutron channels - so that a search for charged and neutral mesons was feasible - and the identification of the decay products of the meson in a complex array of counters. Minor modifications have been made to the original design, but data was essentially taken with the same instrument over a period of months, ending in September, 1970. The incident momentum range covered was 670 to 4000 Mev/c (a missing mass range of 540 to 1960 Mev/c^2). Details of various completed analyses are given in reference 1.

This thesis is concerned with single pion production, and in particular with the $\pi^-\pi^o p$ and $\pi^+\pi^- n$ channels, at the lowest momenta available in the data. In this region nucleon resonances are known to have significant branching ratios to these particular final states.

Results are presented in the form of "yield curves" (section 1.2), any structure in which may be interpreted as either nucleon or meson resonance behaviour.

1.2 Missing Mass Spectroscopy and the Yield Curve.

The yield curve technique is a variation of the well-established method of missing mass spectroscopy advanced by Maglic (2). Consider a quasi-two-body process

$$1 + 2 \longrightarrow X + 4$$

where 1,2 and 4 are stable particles (not resonances), and X is in general a system of particles. The missing mass of this system of particles, M, is given by

$$M^2 = (E_1 + E_2 - E_4)^2 - (\underline{p}_1 + \underline{p}_2 - \underline{p}_4)^2 \qquad \text{...........(1.1)}$$

where E_i is the total energy, and $\underline{p}_i$ the momentum of particle i. At a fixed incident momentum $\underline{p}_1$, and with X representing a system of uncorrelated particles, the distribution of M^2 will be smooth and slowly-varying. However, should X represent the decay products of a resonance of mass M_X , there will be a peak in the M^2 distribution at a mass $M = M_X$. This forms the basis of all missing mass experiments.

Consider explicitly the present experiment, where particle 1 is a pion incident on particle 2, which is a proton at rest, with particle 4 the recoiling nucleon, N. Equation (1.1) then reduces to the following:

$$M^2 = (E + m_p - E_N)^2 - p^2 - p_N^2 + 2pp_N\cos\theta \qquad \text{...........(1.2)}$$

where E, p and E_N, p_N are the energy and momentum of the incident pion and the recoiling nucleon respectively; m_p is the mass of the proton; and θ is the angle between the pion and the nucleon (all variables measured in the laboratory system). Obviously, at a fixed incident momentum, simultaneous measurements of p_N and θ are sufficient to determine M. However, to obtain a yield curve, a 'scan' in incident momentum is required, over a range of values of p: in general, therefore,

$$M = M(p , \theta , p_N)$$

where $p_N = p_N(t)$, if t is the nucleon time-of-flight.

The sensitivity, dM, of the determination of M depends on the precision with which the three variables are measured:

$$(dM)^2 = (\frac{\partial M}{\partial p}.dp)^2 + (\frac{\partial M}{\partial \theta}.d\theta)^2 + (\frac{\partial M}{\partial p_N}.dp_N)^2 \qquad ....(1.3)$$

where, by differentiating equation (1.2),

$$\begin{aligned} M\frac{\partial M}{\partial p} &= -\beta(E_N - m_p) + p_N.\cos\theta \\ M\frac{\partial M}{\partial \theta} &= -\ p.p_N.\sin\theta \qquad ....(1.4) \\ M\frac{\partial M}{\partial p_N} &= -\beta_N(E + m_p) + p.\cos\theta \end{aligned}$$

with β, and β_N the velocities of the pion and nucleon respectively. For a given systematic precision $d\theta$ of the measurement of θ, $\partial M/\partial\theta.d\theta$ can be made to vanish if $\partial M/\partial\theta = 0$. From equations (1.4) this occurs at $\theta = 0$. Similarly, for a given systematic precision dp_N of the measurement of p_N , $\partial M/\partial p_N . dp_N$ vanishes when $\partial M/\partial p_N = 0$. If $\theta = 0$ this can be satisfied when

$$p - \beta_N(E + m_p) = 0$$

or, $\qquad\qquad\qquad\qquad$ ....(1.5)

$$\beta_N = \frac{p}{E + m_p} = \beta_c$$

where β_c is the velocity of the centre-of-mass in the laboratory system. $\beta_N = \beta_c$ corresponds to the nucleon being produced at rest in the centre-of-mass system (the c-system). With the conditions $\theta = 0$ and $\beta_N = \beta_c$, the resolution of the missing mass determination is then solely governed by the precision dp of the measurement of the incident beam momentum:

$$dM = \partial M/\partial p \ . \ dp$$

This experiment was therefore designed to operate as follows: a beam of negatively charged pions was incident upon a hydrogen target; the beam had a precisely defined momentum. A series of neutron counters, arranged symmetrically about the beam axis, was used to detect recoiling nucleons scattered into a small forward cone of angles $\theta \simeq 0$ about the axis. The nucleon times-of-flight were recorded, so that in a subsequent data analysis, events for which the nucleon had a velocity $\beta_N \cong \beta_c$ could be selected. In this way the resolution of the missing mass determination was optimized at each incident momentum.

The remaining products of the interaction were detected by an array of counters sensitive to both charged and neutral particles; for each detected nucleon, the state of this array was also recorded. Such a flexible system enabled several final states to be identified and studied simultaneously. During data analysis, histograms of the time-of-flight of the nucleons for various states of the decay array were made; these could be combined in a suitable fashion to represent the time-of-flight spectra of particular final states of interest. As an example, Fig.1.1A shows the spectrum of the $\pi^+\pi^-\pi^0 n$ final state, at an incident momentum of 1125 Mev/c. As the time-of-flight t is related to the missing mass M by equation (1.2) with $p_N = p_N(t)$, an enhancement in the missing mass distribution will also be present in the time-of-flight spectrum. Thus, the ω meson produced in the reaction $\pi^- + p \longrightarrow \omega + n$, $\omega \rightarrow \pi^+\pi^-\pi^0$, is seen as an enhancement in Fig.1.1A.

The yield in a fixed timing gate (interval of time) is the number of recoiling nucleons with times-of-flight within that gate: this number is usually normalized to a rate of 100 million incident pions. The yield curve is generated by plotting the yield in a given gate as a function of incident momentum. The rise and fall of a cross-section through resonance production is reflected as structure in such a curve. And since background subtraction is simpler in this case, the yield curve is preferred to a time-of-flight spectrum for the extraction of the mass and width parameters of the resonance. As an example, Fig.1.1B shows the yield curve of the $\pi^+\pi^-\pi^0 n$ final state, for yields in the gate shown in Fig.1.1A. The ω meson is seen as

1.1(A)

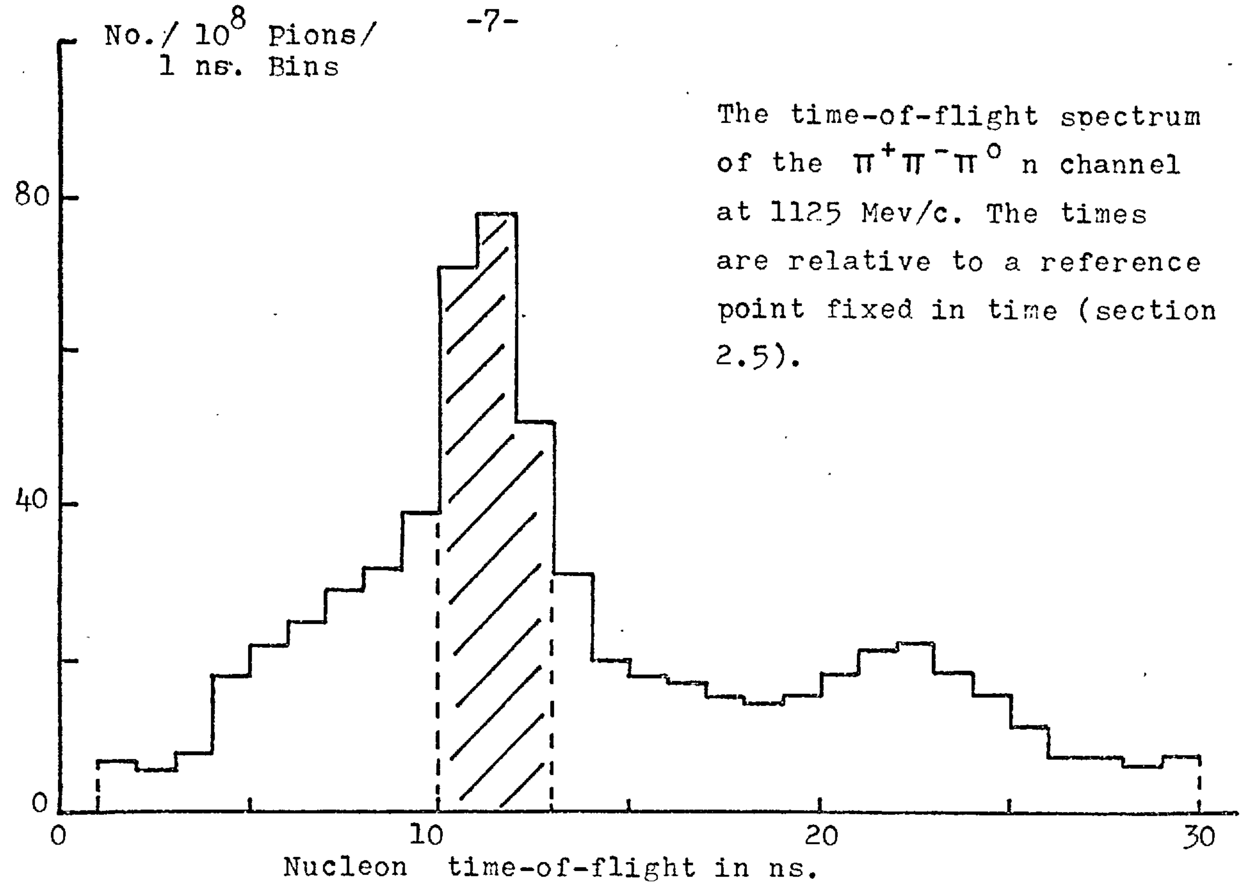

The time-of-flight spectrum of the $\pi^+\pi^-\pi^0$ n channel at 1125 Mev/c. The times are relative to a reference point fixed in time (section 2.5).

1.1(B)

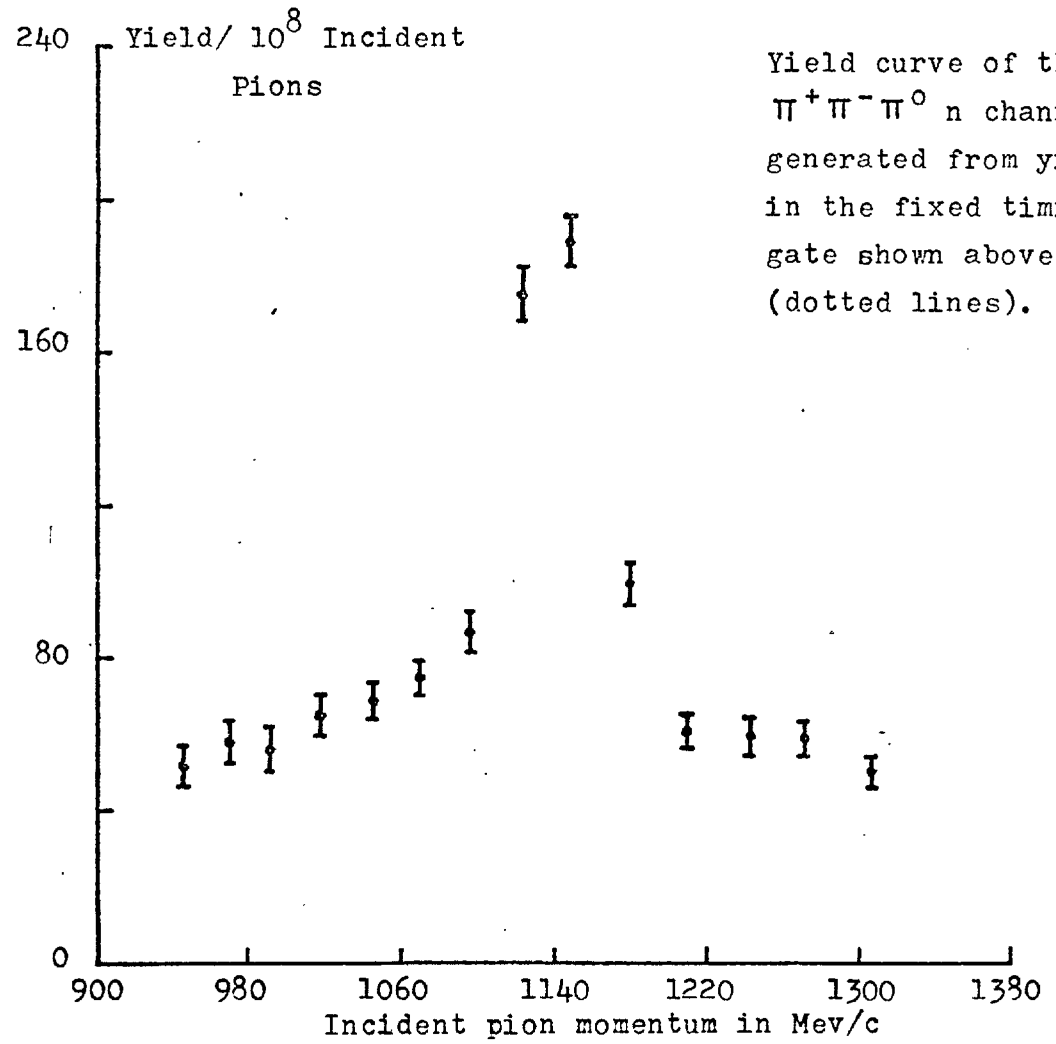

Yield curve of the $\pi^+\pi^-\pi^0$ n channel, generated from yields in the fixed timing gate shown above (dotted lines).

FIG. 1.1

a strong enhancement. From such curves the mass and width of the resonance can be obtained.

A slight variation in the technique of analysis leads to a presentation of the data in the form of mass plots. This technique emphasizes how the yield curve is, in fact, equivalent to a continuous mass spectrum. Essentially the yield in a fixed gate t_2-t_1 is redistributed into mass bins by using equation (1.2). Thus, at a fixed incident momentum, there exist times T and T+dT corresponding to missing masses M and M-dM, such that the events in the time interval are those with masses in the mass interval. A mass spectrum restricted to the range $m_2 < M < m_1$ can be produced from the events in the gate t_2-t_1 : if $N(T_1,T_2)$ is the number of events in the gate T_2-T_1 , then, in an obvious notation:

$$
\begin{array}{lll}
m_1 \equiv T_1 \geq t_1 & & \\
m_1 - dm \equiv T_1+dT_1 = T_2 & : N(T_1,T_2) & = N(m_1,m_1-dm) \\
m_1-2dm \equiv T_2+dT_2 = T_3 & : N(T_2,T_3) & = N(m_1-dm,m_1-2dm)
\end{array}
$$

$$
m_2 = m_1-ndm \equiv T_n+dT_n = T_{n+1} \leq t_2 : N(T_n,T_{n+1}) = N(m_2+dm,m_2)
$$

A slightly increased incident momentum produces a displaced but overlapping spectrum of masses; but by adding such spectra together, with suitable normalization, a continuous mass distribution is achieved. In this way, by actually performing a scan over closely-spaced intervals of incident momentum, a continuous missing mass spectrum can be "simulated".

This method is illustrated in Fig.1.2, where again the final state is $\pi^+\pi^-\pi^0$ n, and the ω seen as a strong enhancement.

Using both the yield curve and mass plot techniques, the mass of the ω meson has been estimated (1c): from the yield curve a value of 782.1 $\pm$ 0.5 Mev/c^2 was obtained; from the mass plot, 782.7 $\pm$ 0.5 Mev/c^2. The width of the ω was estimated to be 9.7 $\pm$ 1.3 Mev/c^2 from the mass plot.

1.3 The Kinematics of Meson Resonance Production.

The kinematic relation between incident momentum p, missing mass M, and the nucleon time-of-flight t, can be shown diagramatically. Thus the kinematics curves of Fig.1.3 show typical missing mass contours in the p - t plane.

Of particular importance is the yield in a small time interval around $t = t_c$, where $t_c = t_c(p)$ is the time-of-flight of nucleons having velocities $\beta_N = \beta_c$ (Fig.1.3). Here, for each incident momentum p, there exist almost unique values of M, since $\partial M/\partial t = 0$ (see section 1.2):

$$M(p, t \simeq t_c) = M(p, t = t_c) + \left(\frac{\partial M}{\partial t}\right)_{t = t_c} . dt + \ldots.$$

$$\simeq M(p, t = t_c)$$

$$= M_{max}(p) \quad \text{(see Fig.1.3)}$$

Working at $t = t_c(p)$, therefore, is equivalent to being at the tip of a Dalitz plot with M^2 as ordinate ($M \equiv M_{\pi\pi}$ for single pion production modes). As the momentum is increased, the

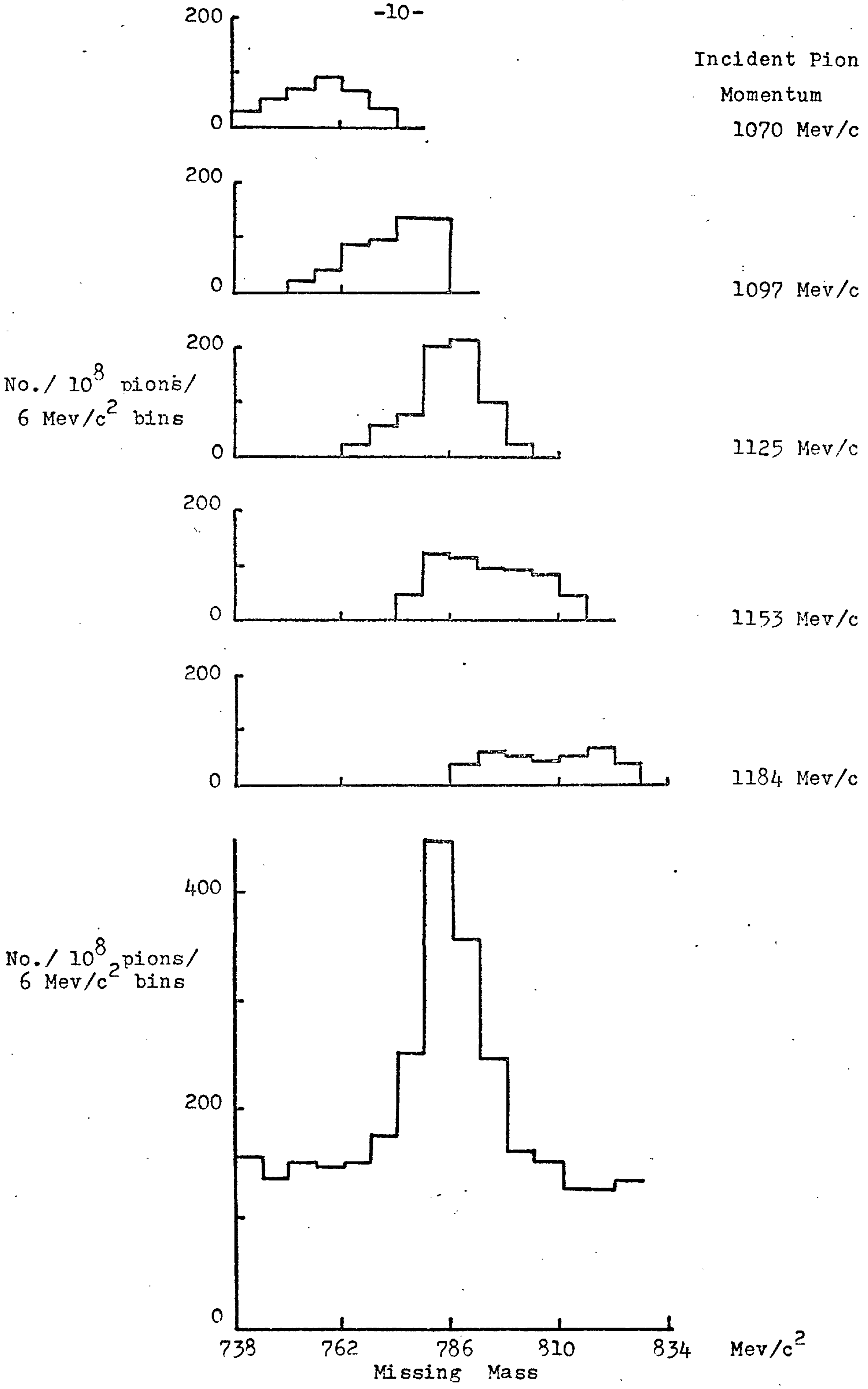

FIG 1.2 : 'Building-up' a mass-plot.
Individual mass spectra obtained from the data in a fixed timing gate at several incident momenta are added and normalized to give a continuous mass spectrum.

FIG. 1.3

The Kinematics Curves

Contours of the Missing Mass (M) in the p - t plane

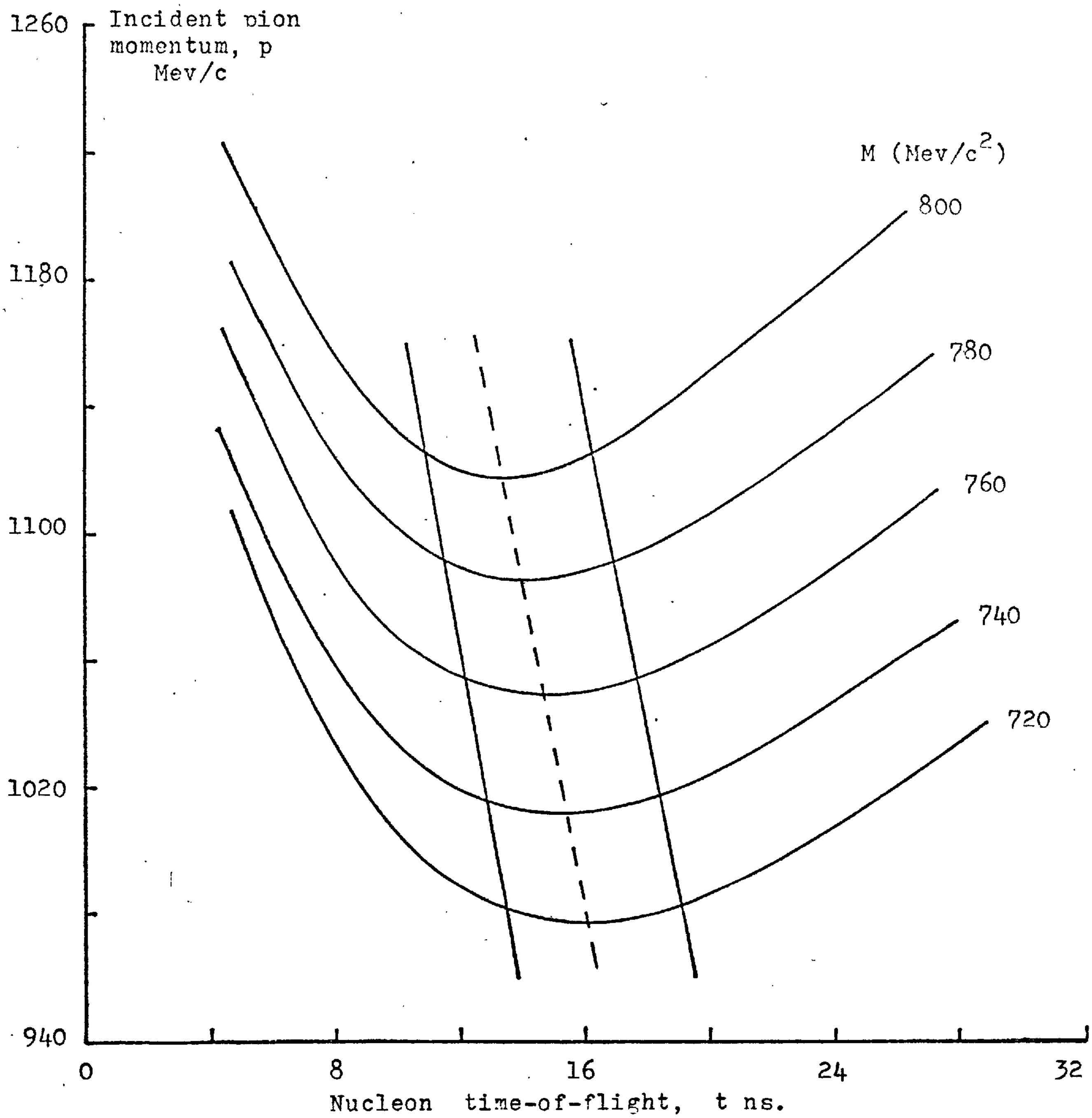

The diagonal solid lines show the limits of the 'cms gate' (section 1.4.1), and the dotted line is $t = t_c(p)$, the time-of-flight locus corresponding to centre-of-mass velocities β_c. The times-of-flight are measured relative to a fixed reference point (section 2.5).

Dalitz boundary expands so that higher and higher values of M^2 are possible. At each momentum, the yield in the gate at $t = t_c$ is proportional to the density of states at the tip of the Dalitz Plot: as the momentum is varied, a peak will occur in the yield curve corresponding to the production of a resonance of mass M_X at a momentum $p = p_c$ for which

$$M_X = M(p_c , t_c)$$

The kinematics curves show that this momentum is the lowest possible required to produce a mass of M_X : the resonance is produced at threshold. When this happens, the nucleon is produced at rest in the c-system, and its resulting motion in the laboratory is therefore directed towards the detectors at $\theta \simeq 0$. In consequence, there is a high collection efficiency for such nucleons. Very close to threshold it has been shown (3) that nucleons emitted at all angles θ^* in the c-system are detected.

As the momentum is increased to some value $p = p_o > p_c$, there now exist two times-of-flight of the nucleon which correspond to the production of the missing mass M_X : $t_1 < t_c$ and $t_2 > t_c$ (Fig.1.4). In both cases the nucleon now has a non-zero kinetic energy in the c-system. However, only those produced backwards (at $\theta^* \simeq 180^\circ$) are detected at t_1; only those produced forwards (at $\theta^* \simeq 0^\circ$) are detected at t_2 (3) . The collection efficiency of events with a missing mass equal to the resonance mass M_X therefore decreases as the momentum is increased above the corresponding threshold value p_c.

In the time-of-flight spectrum produced at a momentum $p = p_c$, there will be a single enhancement at a time $t = t_c$, corresponding to the production of the resonance of mass M_X : at a higher momentum p_o , there will be two enhancements in the spectrum at t_1 and t_2. Thus the two enhancements seen in the time-of-flight spectrum of Fig.1.1A both represent ω production - at an incident momentum above its threshold.

Such an effect can be exploited using the 'yield curve technique': thus in the yield curve generated from the gate at $t = t_c$, structure due to the production of the meson resonance (M_X) should occur at an incident momentum $p = p_c$; in the curve generated from a gate at $t = t_1$ (or t_2), the structure should be at $p = p_o$. By a suitable choice of t_1, this change in the position of the structure, p_o-p_c , can be made large enough to be observable. So by generating curves of the yields in suitable timing gates, it is possible to demonstrate whether or not observed structure in such curves behaves in a manner consistent with its interpretation as meson resonance production. This principle is clearly demonstrated in Fig.1.4. Here the contour of $M = M_X = M_\omega$ is drawn in the t - p plane, and shown together with the observed yield curves of the $\pi^+\pi^-\pi^o n$ channel, generated from the yields in the two different gates shown on the t-axis. A peak due to ω production is observed, at different momenta in the two curves: the relative displacement of the peaks is (approximately) as predicted by the kinematics curve.

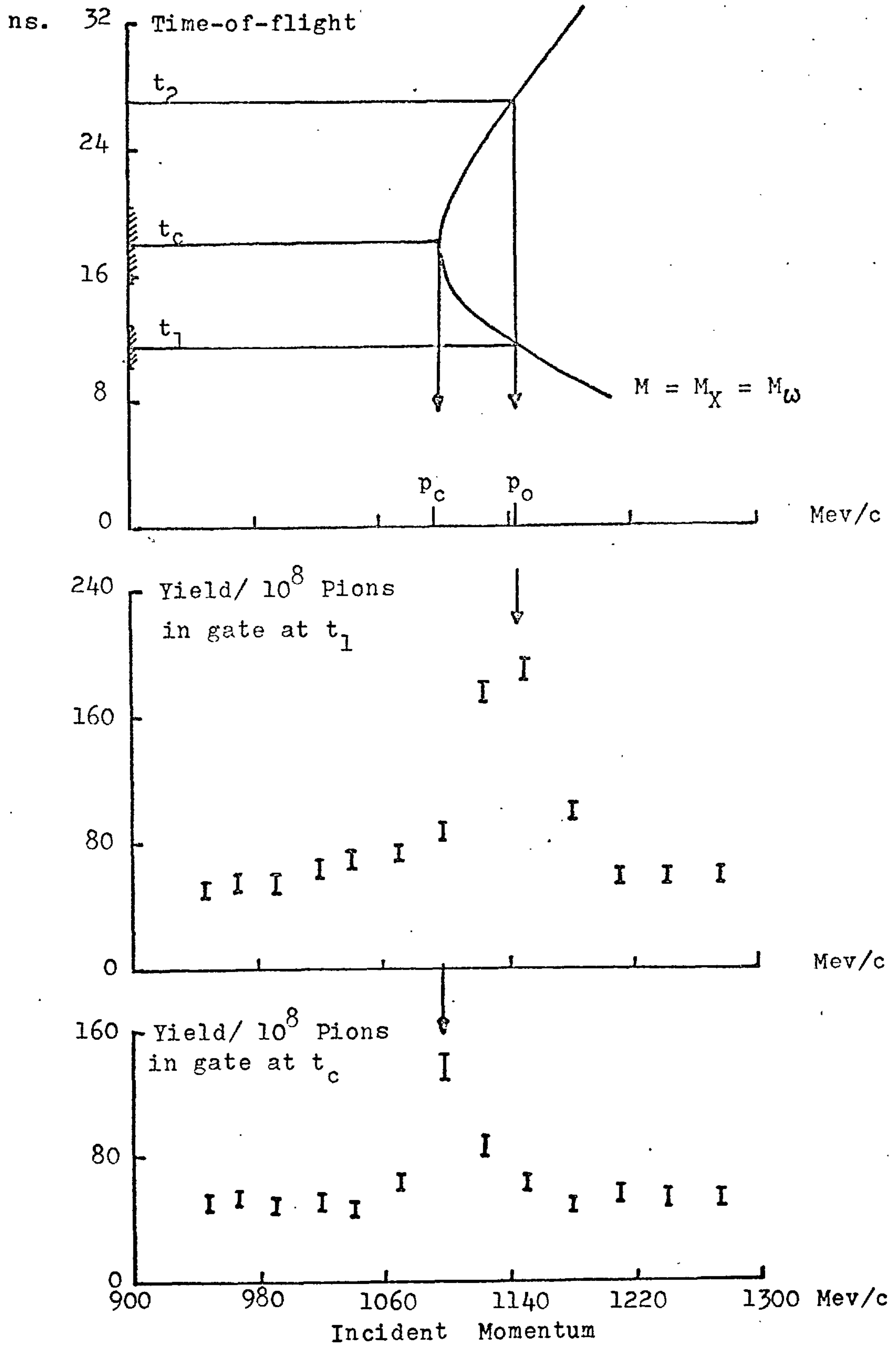

FIG. 1. 4

Yield curves of the $\pi^+\pi^-\pi^0$ n channel, generated from two different timing gates (shown as the shaded regions on the time-of-flight axis in the top graph).

1.4 The choice of timing gates in the practical application of the yield curve technique.

It was seen in the preceding section that systematic variations in the position of structure, present in yield curves obtained from different timing gates, could be related to meson production. The exact form, and the limitations on the choice of such gates, imposed by practical considerations, is now discussed.

1.4.1 The centre-of-mass sliding gate (the cms gate).

In section 1.2 it was shown that the determination of the missing mass is independent of the precision with which the direction, θ, and momentum, $p_N(t)$, are measured, for nucleons detected at $\theta = 0$ with velocities $\beta_N = \beta_c$. In this experiment, nucleons were detected at small angles $\theta \simeq 0$; so a gate selecting those with velocities $\beta_N \simeq \beta_c$ suggested itself - allowing a mass determination with optimum resolution to be made at each momentum. A gate centred on the time t_c was therefore chosen; since t_c is a function of the incident momentum p, the position of the centre of the gate changed at each new value of p. In practice, the width of the gate was also made a function of p. This ensured that the number of events in the gate did not vary too rapidly as the incident momentum was changed: if this were to happen, it would make background subtraction more difficult. (As the momentum is increased, more nucleons are detected close to threshold, so the gate was made to contract.) The gate limits t_{1c} and t_{2c} then had the following form:

$$t_{1c} = t_c(p) - F(p)$$
$$t_{2c} = t_c(p) + G(p)$$

where F and G were positive, linear functions of p, empirically chosen from studies of other channels. However, the same gate was adopted for this study of single pion production processes as it provided a twofold advantage: firstly, the observed yield curves generated from the gate were relatively slowly-varying, which would facilitate accurate background subtraction; secondly, the predicted geometric acceptance of nucleons with times-of-flight in this gate (as furnished by the 3-body phase space simulation described in section 4.3) is independent of incident pion momentum. This gate is referred to throughout the text as the "cms gate": the limits of the gate are shown in Fig.1.3.

1.4.2 Other timing gates.

For gates at times $t < t_c$, the kinematics curves show that $\partial M/\partial t$ rises rapidly. In this region the mass resolution is dominated by $\partial M/\partial t.dt$, where dt is the intrinsic electronic timing resolution, systematic to the experiment; (dt is approximately $\pm$ 0.6 ns.). The mass resolution therefore becomes increasingly worse as gates at shorter times-of-flight are chosen. The contribution to the resolution due to the finite size of the neutron counters, $d\theta$, is negligible at all times-of-flight.

The mass resolution versus time-of-flight curve for neutron channels at an incident momentum of 1.1 Gev/c has been calculated in reference 1c. In the region of the cms gate where the resolution is dominated by the precision of the incident momentum measurement, it is of the order of $\pm$ 2 to 3 Mev/c^2 (standard deviation).

For proton channels, gates chosen at times $t > t_c$ have the additional problem due to the proton energy loss in ionising collisions in the target. This requires a correction to the raw time-of-flight depending on the position of the interaction vertex; any uncertainty in this position leads to an error in the missing mass determination. This problem is discussed further in section 4.5.2.

In general, therefore, the choice of gates is practically restricted; on the $t < t_c$ side for both proton and neutron final states due to the electronic timing precision; on the $t > t_c$ side for proton final states due to the uncertainty in the position of the interaction vertex. Within the range governed by these limitations, all other gates used in the analysis were fixed in time, and chosen for two main reasons:

(1) to distinguish between nucleon and meson resonances by observing the behaviour of enhancements in yield curves generated from the yields in different timing gates, as outlined in the next section;

(2) the time-of-flight t is related to the 4-momentum transfer Δ^2 by the equation:

$$\Delta^2 = (p_N - p_p)^2$$

where p_N and p_p are the 4-momenta of the final state nucleon and the initial state proton respectively: this can be expressed as

$$\Delta^2 = -2T_N m_p + (m_N - m_p)^2$$

$$\simeq -2T_N m_p$$

with T_N the kinetic energy of the recoiling nucleon, directly related to the time-of-flight t. So changing the timing gate allows a study of possible differences in behaviour of any structure in the yield curve to be made as a function of 4-momentum transfer.

1.5 Limitations of the Experiment.

So far the apparatus has been reviewed as a means of experimentally detecting meson resonances: the hope is to assign mass and width values to each resonance. To achieve this end, two main problems must be overcome during the data analysis: any structure present in the yield curve must be identified as being due to meson production - rather than to some spurious instrumental effect, or nucleon resonance formation; and it must be possible to parametrize and remove the background under the structure, leaving the resonance whose mass and width are to be established.

In general, the yield curve technique is most effective in the study of narrow resonances. Here the background is relatively easy to remove, so that accurate measurements of masses and widths can follow (cf. the result of reference 1c). The subtraction of background under resonances with large widths is, however, much more speculative, and must be undertaken with a great deal of care (cf. the results of references 1a and 1b). This problem is, of course, common to the analyses of many experiments in high energy physics today, and often results in only tentative estimates of the resonance parameters being deduced (cf. the results of elastic phase shift analyses (4)).

The formation of nucleon resonances is another problem of particular significance in the momentum range discussed here, as many are known to exist, and to have large branching ratios to the single pion production channels (5). Thus the formation of N^* or Δ -resonances in reactions of the type

$$\pi^- + p \rightarrow N^* \rightarrow \pi\pi N \qquad \ldots\ldots\ldots\ldots\ldots\ldots\ldots (1A)$$

will give rise to the same final states as meson production in reactions like, for example,

$$\pi^- + p \longrightarrow \rho + N \quad , \rho \longrightarrow \pi\pi \qquad \ldots\ldots\ldots\ldots\ldots (1B)$$

The formation of nucleon resonances can be expected to manifest itself in the yield curve, since such a curve is obtained by varying the incident pion momentum p in what is essentially a scan over the centre-of-mass energy E^*. This can be understood by assuming a cross-section for reaction (1A) of the form

$$\sigma \propto \frac{A}{A + (E^* - M_s)^2} \quad , \quad A = (\Gamma_s/2)^2$$

where M_s and Γ_s are the mass and width of the nucleon resonance, and $E^* = E^*(p)$. As the incident momentum p is varied so that E^* tends towards the threshold energy, M_s , for reaction (1A), the value of $E^* - M_s$ tends to zero; consequently the cross-section σ rises, and there will be a corresponding rise in the yield of recoiling nucleons. As the threshold energy is passed, the yield will similarly fall in concert with the now diminishing cross-section. Thus a peak will occur in the yield curve at a momentum $p = p_s$, for which $E^*(p_s) = M_s$.

Assuming that the $\pi\pi N$ final state is a system of uncorrelated particles, the $M^2_{\pi\pi}$ distribution at each momentum will be structureless. It follows from equation (1.2) that the nucleon time-of-flight spectrum will also be structureless: only in the generation of the yield curve will any structure be observed, and the presence of the nucleon resonance be detectable. It is the whole time-of-flight spectrum which moves first up and then down again (relatively speaking), as the incident momentum is varied through the threshold for the formation of the nucleon resonance. Thus the position of the structure in the yield curve will be independent of the timing gate chosen for the generation of the curve. Recalling the discussion of section 1.3, this is a different pattern of behaviour to that expected for meson production; in that case, the position of the structure moves from one momentum to another as the timing gate is changed. This difference in behaviour provides a basis for distinguishing between the two types of resonance in a yield curve analysis: it will be discussed in detail in chapter four. It should be added that such a distinction is not wholly independent of the problem of background subtraction mentioned above. This is because discernible movement of the peaks in yield curves of different timing gates depends to a large extent on how accurately the centre of the peaks can be established. This in turn depends on their widths; and if these are large, particularly on the proper subtraction of the background under them.

In summarizing the limitations of the experiment as a means of detecting meson resonances, two other important qualifications must be added. The first is inherent in the particular design of the apparatus; the second is a more general criticism of the missing mass technique.

Firstly, at each incident momentum, the nucleon detected in the final state has a very small momentum in the centre-of-mass (for example nucleons with times-of-flight in the cms gate have momenta less than 40 Mev/c). It follows that a meson resonance, X , produced in the reaction $\pi^- + p \rightarrow X + N$, will only be detected if there exists sufficient cross-section for its production so close to its threshold. In an earlier experiment on the production of the η at threshold, it was shown that the cross-section rose linearly with the momentum of the η (6). While such a result is encouraging, there is no guarantee of its universality. A cross-section dependence on higher powers of the centre-of-mass momentum would make the detection of a meson more difficult so close to its production threshold.

Secondly, missing mass spectroscopy is essentially confined to a search for enhancements on a continuous background; with this approach, some meson states might not appear due to complicated interference effects. In this spirit, Donnachie (7) has likened the missing mass technique to a study of total cross-section curves (like those of Fig.1.5). Thus, while such curves clearly show a good deal of structure, a study of their shapes by itself would fail to reveal the presence of the many nucleon resonances now known to exist. Donnachie contends that, in a similar fashion, new meson resonances might not necessarily be visible with the missing mass technique. Nevertheless, in the continued absence of experiments in which mesons are directly formed in the s-channel (apart from the exceptions given in section 1.1), missing mass spectroscopy remains of paramount importance in the study of the meson spectrum.

1.6 The Single Pion Production Channels.

Looking specifically at the incident momentum range below 1070 Mev/c (i.e. below the ρ threshold), Fig.1.5 shows a compilation (8) of total cross-section measurements for the single pion production channels $\pi^- + p \rightarrow \pi^-\pi^0 p$, $\pi^+\pi^- n$, and $\pi^0\pi^0 n$. A good deal

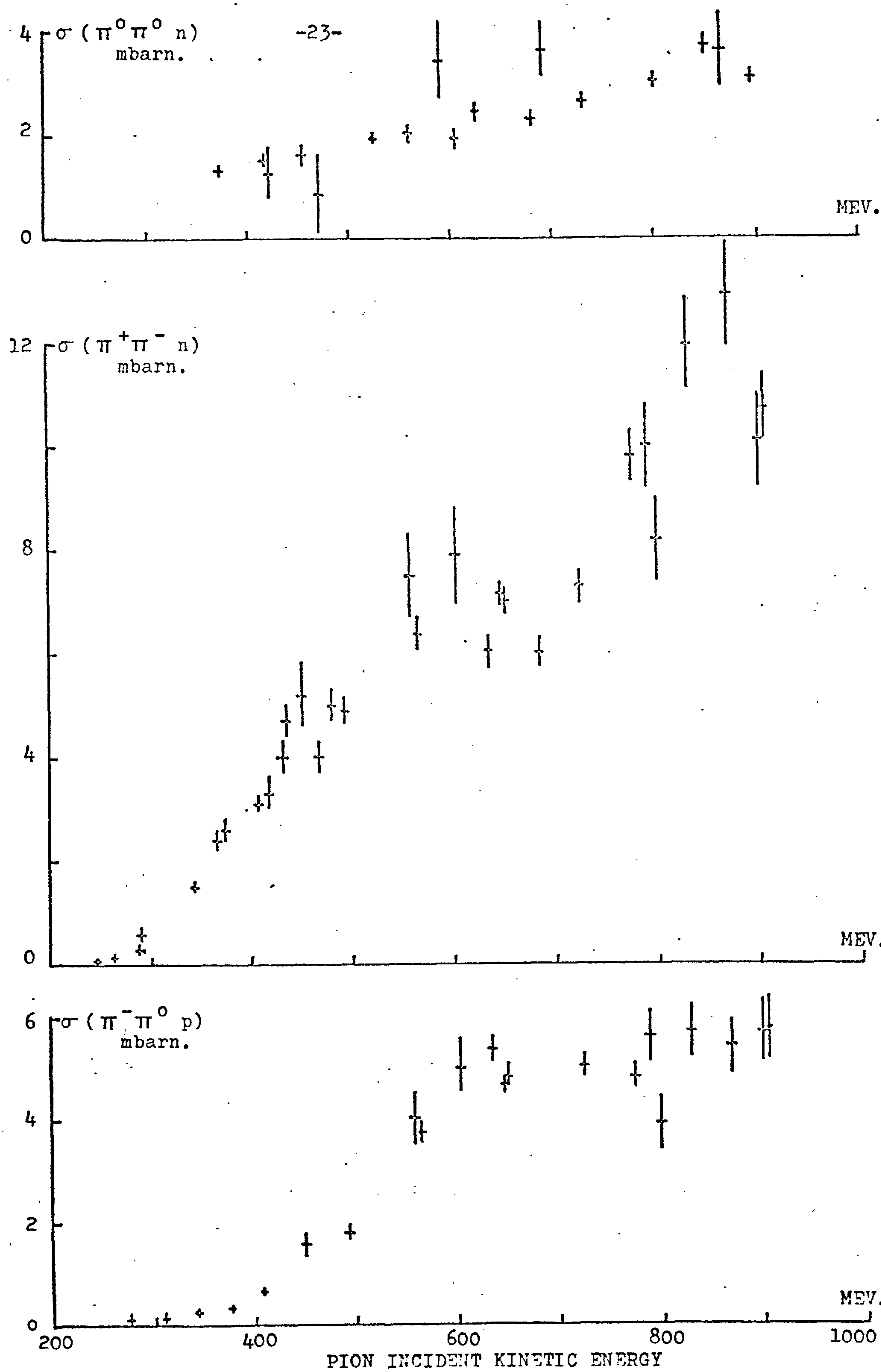

FIG. 1.5 : CROSS-SECTIONS FOR SINGLE PION PRODUCTION IN $\pi^- p$ INTERACTIONS

of broad, overlapping structure is evident. Sophisticated phase shift analyses (9) of elastic scattering data have been required to establish that many nucleon resonances contribute to these total cross-sections. The techniques of analysis favour large widths (10); for the known resonances they are of the order of 100 to 200 Mev/c^2 (5).

Because of the broad nature of these effects, the presence of narrow mesons should still be detectable in this experiment. Ideally, providing there is sufficient cross-section, they should appear as narrow enhancements on the slowly-varying background of the nucleon resonances. Furthermore, by using the technique outlined in section 1.4, it should be possible to distinguish effects produced by narrow mesons from any produced by the recently reported narrow nucleon resonances (10).

While searching the region for narrow resonances, an attempt has also been started to interpret at least the qualitative features of the yield curves - narrow structure apart - in terms of the established nucleon resonances. At first this may seem ambitious, recalling the general criticism of the missing mass technique advanced in the preceding section. It would appear that the criticism is even more pertinent when applied to the study of a region of known overlapping effects by this technique!

On the other hand, the kinematics of the experiment tend to favour the formation of nucleon resonances. Thus, the particles in the final state are separating very slowly (in the region of the cms gate, for example, the nucleons have momenta of less than 40 Mev/c in the centre-of-mass). The particles therefore stay within a typical interaction length ($\hbar$ / $m_{\pi}c$) of each other for a relatively long period on the strong interaction time-scale - a situation which intuitively seems to suit the formation of nucleon resonances. Moreover, because of the collection efficiency of the nucleon detectors, and the selection of events with nucleons of specific times-of-flight, the yield curve actually represents a particular form of differential cross-section measurement. In elastic scattering, it has been useful to study the differential cross-section in the backward direction ($\theta^{*} \approx 180^{\circ}$) because of the sensitivity of backward scattering to phase shifts caused by interference between the various waves (11). Similarly, in the 3-body final state, interference effects are thought to have produced interesting results in this experiment.

Chapter Two

The apparatus and data taking system.

2.1 Introduction.

Two completely independent sets of data were taken with the apparatus. For the first set, the nucleon detection system was placed approximately five metres downstream of the hydrogen target. For the second set, minor modifications and additions were made to improve the overall performance and scope of the apparatus. The detection system was moved a further metre downstream. Throughout the text, the two sets of data are referred to as the 5 and 6 mt. data respectively.

A general review of the main experimental features and the subsequent modifications is presented in this chapter. The arrangement of the counters used in the experiment, together with their relevant design dimensions, is shown in Fig.2.1.

2.2 The Beam and Hydrogen Target.

A high flux beam of negatively charged particles, mainly pions, was produced by bombarding an internal Nimrod target with the circulating proton beam. These particles were extracted, and those in the desired momentum band transported via the π-7 beam-line to a downstream focus on a target of liquid hydrogen.

The lay-out of the beam-line is shown schematically

FIG. 2.1
Schematic diagram of the apparatus

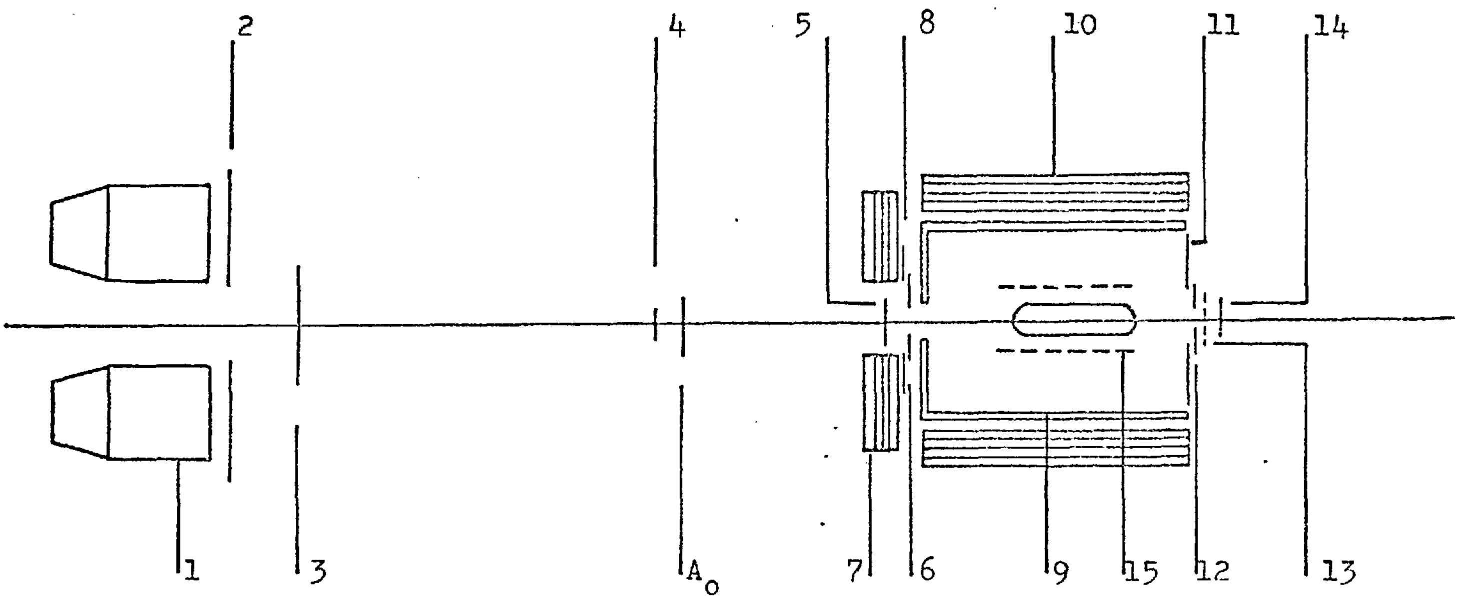

	COUNTER	EFFECTIVE SIZE
1	NEUTRON COUNTER	300 mm ϕ X 300mm LONG
2	VETO A COUNTERS	HEXAGONAL 32 A/F X 9mm THICK
3	VETO A_{O_1} "	CIRCULAR 320 ϕ X 5mm THICK
4	BEAM S_3 "	SQUARE 60mm X 3mm THICK
5	PROTON 'P' "	CIRCULAR 120mm ϕ X 2mm THICK
6	RING COUNTER R_1 & R_2	210mm O/DIA X 100mm I/DIA 5mm THICK.
7	LID γ COUNTERS	20 COUNTERS 18° PITCH SANDWICH CONSTRUCTION 6 LAYER 5mm SCINT 4mm LEAD LEAVING 200mm HOLE.
8	POLAR ANGLE L_1 & L_2 COUNTER	400 O/DIA X 200 I/DIA 7·5mm THICK.
9	INNER CHARGE	19 + 1 SPECIAL 18° PITCH SEGMENT LEAVES 100mm HOLE 10mm THICK 800mm LONG
10	CYLINDER γ COUNTERS	19 + 1 SPECIAL 18° PITCH 6 LAYER SANDWICH 5mm SCINT 4mm LEAD X 800 mm LONG
11	DROOP 1 & 2	580 O/DIA X 160 I/DIA X 10mm THICK
12	A13 COUNTER	190 SQ WITH 40 HORIZ X 42 HIGH HOLE X 5mm THICK
13	'H' HODOSCOPE 7 FINGERS	60 HIGH X 7 52mm X 3mm THICK.
14	'S' COUNTER	55mm SQ X 2mm THICK.
15	TARGET COUNTERS TH_1 - TH_6	RING SHAPED AROUND LH_2 TARGET 130 O/DIA X 3mm THICK X 50 WIDE.

in Fig.2.2: it consisted of two separate stages, each of which comprised a quadrupole doublet and a bending magnet. The purpose of the bending magnets was to provide a beam of particles in the required momentum range, while the pair of quadrupole doublets served to focus the beam on the hydrogen target. To obtain a beam with a central momentum P_0 , the magnet currents were adjusted to values which had been determined during "beam-setting" runs prior to the main experiment. Estimates of these values were initially obtained from standard Rutherford Laboratory programs (12). Exact currents for the magnets in the second stage, and the relation between P_0 and the field in the bending magnet (M2) were established by a form of floating-wire technique (13,14); those for the magnets in the first stage were determined empirically. M2 was shimmed to provide a constant field, and to compensate for path-length inequalities (3).

During the experiment, the currents in the magnets were stable to 0.1% (1a). The field in M2 was monitored by an N.M.R. arrangement, the frequency of which was reliable to 0.005% for each momentum setting. By repeating the floating-wire measurements at the completion of the experiment, it was estimated that the absolute momentum was known to 0.14% (14). This corresponds to uncertainties in the missing mass determination of 0.4 Mev/c^2 at the η threshold, and 0.7 Mev/c^2 at the threshold of the ω .

Since only pions were wanted in the incident beam, a long, gas-filled Cerenkov counter was included in the beam-line. It was used in veto to remove as much of the unwanted contamination in the beam as possible. After passing through the Cerenkov counter, the beam of pions was estimated to contain a 2 $\pm$ 2 % contamination of electrons and muons.

In the second stage, the momentum of each particle in the accepted band was determined. This was achieved by the installation of two sets of finger hodoscopes, the G and H counters, at the conjugate planes of unit magnification of the spectrometer. Each set consisted of thin scintillation counters mounted across the beam axis (Fig.2.3). The ratio of the widths of the G and H fingers was matched to the horizontal magnification of the spectrometer. Under these conditions, and with a uniform field in M2, a particle passing through the vertical plane at the G counters will horizontally intersect the vertical plane at the H counters at a point depending on its momentum. Thus, a knowledge of the horizontal displacements of the particle as measured by the counters H_i (i = 1,....,7) and G_j (j = 1,....,11) was sufficient to define the particular value of its momentum.

Although there were 11(7) fingers in the G(H) hodoscope, the outer pair of each set was not incorporated into the logic. Several possible combinations of H_iG_j defined the same momentum - namely those pairs for which i + j was the same integer. By electronically adding such combinations, the beam was analysed into five different momentum classes, or "channels", for each central setting P_o . As can be seen from Fig.2.3 , P_o corresponds to those combinations having

FIG. 2.2
BEAM LAY-OUT

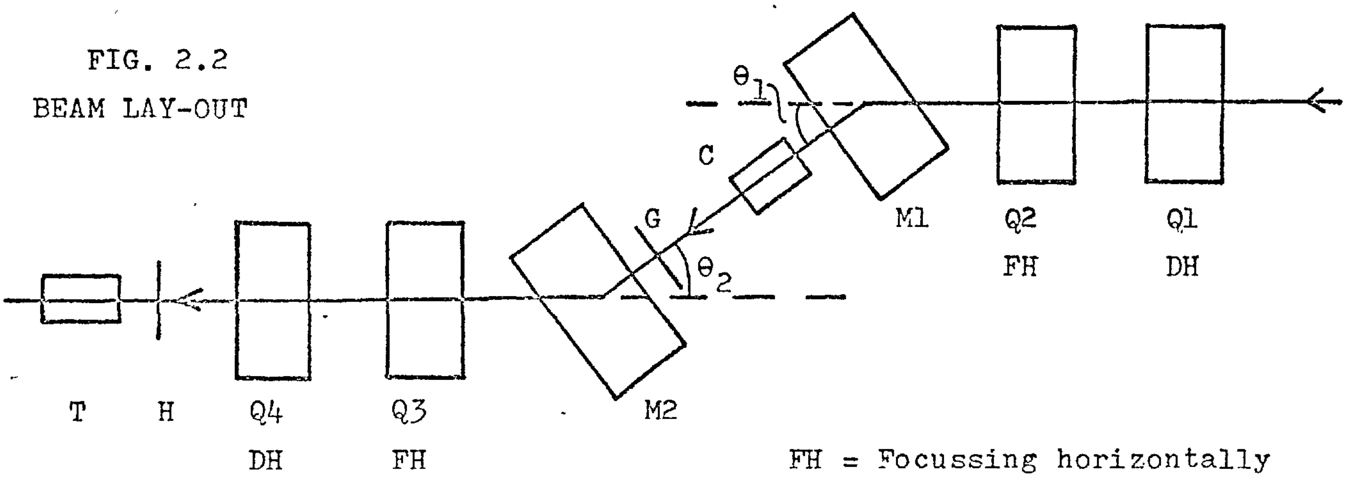

FH = Focussing horizontally
DH = Defocussing horizontally
C = Cerenkov Counter
G = G-Hodoscope
H = H-Hodoscope
T = Liquid Hydrogen Target
$\theta_1 = 7.25^\circ$
$\theta_2 = 9.75^\circ$

FIG. 2.3
THE HODOSCOPES

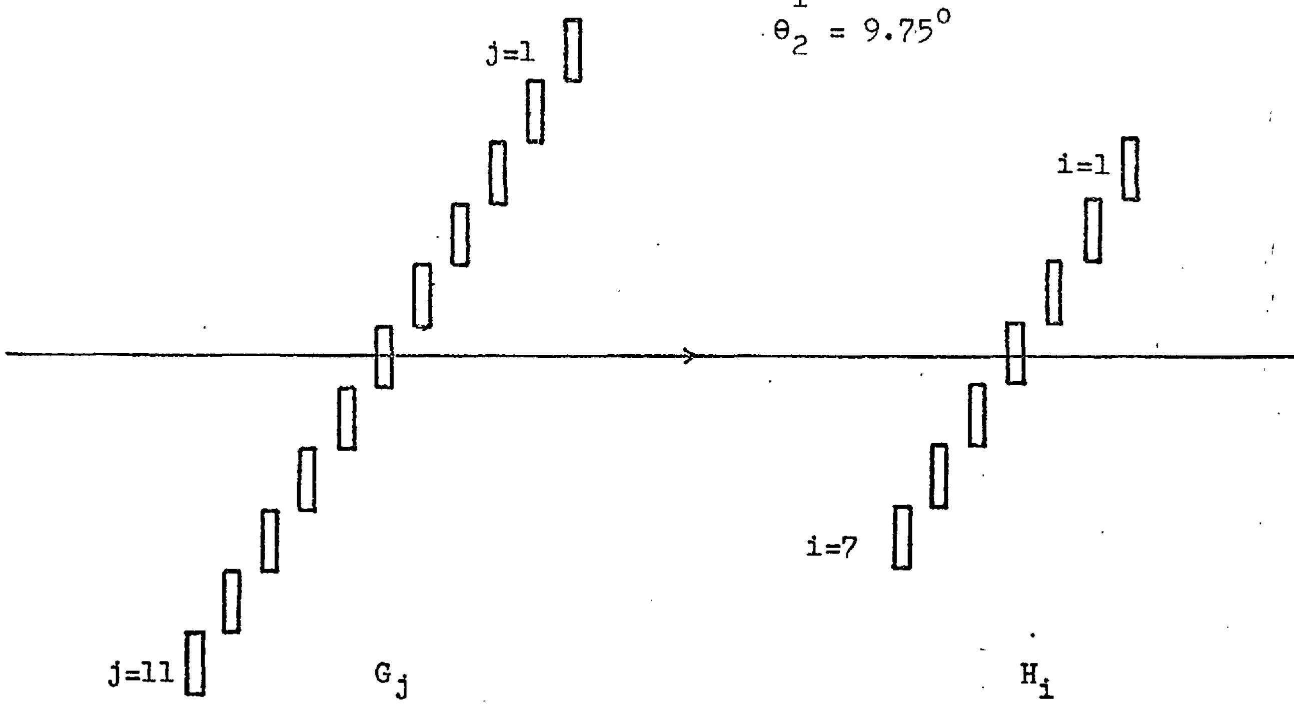

For each central momentum setting P_o, the hodoscopes define five separate momentum channels p_m:

$$p_m = P_o(1 + 0.005(m - 3)).$$

If $i + j = 8$, $m = 1$; if $i + j = 12$, $m = 5$. The central momentum $P_o = p_3$ occurs for combinations of H_iG_j for which

$$i + j = 10$$

$i + j = 10$.

Mainly due to the finite size of the hodoscope fingers, the momentum of each channel had a triangular profile, of full-width at half-height dp_i , such that the momentum bite dp_i/p_i was $\frac{1}{2}$ % (3). The momentum of each channel, p_i , was then given by the formula

$$p_i = P_o \left(1 + \frac{dp_i}{p_i}(i - 3)\right) \qquad i = 1,\ldots\ldots,5 .$$

where P_o is the momentum of the central channel.

Scalers monitored the number of pions in each of the channels, while a separate scaler independently recorded the total number in all five. This afforded a useful hardware check on the numbers used in the normalization of rates. The rate at which the incident pion beam was delivered to the target varied considerably throughout the full range of data. However, tests have confirmed that the yields for individual final states, and in particular for the single pion production channels, are independent of this effect (1f).

The beam-line transported the focussed beam of pions to the centre of the target, situated 45 cm. downstream of the H hodoscope. The target consisted of slowly-boiling liquid hydrogen; this ensured a constant density of protons available for strong interactions. A jacket, 29.4 cm. long by 6.5 cm. in diameter, made of 0.01" thick mylar contained the hydrogen. Encasing this jacket was an evacuated aluminium cylinder with transparent melinex end-windows. The hydrogen was supplied from a reservoir via a pipe connected to the aluminium casing.

Two problems arise with the use of such a target. Firstly, recoiling protons will lose some of their energy in ionising collisions in the hydrogen, before reaching the detection system. This important effect is discussed in section 4.5.2. Secondly, the other particles of the final state must first escape from the region of the target, in order to be detected. If charged, they will lose energy in the hydrogen, in the mylar, and in the aluminium; they must have sufficient remaining energy to trigger the decay array if they are to be detected. However, the energy required to trigger a counter in the decay array is some five times greater than the energy lost in escaping from the target area. In consequence, the energy required to trigger the array is is a much more critical factor than the actual energy lost in reaching the array: it is discussed in section 2.4.

2.3 The System for detecting the recoiling nucleons.

The experiment was to be sensitive to both proton and neutron final states. To this end, the system used to detect the recoiling nucleons comprised a set of six identical neutron counters, N_{1-6} , and a corresponding set of charged-particle detectors, the A counters, A_{1-6} . This system of counters was placed several metres downstream of the target.

The neutron counters were arranged symmetrically about the axis of the beam, forming a ring into which an identical counter could be fitted if desired. Each counter was made of cylindrical blocks of plastic scintillator, 30 cm. in diameter and 30 cm. in depth; each was optically interfaced by a conical perspex light-guide to a photomultiplier tube. Similar counters have a measured efficiency for neutron detection of approximately 25 % (15). For proton detection, their efficiency was assumed to be 100 % . As the counters were used as part of the system for timing the nucleons, they were temperature controlled for greater stability of operating performance.

A_{1-6} were six plastic scintillation counters, placed just upstream of the neutron counters, N_{1-6} . Hexagonal in shape, they completely covered the faces of their corresponding neutron counters. Their purpose was to help distinguish between neutron and proton triggers in a subsequent analysis of the data: a neutron would trigger only a neutron counter; a proton would trigger both an A counter and its corresponding neutron counter. To illustrate the general performance of this system, Fig.2.4 shows the yield curve of the sum of all the neutron final states; the curves are for the yields in the cms gate, for both the five and six metre data. The narrow η and ω mesons both show as strong enhancements on an otherwise slowly-varying background.

The temperature controlled box containing the neutron counters was mounted on a movable trolley, so that the position of the counters relative to the target could be

FIG. 2.4

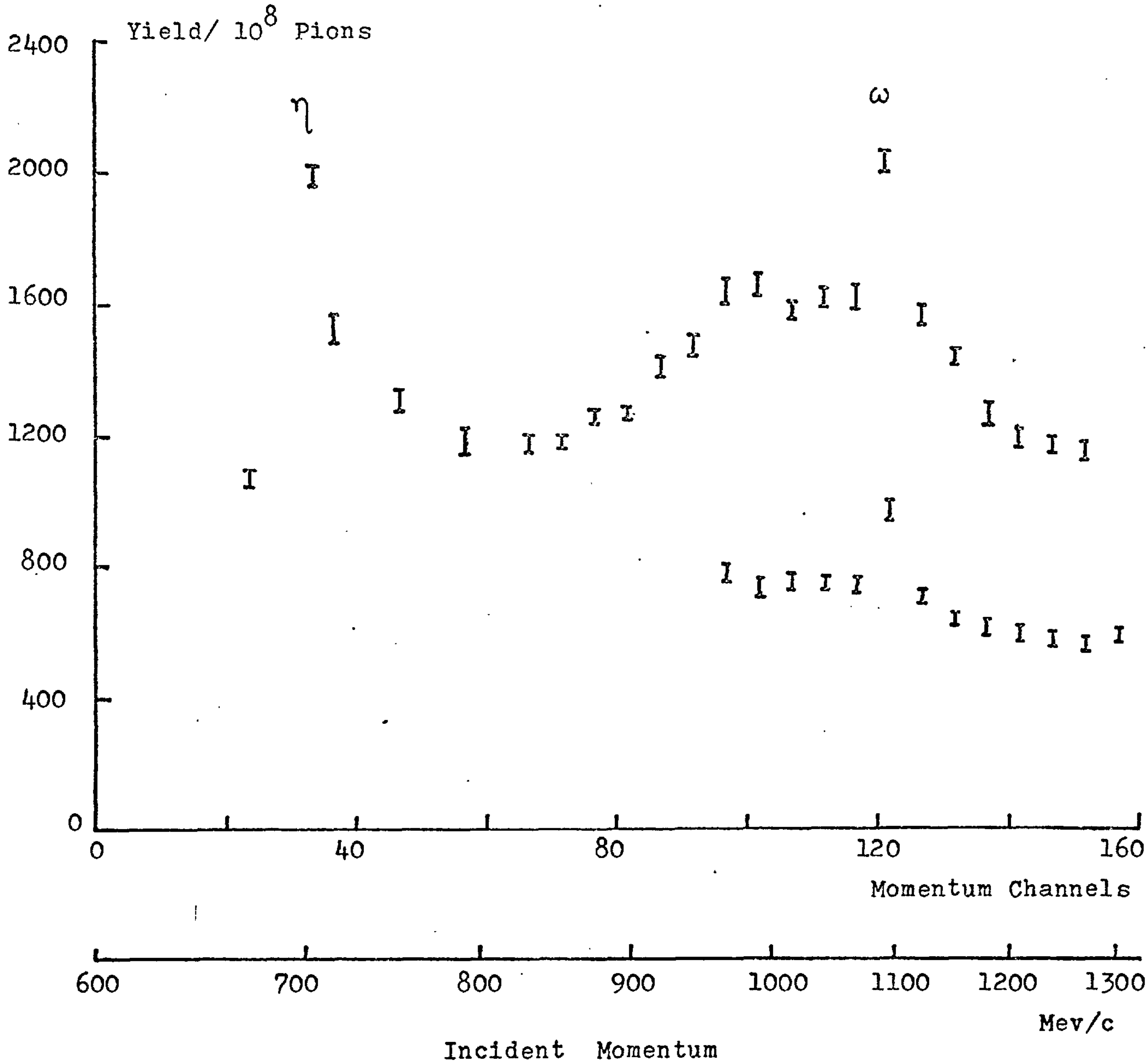

The yield curves generated from the cms gate for all final states having neutron triggers, for both the data at 5 mt. (upper) and 6 mt. (lower) .

adjusted. In the experiment two sets of data were taken, with the face of the neutron counter array at distances of 5.15 and 6.15 mt. from the centre of the target. The corresponding angles, θ , subtended by the counters at the centre of the target were $3.3 \pm 1.7^\circ$ and $2.8 \pm 1.4^\circ$ respectively.

2.4 The Decay Array.

The remaining products of the interaction were detected by a cylindrically symmetric array of counters enclosing the target (Fig.2.1). For the 6(5) mt. data, the array was composed of 40(40) counters sensitive to both charged particles and gamma-rays, while a further 26(23) detected charged particles only. The particles could be detected in any one of 20(20) different azimuthal regions in planes perpendicular to the beam axis, and in any one of 5(4) polar regions.

Nearest the target was an array of twenty plastic scintillation counters, known as the inner charged counters, which could detect charged particles only. The counters formed the segments of a cylinder parallel to the beam axis, bent and shaped at the downstream end to form vertical sectors of an annular lid (Fig.2.5). Each of the counters had its own air light-guide coupling it to a photomultiplier tube.

The hole left in the downstream lid, while allowing beam pions to pass out of the apparatus, was essentially designed so that recoiling nucleons could be detected without their interacting with the decay array. Its 20 cm. diameter

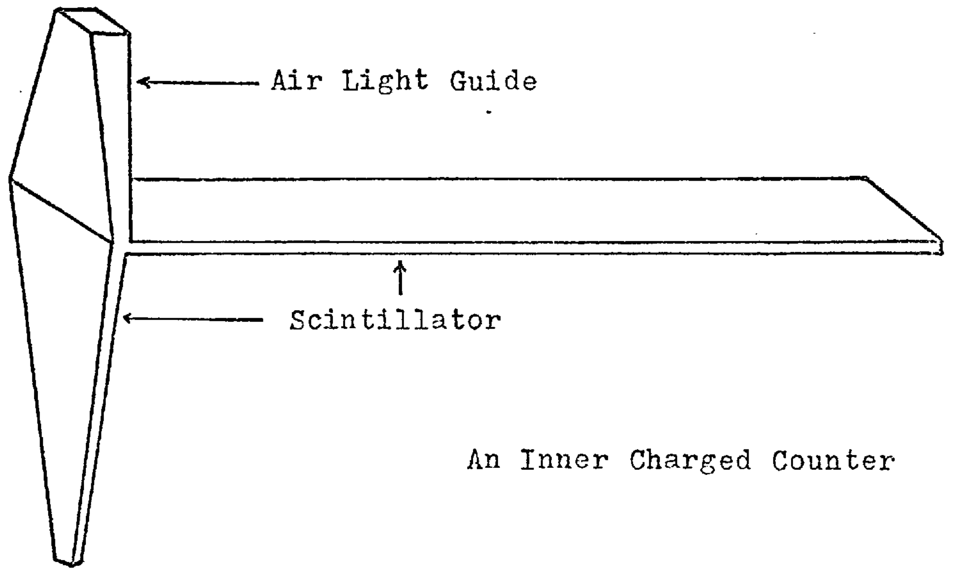

An Inner Charged Counter

The inner charged counters form paraxial segments of a cylinder, symmetrically surrounding the target; the counters are themselves surrounded by the Cylinder Gamma Counters. The inner charged are bent and shaped at the downstream end of the target to form sectors of an annulus, and are partly covered by the Lid Gamma Counters (see section 2.4)

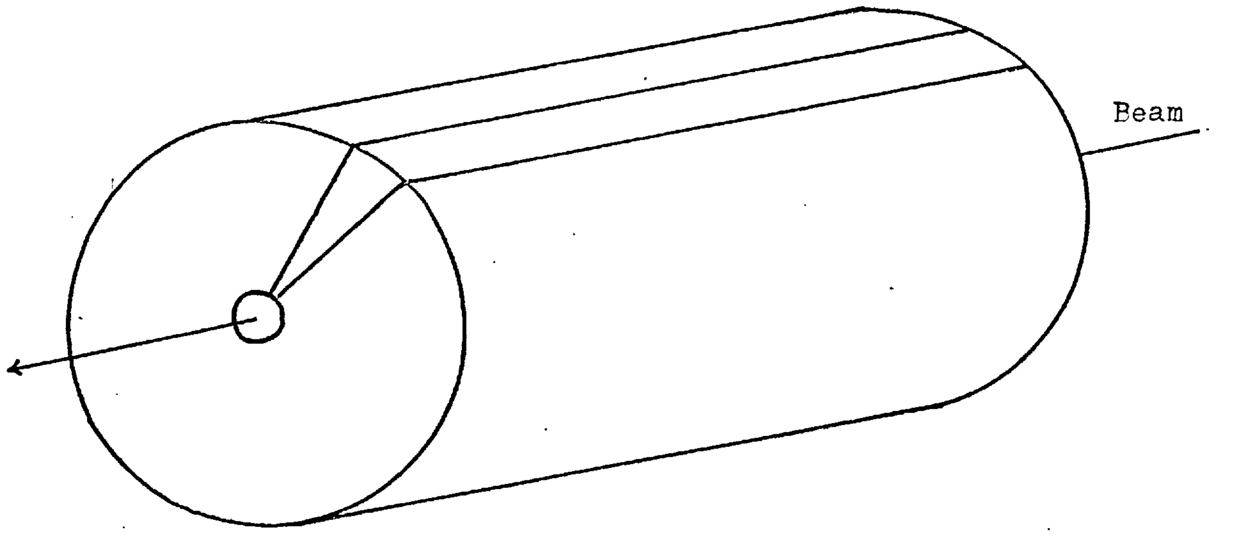

FIG. 2.5

was therefore chosen so that a nucleon produced at any point in the target could reach the extremities of the neutron counter ring without triggering an inner charged counter.

The array was made sensitive to uncharged particles by encasing the inner charged counters with two sets of gamma-ray detectors (Fig.2.1). The first set, the cylindrical gamma counters, comprised twenty counters forming the segments of a cylinder, each parallel to, and opposite, its corresponding inner charged member. The second set, the lid gamma counters, was composed of twenty detectors forming the sectors of an annulus; each covered almost all of that part of the corresponding inner charged counter forming the downstream lid. The region where overlapping was incomplete was filled by a small annular plastic scintillation counter, the "ring" (Fig.2.1).

All the gamma-ray detectors were constructed of six layers of 5 mm. thick plastic scintillator, interleaved with six of 4 mm. thick (equivalent to 0.7 radiation lengths) lead-plating, with a layer of lead innermost. For each counter, the layers of scintillator were connected via their own perspex light-guides to a single perspex button, itself coupled to a photomultiplier tube.

Gamma-rays (from the decay of a neutral pion for example) would be converted into electron-positron pairs in the lead-plating, and these would in turn activate the scintillator. Moreover, products of the interaction that were charged would automatically activate the scintillator in the usual way; so that this type of detector was triggered by both gamma-rays and charged particles.

In the lid at the downstream end of the array, where the gamma-ray detectors did not completely overlap with the inner charged counters, the ring counter provided for the detection of charged particles only.

To complete a coverage of almost 4π solid angle for the detection of charged particles, a lid at the upstream end of the cylinder was used. This was not so sophisticated as that at the downstream end, comprising two semiannular counters called the "droops", meeting in a vertical plane containing the beam axis. The droops were simple scintillation counters so that only charged particles could be detected in this polar region. No coverage of this region with gamma-ray detectors was made because the technical problems were many.

In principle, therefore, it was possible, over a large solid angle in those regions where the inner charged and gamma counters overlapped, to identify final states consisting of both charged and neutral pions. Thus a charged pion would require pulses in both an inner charged counter and the corresponding gamma-ray detector; on the other hand, a neutral pion would require pulses in two gamma-ray detectors only. To detect charged pions in that area of the downstream lid where there were no gamma-ray detectors, a spare inner charged counter and the ring counter had to be triggered together. Obviously, in the regions of the ring and droop counters it was only possible to detect charged pions.

Prior to the experiment, exhaustive studies of the detection efficiency of the decay array were undertaken, and each counter was tested individually. In particular, it was found that a pion required a minimum momentum of 70 Mev/c to trigger an inner charged counter: to trigger both an inner charged and a gamma counter, a pion must have a momentum of at least 135 Mev/c (13). From phase space calculations, however, only $\simeq$ 7 % of the charged pions produced in the $\pi^+\pi^-n$ channel at an incident momentum of 1070 Mev/c (the threshold momentum for ρ production) are expected to fail to trigger both counters.

Extensive tests on the performance of the gamma counters were also made (16). It was established that a gamma-ray required an energy of only 20 Mev. to be detected by the array: at the ρ threshold $<$ 1 % of the gamma-rays from the neutral pions in the $\pi^-\pi^0p$ channel would be expected to fail to trigger the gamma counters. The general performance of the counters, and the probability of producing "double gammas" - adjacent counters in the same polar region triggered together - were established as functions of gamma-ray energy.

All these results were then used in a Monte-Carlo simulation program (descibed in section 3.3), and checked under experimental "running" conditions by studying the $\eta \rightarrow \gamma\gamma$ decay. The branching ratio obtained for this decay mode was consistent with the listed value of 38 $\pm$ 2 % (5).

The response of the decay array to charged and neutral pions in the single pion production channels is discussed at length in chapter three.

2.4.1 The modifications made to the apparatus for the 6 mt. data.

The most important modification to the decay array was the addition of the six circular, plastic scintillation counters, the target counters (Fig.2.1). These were wrapped side by side around the length of the target. Their main purpose was to provide a more accurate estimate of the interaction vertex - important in the case of slow recoiling protons as already mentioned. Additionally, the target counters could be used in the selection criteria of certain final states. For example, in the $\pi^-\pi^0 p$ channel, if the charged pion was detected in the cylinder, at least one target counter must have been triggered; otherwise, the event was rejected from the $\pi^-\pi^0 p$ class.

The L-counters, two charged particle detectors semiannular in shape, were mounted vertically between the ring and lid gamma counters. They could provide additional information by defining an extra polar region, but in fact were not used in this analysis.

The ring counter was divided into two semiannular halves, to furnish a crude correlation between the ring and the spare inner charged counters used in the definition of a charged pion. Thus it was now demanded that for a charged pion the half of the ring and the spare inner charged counter that were triggered together must belong to the same azimuthal half of the decay array.

Because of the increased rate of incident pions available for the 6 mt. data, it was necessary to remove the unfocussed "halo" of particles surrounding the pion beam. This was done by introducing a square counter, the A_{13} , adjacent to, and slightly overlapping with, the droop counters (Fig.2.1). Events in which the A_{13} counter was triggered were vetoed by the hardware.

To summarize: the decay array provided an overall solid angle coverage of 3.95π for charged particle detection, and 3.25π for neutrals. Many different final states could be studied simultaneously, and independently of the event (neutron or proton) trigger.

2.5 The Event Trigger Logic.

Detailed descriptions of the electronic logic used in the experiment can be found in references 1d and 13: the important features are outlined here. All the electronic circuits used were temperature controlled for stability.

A circuit was used to define those pions in the incident beam which were involved in strong interactions in the hydrogen. Beam pions entered the target area via the G and H hodoscopes (section 2.2) and the beam counter S . Those having no strong interaction would, in general, leave the apparatus via the two beam veto counters, A_0 and A_{01} . Conversely, strongly interacting pions would not exit in this way: for this type of event, an interaction signal ST3 would be formed, where,

$$ST3 = G_i . H_j . S . \bar{C} . \bar{A}_0 . \bar{A}_{01} \qquad (i = 2,10;\ j = 2,6)$$

with the Cerenkov veto included to ensure as near as possible that the interacting particles were in fact pions. Fig.2.6 shows a simplified diagram of the relevant circuit. Events were rejected if two or more pulses were received from S within 30 ns. of each other (1d).

The A_0 , A_{01} and S counters were all charged particle detectors made of plastic scintillator, and S , as part of the time-of-flight measuring system, was temperature controlled for greater stability of performance.

As a check on the overall operation of the counters involved in the definition of ST3 , Fig.2.7 shows the ST3 rate plotted as a function of incident momentum over the range discussed here. The general smoothness of the curves for both the 5 and 6 mt. data, and their similarity in behaviour in the overlapping momentum region, is evidence for the satisfactory performance of this system of counters.

Generally speaking - the exceptional cases are discussed below - when ST3 signals were formed, recoiling nucleons were produced. The system for detecting nucleons emitted at angles to the incident beam in the range $\theta \pm d\theta$ has been described in section 2.3 . If, within a predetermined interval, defined by the hardware, of receiving an ST3 signal, a pulse was also received from one of the neutron counters, N_i , an event or master trigger was formed. The suitably digitised

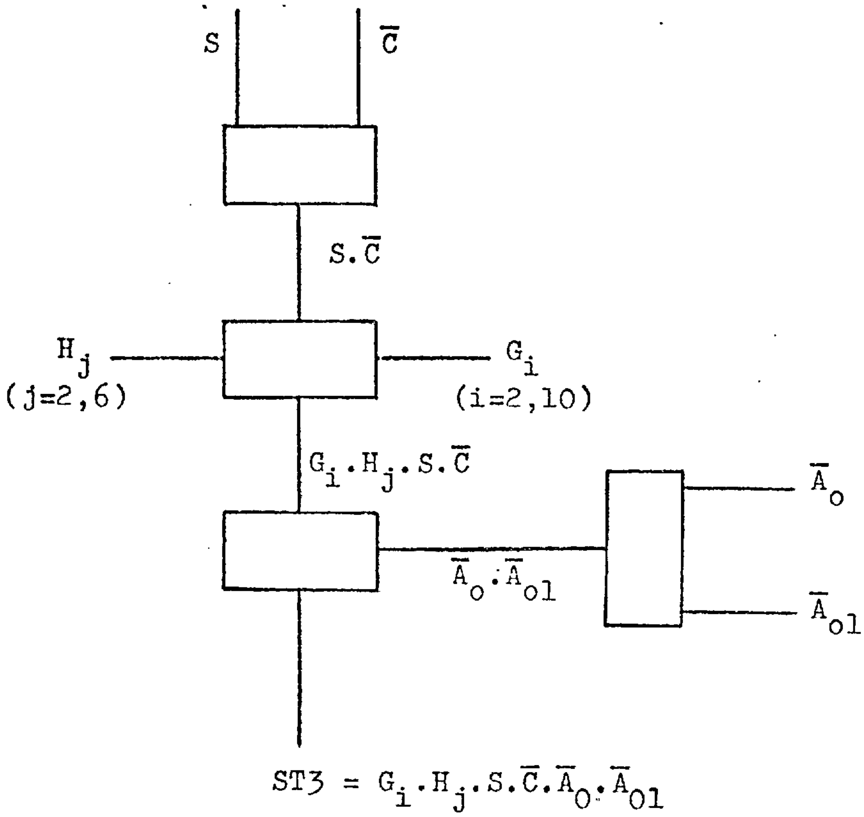
S
C̄
S.C̄
H_j
(j=2,6)
G_i
(i=2,10)
G_i.H_j.S.C̄
Ā_o
Ā_o.Ā_o1
Ā_o1
ST3 = G_i.H_j.S.C̄.Ā_O.Ā_O1

FIG. 2.6

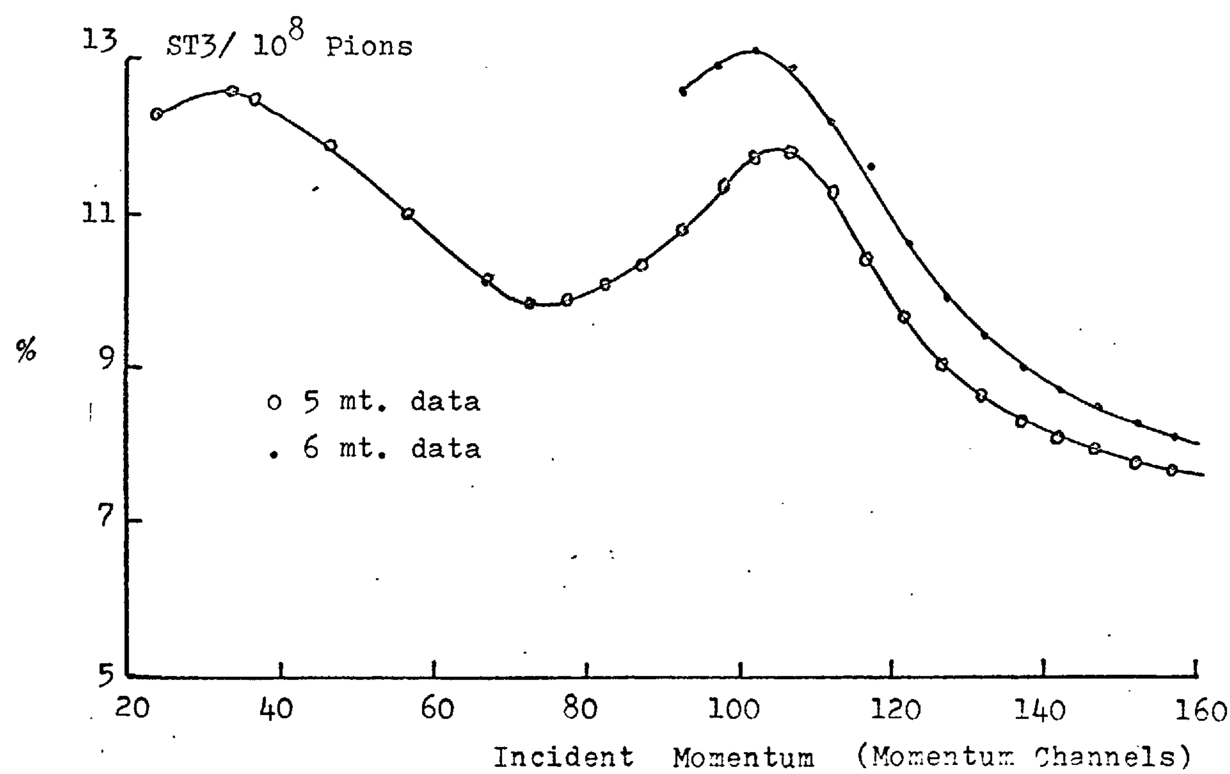
ST3/ 10^8 Pions
%
13
11
9
7
5
o 5 mt. data
. 6 mt. data
20
40
60
80
100
120
140
160
Incident Momentum (Momentum Channels)

FIG. 2.7

difference in time between the pulses in S and N_i was taken as the raw time-of-flight of the recoiling nucleon.

The hardware gate was opened some 10 ns. before particles with velocities $\beta \simeq 1$ could reach the neutron counter array from S . As a result, the experiment was in danger of being swamped by beam pions scattering through small angles in Coulomb interactions in the hydrogen into the neutron counters. Such pions would reach the array, with velocities $\beta \simeq 1$, to form the "fast-peak". Similarly, gamma-rays detected in the array would form a peak in the time-of-flight spectrum of the neutron channels. To avoid this, a "prompt-veto" was employed: this removed events with times-of-flight distributed a few nano-seconds either side of the "fast-peak". However, the veto was removed every so often, so that the peak could be randomly sampled, thus furnishing a reference for the time-of-flight spectrum. The position of the peak was determined to within a $\pm$ 20 psecs. uncertainty (1a,1b).

Obviously any event triggers occurring before the "fast-peak" could not be attributed to physical processes of interest. They were thought to be random or "casual" coincidences between ST3 signals and stray pulses in the nucleon detectors. Thus for an interacting beam pion producing a nucleon scattered outside the angular range accepted by the neutron counters, a master trigger could result from an accidental coincidence in the nucleon detectors. Assuming this were the sole cause of such master triggers, the random nature of the process would guarantee the formation of a structureless distribution of events at all times-of-flight. As such, the rate measured in the region before the fast-peak could be extrapolated to that part of the spectrum corresponding to genuine strong interactions. Thus by subtracting the suitably normalized (for gate width) rate of these casual events from the total rate, the yield of genuine events in any gate was obtained. This process would be invalidated if any part of the time-of-flight spectrum of casual events contained structure. Possible sources of structure might include: (i) some form of scattering off the surroundings of the apparatus into the nucleon detectors; or (ii) some form of time-dependent effect produced by the various veto and coincidence requirements demanded in the electronic logic circuitry. As these effects cannot be monitored, it would be impossible to correct the data of each run accordingly. But to reduce the level of casual events and minimize the chance of such possible effects, various precautions were made: thus, requirements were made on the selection of 'good' proton or neutron triggers (see section 3.2.1); events with two pulses in either set of hodoscope counters were vetoed; and events were rejected if two or more pulses were received from the S counter within 30 ns. of each other.

The regions of the visible casual events, of the fast-peak, and of events from genuine strong interactions are illustrated in Fig. 2.8.

As the incident momentum is increased, more phase space becomes available to the final states; in consequence, the nucleons have probabilities of increased momenta - or shorter times-of-flight. So as the momentum is increased, more and more events from strong interactions can merge into the

FIG. 2.8

The time-of-flight spectrum of all events having 'good proton' triggers (see section 3.2.1).

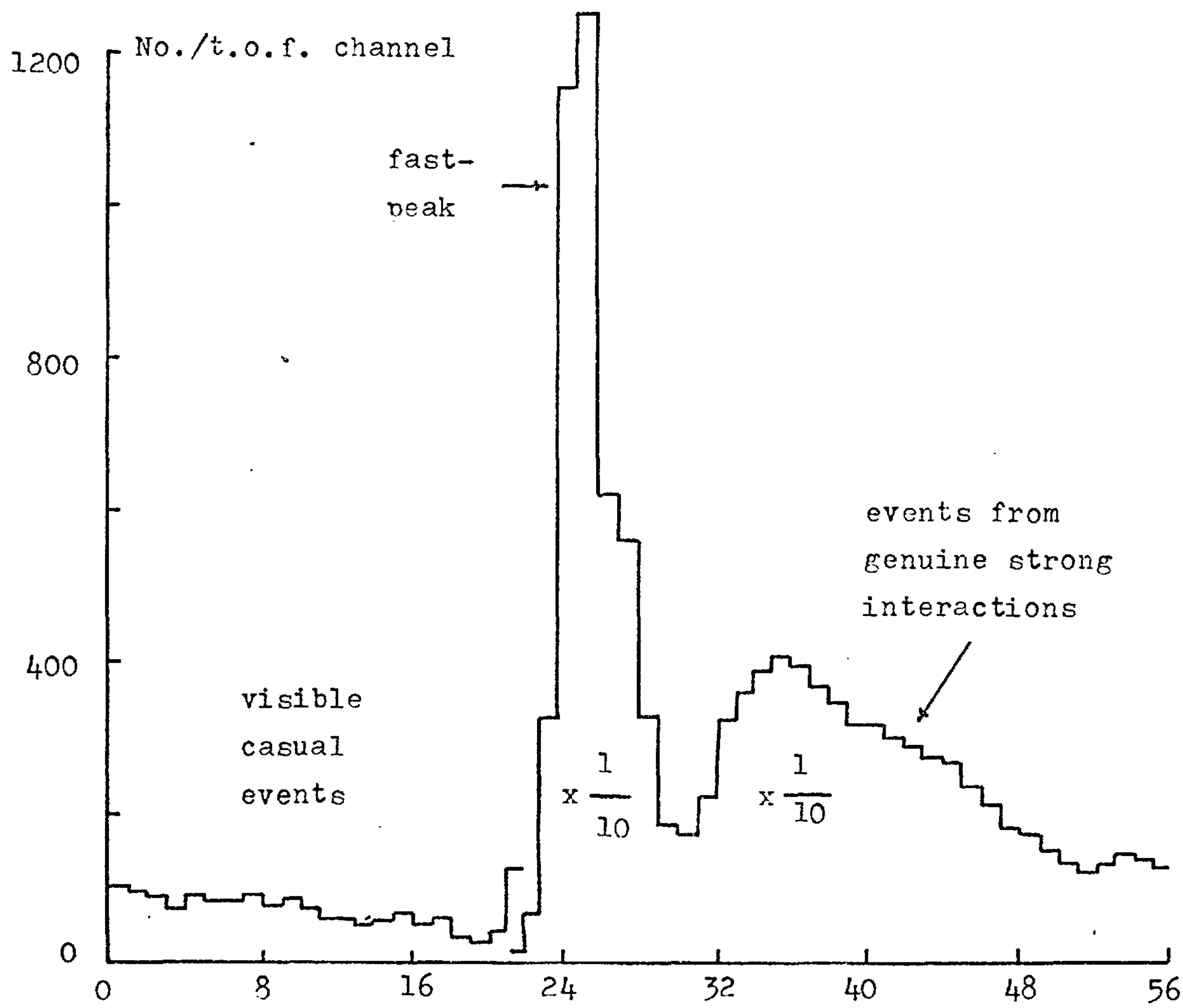

For these proton triggers, the time-of-flight spectrum shows (from left to right): the region before the fast-peak where the casual events can be seen; the region where the prompt-veto was used, and the fast-peak formed; and finally, the region of events from genuine strong interactions. Each time-of-flight channel is approximately 0.52 ns. wide. The spectrum is taken from the 6 mt. data, at 1097 Mev/c. There would be a similar spectrum for all events having 'neutron' triggers (section 3.2.1), except that a very much smaller structure formed by spurious gamma-rays (the gamma-peak) would replace the fast-peak in the region where the prompt-veto was applied.

fast or gamma-peaks.

In both the 5 and 6 mt. data, the casual events in the neutron time-of-flight spectra have structureless, flat distributions; for the $\pi^+\pi^-n$ channel, the yield curve, obtained from the casual events in a gate before the gamma-peak, is also structureless, and independent of incident momentum. The casual events in the proton time-of-flight spectra show signs of spurious structure - especially in the 5 mt. data. However, the yield curve of these events for the $\pi^-\pi^0p$ channel is smooth, and negligible compared to the strengths of the enhancements observed in the yield curve of genuine events. Below 1 Gev/c, the casual to genuine events ratio is estimated to be less than 3 % . This is to be compared with the strength of the enhancement at 755 Mev/c (Fig.4.1), which has an estimated signal to background ratio of approximately 3:1 . Above 1 Gev/c, the 6 mt. data is preferred for a detailed analysis (because it has better statistics, and fewer casual events - the latter due to the introduction of the A_{13} counter). Here the ratio of casual to genuine events is < 2 % - to be compared with an enhancement at 1070 Mev/c having a signal to background of about 3:5 (Fig.4.2).

One additional counter, the P counter, was also mounted in the beam, downstream of the target (Fig.2.1). Although this small, plastic scintillation counter played no part in the logic of event selection, it was important at the subsequent software analysis stage. Nucleons detected by the apparatus must leave the target and pass through P on their way to the nucleon detectors. A pulse in P would imply a proton rather than a neutron event. As a further test, the pulse-height in P (proportional to dE/dx) was monitored, so that protons could be distinguished from other charged particles; because of the many other criteria used to identify the $\pi^-\pi^0 p$ final state, (described in chapter three), the pulse-height test was not needed in this analysis. A pulse in P was demanded, however, for a proton event, while P must not be triggered for neutron events.

2.6 Data Collection.

An "on-line" PDP-8 computer controlled the progress of the experiment during "running" time.

Before starting a run at a given momentum, the magnet currents and the NMR frequency were adjusted to their appropriate values. Sample data was recorded by the computer and analysed to provide the distributions of events in the counter arrays, the hodoscopes, and in the nucleon time-of-flight spectra. In this way it was possible to ensure that the system was correctly set-up and operating normally. At this stage the run details were stored on magnetic tape, and the computer restarted to take and store data.

When a master trigger was received from the logic, the state of all the counters, the digitised pulse-heights in the N and P counters, and the digitised time-of-flight were all transferred via the electronic interface to the computer. Each counter was assigned a particular "bit" in the computer store.

A "1" state meant that the corresponding counter had been triggered in the event; a "0" state meant that it had not.

Such information was continually transferred via a temporary disc store to the magnetic tape for permanent storage. As much "on-line" computation as the core-size of the PDP-8 allowed was performed in concert with the data collection. Thus at the end of each run, a summary of the data was available. This ensured that nothing that might go seriously wrong with the system would go unnoticed, by allowing run-by-run checks on the performance of the system to be made. Similarly, at any time during a run, the experiment could be halted and the various distributions of events examined on a CRT screen, to check the continuing efficient operation of the system.

At intervals during data collection, the time-of-flight scale was calibrated: throughout the experiment it was found to be stable to better than 0.15 % .

As already mentioned, two sets of data were taken, embracing the incident momentum region from 670 to 4000 Mev/c. In the range discussed here, the 5 mt. data consists of two overlapping series of runs (taken at two different times), in the ranges 673 to 993 Mev/c and 968 to 1306 Mev/c: the 6 mt. data is composed of a single series in the range 945 to 1306 Mev/c. The two lowest limits, 673 and 945 Mev/c for the 5 and 6 mt. data respectively, represent the extremities of the recorded data: 673 Mev/c was chosen as just below the η threshold; runs below 945 Mev/c in the 6 mt. data were not possible because of a Nimrod failure. The upper limits used in this analysis have been somewhat arbitrarily chosen - as the sort of area beyond which the total cross-sections for the single pion production channels show less signs of structure.

In the two sets, the data was mainly taken in a "one-in-five" scan - that is the central momentum for each run was chosen so that it was separated from the previous one by five momentum channels (as defined in section 2.2). Typically there were some 50 million pions per channel in the 5 mt. data, and some 100 million per channel in the 6 mt. data.

Chapter Three
The Analysis of the Single Pion Production Channels.

3.1 Introduction.

This chapter is devoted to a general description of the techniques used in analysing the data, and specifically to the identification and treatment of the single pion production channels $\pi^-\pi^0p$ and $\pi^+\pi^-n$.

At the completion of the experiment, the raw data tapes were decoded and analysed by "off-line" programs on the Rutherford Laboratory's IBM-360 computer.

To ensure as much uniformity of treatment as possible, one program - called KRUNCH - was used to analyse all the tapes. Basically, KRUNCH read and decoded the information; then histogrammed and stored accepted events in the form of time-of-flight spectra, categorized according to the nucleon type and the classification of the state of the decay array. There were ninety permitted classifications, each representing a summary of the decay array information. So the reduction to summarized form of raw data representing a variety of final states was able to proceed simultaneously. This uniformity in the treatment of the data provided an important element in checking against possible spurious structure. Thus, if any structure was observed in the yield curve of a particular final state, yield curves of different final states could also be examined - on an equal basis - to try to discover whether it was due to instrumental effects, or was a genuine enhancement.

As KRUNCH was restricted to ninety classifications, each final state of particles was allowed only a certain number of these. The decision as to which classifications were to be interpreted as the particular final states of interest, and the choice of which of these should be included in KRUNCH, was made in a preliminary analysis. This involved the use of a similar program - called SIP - which, however, could examine the data in more depth. The criteria used to determine which classes were used in KRUNCH for the single pion production channels is discussed in sections 3.4 and 3.5.

Having chosen appropriate classifications with SIP, all the data tapes were then analysed by KRUNCH. A series of time-of-flight spectra, one for each of the ninety classes, was produced. When all the data of a run was analysed, these were transferred by KRUNCH to a data summary tape (a DST), the whole process being repeated for each run in the series.

In the second stage of the analysis, different physicists studied the groups of classifications corresponding to different final states, over momentum ranges of interest. Programs were used to read and analyse the DST, furnishing output of the appropriate time-of-flight spectra, yield curves, and mass-plots. As additional input, various timing limits could be used, so that the behaviour of the yield curves and mass-plots could be studied as functions of timing gate.

3.2 The Analysis Program.

The main functions of KRUNCH, the analysis program, are outlined in this section.

3.2.1 The initial selection of events.

In the first part of the program, the state of the counters involved in the selection of master triggers was checked, the type of nucleon in the final state established, and a preliminary selection of the data made.

After reading and decoding an event, the master trigger was tested. All events had either "good" proton or neutron triggers, or were rejected from further analysis. A "good" proton trigger was one for which there were two pulses in the corresponding A and N counters (A_iN_i , $i = 1,....,6$), together with a pulse in the P counter. A "good" neutron trigger demanded a single pulse in one of the N counters ($\bar{A}_iN_i$) , and no pulse in P. All other sorts of trigger were "error conditions" and were vetoed. At the same time, the hardware used in the selection of suitable beam pions was checked: only events with single pulses in each of the G and H hodoscopes, with another corresponding pulse in the appropriate momentum channel monitor, were allowed. Furthermore, events with pulses in any of the A_0 , A_{01} or Cerenkov counters which had survived the hardware selection were also rejected at this stage.

It was decided that events in which either of the droop counters had been triggered should also be vetoed. This ensured that there was no significant asymmetry between the collection efficiencies for charged and neutral pions. For example in the $\pi^-\pi^0p$ channel, the gamma-rays from a neutral pion travelling backwards in the laboratory would not be detected in the region of the droop counters. By vetoing events with charged pions in this polar region, the bias was removed.

Every event surviving these preliminary acceptance tests had its raw time-of-flight adjusted for pulse-height variations in the neutron counters (the N counters). (From studies of π^-p elastic scattering, from the charge exchange reaction $\pi^-p \rightarrow \pi^0n$, and from $\pi^-p \rightarrow n\eta$, it was found that the error in a single measurement of time-of-flight was $\pm$ 0.6 ns. (standard deviation).)

3.2.2 The Interpretation of the Decay Array Information.

An event with an accepted master trigger surviving the initial selection criteria, was next allocated a six-digit number which summarized the state of the decay array for that event. Each digit represented one of six possible particle classes, and its value was the number of times that class had occurred. The possible classes and the corresponding configurations of the decay array were as follows:

first digit:	a simple pion - the corresponding inner charged and gamma counters had been triggered together;
second digit:	a π-gamma - the same as a simple pion

	but with an additional pulse in an adjacent gamma counter;
third digit:	a π-delta - the same as a simple pion but with an additional pulse in an adjacent inner charged counter;
fourth digit:	a delta - a spare inner charged counter had been triggered (without an accompanying pulse in the ring counter);
fifth digit:	a gamma - a single gamma counter had been triggered;
sixth digit:	a double-gamma - two adjacent gamma counters in the same polar region had been triggered together.

Thus by interrogating in turn each counter and its two neighbours, a description of the state of the decay array in terms of the six-digit classification was achieved for each event. Each counter which had been triggered in an event could only contribute to one of the above six categories.

As an example, the classification 100020 represented the detection of one simple pion (interpreted as a charged pion) and two gamma-rays (which could be interpreted as implying the decay of a neutral pion - see below). An example of the state of the decay array for a typical event , and its interpretation, is given in Fig.3.1.

FIG. 3.1

Classifying the state of the decay array.

array type	counter number and state																			
	1	2	3	4	5	6	7	8	9	10	11	12	13	14	15	16	17	18	19	20
inner charged	0	0	0	0	1	0	0	0	0	0	0	0	0	0	0	0	0	0	0	0
lid gamma	0	0	0	0	0	0	0	0	0	0	0	0	0	0	1	0	0	0	0	0
cylinder gamma	0	0	0	0	1	0	0	0	0	0	1	1	0	0	0	0	0	0	0	0
					simple pion						double gamma				gamma					

The classification of the state of the decay array for this event would be 100011 : if the event had a proton trigger, it would be interpreted as a $\pi^- \pi^0 p$ final state.

On the other hand, if the state of the array was as follows:

1	2	3	4	5	6	7	8	9	10	11	12	13	14	15	16	17	18	19	20
o	0	0	0	1	0	0	0	0	0	0	0	0	0	1	0	0	0	0	0
0	0	0	0	1	0	0	0	0	0	0	0	0	0	0	0	0	0	0	0
0	0	0	0	0	0	0	0	0	0	0	0	0	1	1	0	0	0	0	0
				simple pion										π - gamma					

the classification would be 110000 : if the event had a neutron trigger, it would be interpreted as a $\pi^+ \pi^- n$ final state.

3.2.3 Further selections.

The classification of the state of the decay array together with the type of master trigger (neutron or proton) usually provided sufficient information for the identification of the event as a particular final state. So, for example, a classification 200020 with a neutron trigger would imply the detection of the $\pi^+\pi^-\pi^0 n$ final state. In a similar spirit, 100020 with a proton trigger, and 200000 with a neutron trigger, could represent $\pi^-\pi^0 p$ and $\pi^+\pi^- n$ respectively.

However, since the decay array could distinguish twenty different azimuthal regions (each of 18^o pitch), it was possible to impose certain geometric cuts on the particle separations in the final states of the single pion production channels (see sections 3.4 and 3.5). To this end, a further selection process in the analysis program entailed checking the azimuthal separations of the particles against predetermined expectations obtained from a Monte Carlo simulation. Failure to meet the demands of such predictions meant that events would not be identified as these particular final states.

At the same time it was possible to help distinguish between certain types of interaction which would naturally have the same signature in the decay array. Thus the interactions $\pi^- + p \rightarrow \pi^- + \eta + p$, $\eta \rightarrow \gamma\gamma$, and $\pi^- + p \rightarrow \pi^- + \pi^0 + p$, $\pi^0 \rightarrow \gamma\gamma$ (both having the same 100020 classification, and a proton trigger) could be partly distinguished by suitable cuts on the separation of the gamma-rays, deduced from the Monte Carlo.

For the single pion production channels, no cuts were made on the polar distributions of the particles, with the exception that events with charged particles in the droop counters were vetoed, as already mentioned. For the runs comprising the 6 mt. data, the information from the target counters was also used in the analysis to help with the classification of events (see section 2.4.1).

At this stage, when the classification of the event was complete, the time-of-flight (corrected for the energy loss in the hydrogen in the case of proton events in the 6 mt. data) was histogrammed in spectra according to the event classification.

When all the events of a particular momentum run had been analysed, the program transferred the ninety histograms to the summary tape (the DST).

3.3 The Monte-Carlo Simulation of the Detection Efficiency of the Decay Array.

For those events detected in single pion production, the pions are constrained in the laboratory to have almost equal and opposite momenta in a plane perpendicular to the beam axis ($\theta = 0$). This can be understood by recalling that all the initial momentum is along $\theta = 0$, while detected nucleons must also travel at small angles θ to this axis. As a result, the recoiling nucleon can have only a small momentum component in such a plane, implying that the dipion system must have a similarly small net component. This property is very useful, since it infers that the two pions will appear in decay counters which are separated by an azimuthal angle of 180° - separated, that is, by ten decay counters. The single pion production channels are therefore relatively easy to identify (although $\pi^{0}\pi^{0}n$ is more complicated than either $\pi^{+}\pi^{-}n$ or $\pi^{-}\pi^{0}p$ because of the four gamma-rays in this final state). As a result, the two with the clearest signatures were studied to gain an understanding of the response of the array to pions. It was found that the array did not always respond in an entirely simple fashion. For example, a charged pion might trigger two adjacent inner charged counters; or two adjacent gamma counters; there was a chance that the pion would not reach the gamma counter array, and so on. Such possibilities were dependent on the energy available to the pions. By studying these effects, or "aberrations" as they were called, over a wide range of incident momentum, the probabilities of the various possibilities were established. With such information, together with that on the response of the array to gamma-rays (section 2.4), it was possible to produce a program to simulate the detection efficiency of the array.

At a given incident momentum, the program assumed an event trigger - that is a recoiling nucleon directed towards the neutron counters - and a known time-of-flight. The 4-momentum of the nucleon was therefore completely specified, and that remaining from the conservation of the 4-momentum of the initial state (essentially defined by the incident pion momentum) was shared between the two pions according to an isotropic, 2-body phase space distribution in the centre-of-mass of the dipion system. The fate of each pion in the laboratory was then determined, according to its charge, using the known probabilities of detecting aberrations in the decay array, and the specification of the geometry of the detection system. So a simulated event might have a charged pion appearing as a π-delta in the lid, or as a π-gamma in the cylinder; or a gamma-ray from the decay of a neutral pion might appear as a double-gamma; and so on.

The output formats of this and the analysis program, SIP, were made almost the same, enabling a study of the data in direct comparison with the simulated predictions to be made. The outputs included the rates of chosen classifications in preselected timing gates, together with the relevant polar and azimuthal distributions of the particles in the final state.

When a successful comparison had been achieved, the simulation program was extended to the case where there were three pions in the final state. Here no geometric constraints were relevant, and the signature in the decay array was not so clear: so it was important to have predictions of in which classifications such final states would appear, and of how efficiently they could be detected.

In the following sections a similar comparative study is made of the single pion production channels $\pi^+\pi^-n$ and $\pi^-\pi^0p$; the study serves the following purposes:

(1) to investigate the effects of the geometric cuts made on the data as a means of reducing background contamination from the

selection of events for these final states;

(2) to justify the final selection of classifications used in the analysis program KRUNCH;

(3) to check the consistency of the data over the momentum range considered here.

3.4 The $\pi^-\pi^0p$ Channel.

Among the many possibilities, assuming proton triggers, the "pure" classification 100020 is the most obvious candidate to comprise events from this channel. Recalling the definitions of section 3.2.2 , 100020 corresponds to detecting a simple (or charged) pion and two gamma-rays in the array. As well as this, four aberrant classifications were used as including events from the $\pi^-\pi^0p$ final state:

100010 : a simple pion and a single gamma-ray;

100001 : a simple pion and adjacent gamma-rays in the same polar region (a double-gamma);

100011 : a simple pion, a gamma-ray and a double-gamma;

and 120 : a delta and two gamma-rays.

Following the discussion of the previous section, three tests were made on the data. Two of the tests involved studying data of three typical runs, those at 755, 1070 and 1306 Mev/c in the 5 mt. set. This sample data was analysed into classifications representing most of the possible forms the $\pi^-\pi^0p$ final state would assume in the decay array. In particular, the program SIP was used to examine both the rates and angular distributions of events in these classifications, comparing them with the predictions obtained from the Monte-Carlo simulation program described in section 3.3. In the third test, outputs produced by the analysis program KRUNCH were used. The rates in the selected classifications were compared with that in the "pure" 100020 mode (as a function of incident momentum) to investigate the overall consistency of the data.

Each of these tests is now discussed.

3.4.1 The effects of cuts on the angular distributions of the final-state particles.

Essentially these cuts were made to remove as much unwanted contamination of non- $\pi^-\pi^0 p$ events from the selected signal as possible.

The Monte-Carlo simulation was used to predict the limited range of azimuthal separations between the two pions and - where relevant - the two gamma-rays expected for events in the $\pi^-\pi^0 p$ final state. In practice, these predictions varied slightly with incident momentum. To simplify the analysis, the program KRUNCH applied the same selection criteria to the complete set of data (that is for the runs from 670 to 4000 Mev/c). Accordingly, compromise criteria derived from the predictions of the Monte-Carlo were adopted. This implied that the background levels in the selected classifications would change slightly over the complete set of data.

In the case of the 100020 mode, both the above cuts were relevant.

The situation is illustrated by Fig.3.2; here the azimuthal separation between the two gamma-rays is called ϕ_1, and that between the two pions, ϕ_2. Two-dimensional plots (and their corresponding projections) of the numbers of events, $N(\phi_1)$ and $N(\phi_2)$, at separations ϕ_1 and ϕ_2 are plotted for both the predicted Monte-Carlo events and the observed data, at 1070 Mev/c. Each bin represents a separation of one decay counter (of 18° pitch); separations of zero to ten counters are possible. The numbers of events in the two-dimensional plots are unnormalized; for the projected histograms, the numbers predicted by the Monte-Carlo have been normalized, so that the predicted histograms contain the same number of events as those of the data.

Obviously, the $\pi^- \pi^0 p$ events are clustered at high pion-pion, and low gamma-gamma azimuthal separations; by using suitably chosen cuts on these separations, much of the non- $\pi^- \pi^0 p$ contamination can be eliminated, and the remaining signal will contain a high percentage of $\pi^- \pi^0 p$ events.

In the analysis, therefore, only those events having $0 \leqslant \phi_1 \leqslant 4$ counters were selected for inclusion in the 100020 class; at 1070 Mev/c this cut removed some 38 % of the total signal in this class.

In the analysis, the direction of the neutral pion was taken as the bisector of the two gamma-rays (as measured by the decay array). The degree of colinearity, as measured by the azimuthal separation, ϕ_2, for the two pions is thus smeared.

FIG. 3.2

The azimuthal separations between particles in the 100020 class.

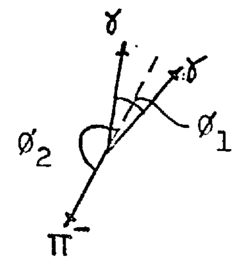

100020

N(ϕ_1)(0 to 10 counters)

N(ϕ_2) (0 to 10 counters)

Monte-Carlo

0	0	0	0	0	0	0	0	0	0	0
0	0	0	0	0	0	0	0	0	0	0
0	0	0	0	0	0	0	0	0	0	0
0	0	0	0	0	0	0	0	0	0	0
0	0	0	0	0	0	0	0	0	0	2
0	0	0	0	0	0	0	0	0	1	0
0	0	0	0	0	0	0	4	3	3	1
0	0	0	1	1	5	11	5	1	1	0
0	0	2	33	32	23	12	3	0	0	0
14	35	126	160	61	9	1	0	0	0	0
24	29	196	138	19	4	0	1	0	0	0

Data

0	0	1	0	0	0	2	1	0	1	1
1	1	0	1	0	4	0	1	0	2	0
1	0	1	0	0	0	1	0	1	2	0
1	1	0	2	2	1	0	0	2	1	0
0	0	2	1	1	1	7	1	0	1	3
0	1	1	2	0	1	4	0	2	2	0
0	0	1	1	1	3	2	1	1	4	2
1	1	2	3	3	5	5	3	4	3	2
1	2	2	6	14	7	2	6	0	5	0
3	6	16	38	19	8	5	1	6	1	0
10	6	33	17	5	3	2	2	0	2	1

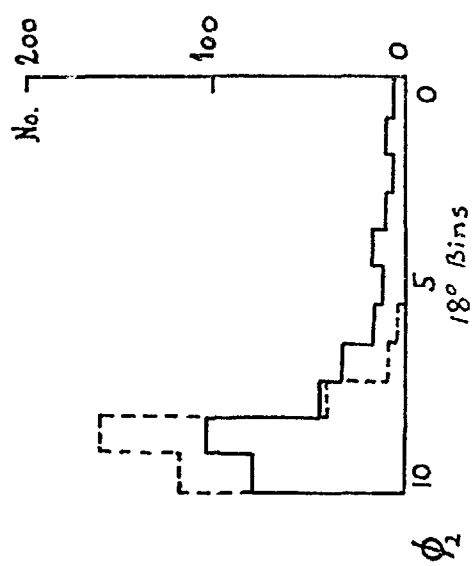

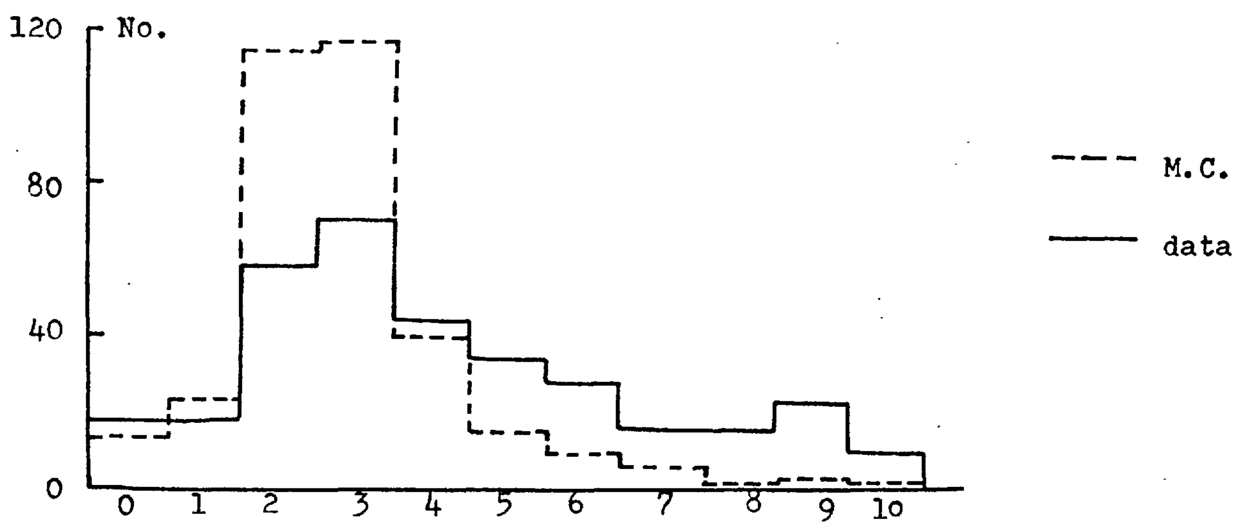

Azimuthal counter separation (18° bins), ϕ_1

In the analysis program events with separations of from seven to ten counters were selected for the 100020 classification. Fig.3.3A shows the data for the run at 1070 Mev/c after the cut on the separation between the gamma-rays has been made. Obviously there is evidence for a small non- $\pi^-\pi^0 p$ element at smaller separations. However, the shape of the distribution suggests that a relatively small background - constant over the plot - can reasonably be assumed. When such a background has been removed, the comparison between the data and the prediction for the selected events is quite good. This is illustrated in Fig.3.3B, where the distributions of the other sample data are also included. Again the same normalizing technique is used.

The estimated effect of this second selection at 1070 Mev/c was to remove a further 11 % of the signal remaining after the first cut.

The main conclusion from this study of the 100020 classification is that most of the non- $\pi^-\pi^0 p$ background was eliminated by the selections made on the data during analysis. When both cuts had been made, estimated backgrounds of $1.5 \pm 0.5\%$ and 8 ± 2 % of the selected 100020 signal remained at 755 and 1070 Mev/c respectively.

The 100010 classification merited special attention. Here one of the gamma-rays was not detected in the array: so only a cut on the azimuthal separation between the pion and the single gamma-ray was relevant. In the analysis program events

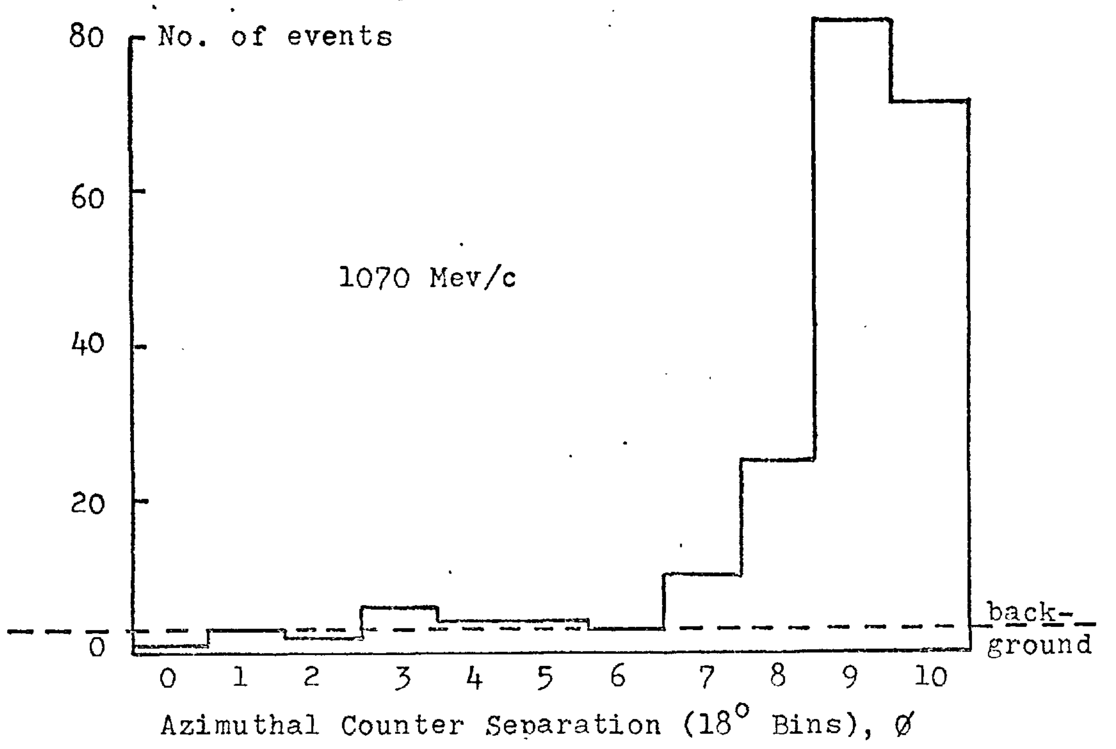

FIG. 3.3(A): The azimuthal counter separation, Ø, between the charged and the neutral pion for events in the 100020 classification.

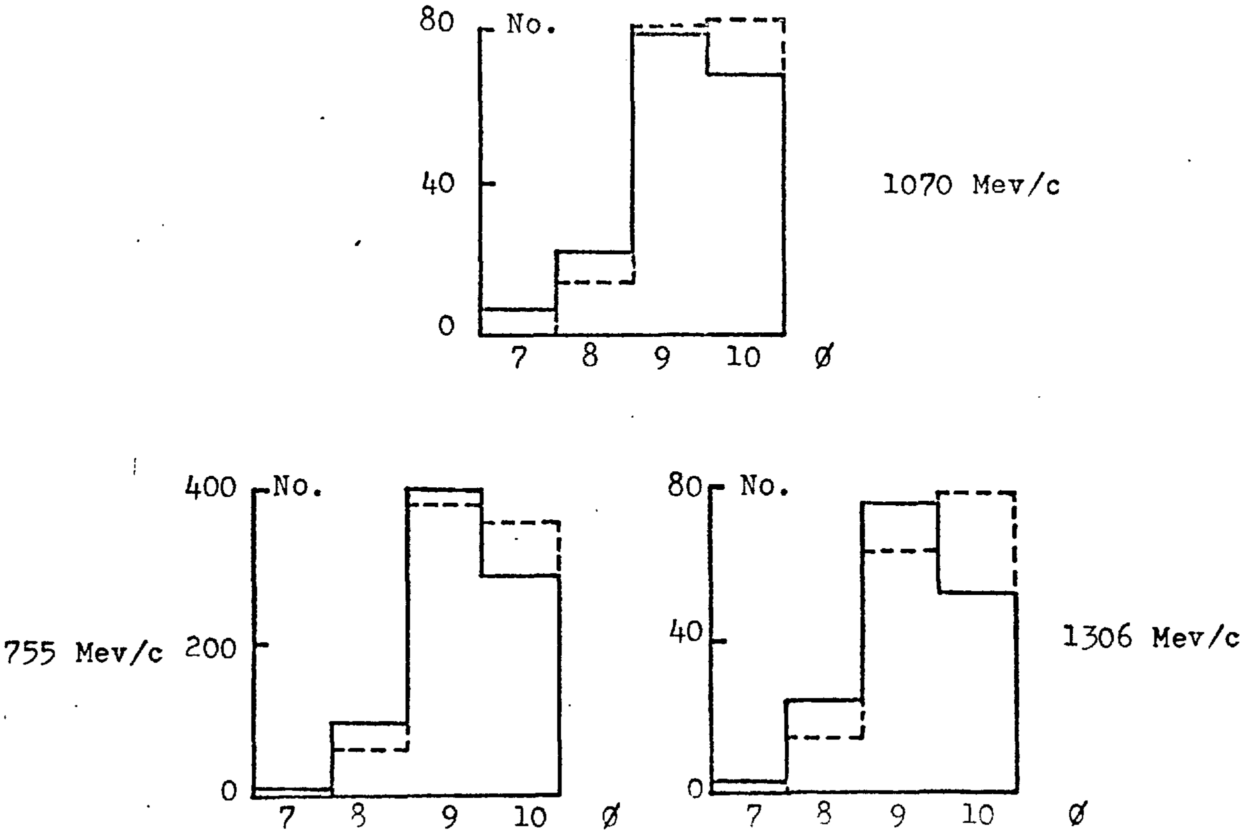

FIG. 3.3(B): The comparison between the data (solid lines) and the Monte-Carlo predictions (broken lines) after the cut $7 \leqslant \emptyset \leqslant 10$ counters has been made, and 'background' removed.

were selected for this class only if this separation was in the range from seven to ten counters - corresponding to the permitted range predicted for $\pi^-\pi^0p$ events by the Monte-Carlo program. Unfortunately this selection was not so effective in removing non-$\pi^-\pi^0p$ events from this class. In Fig.3.4A, for the data at 1070 Mev/c, the distribution of the separation shows that the $\pi^-\pi^0p$ signal in bins seven to ten is imposed on a fairly large contamination of unwanted events. But again by assuming a constant level of background across the distribution, and removing it, the remaining data is adequately fitted by the Monte-Carlo prediction, as demonstrated in Fig.3.4B for the three sets of sample data.

So to conclude, it is clear that by including events from the 100010 classification some non-$\pi^-\pi^0p$ background contamination was inevitable - even after the appropriate cut on the raw data had been made. For example, at 755 Mev/c the estimated background accounted for 8 $\pm$ 1 % of the total 100010 signal: at 1070 Mev/c it had risen to 34 $\pm$ 4 % .

Similar cuts on the distributions of events for inclusion in the 100001, the 100011 and the 120 classifications were used. At 1070 Mev/c the estimated contamination in the three modes was 22 $\pm$ 4 % of their combined total signal.

Taken as a whole, the selections made on the raw data did much to ensure that the contributions from the various classifications contained only a relatively small element of

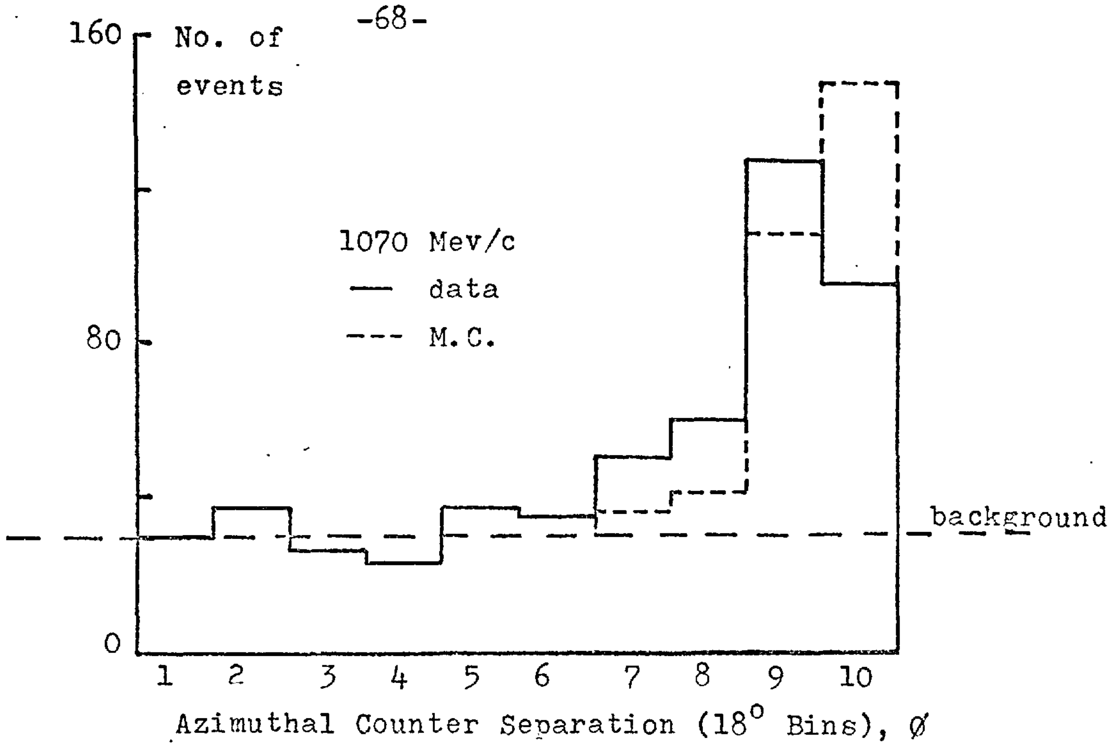

FIG. 3.4(A): The azimuthal separation, Ø, between the charged pion and the gamma-ray for events in the 100010 classification.

FIG. 3.4(B): The separation, Ø, after the cut $7 \leqslant \emptyset \leqslant 10$ counters has been made, and 'background' subtracted.

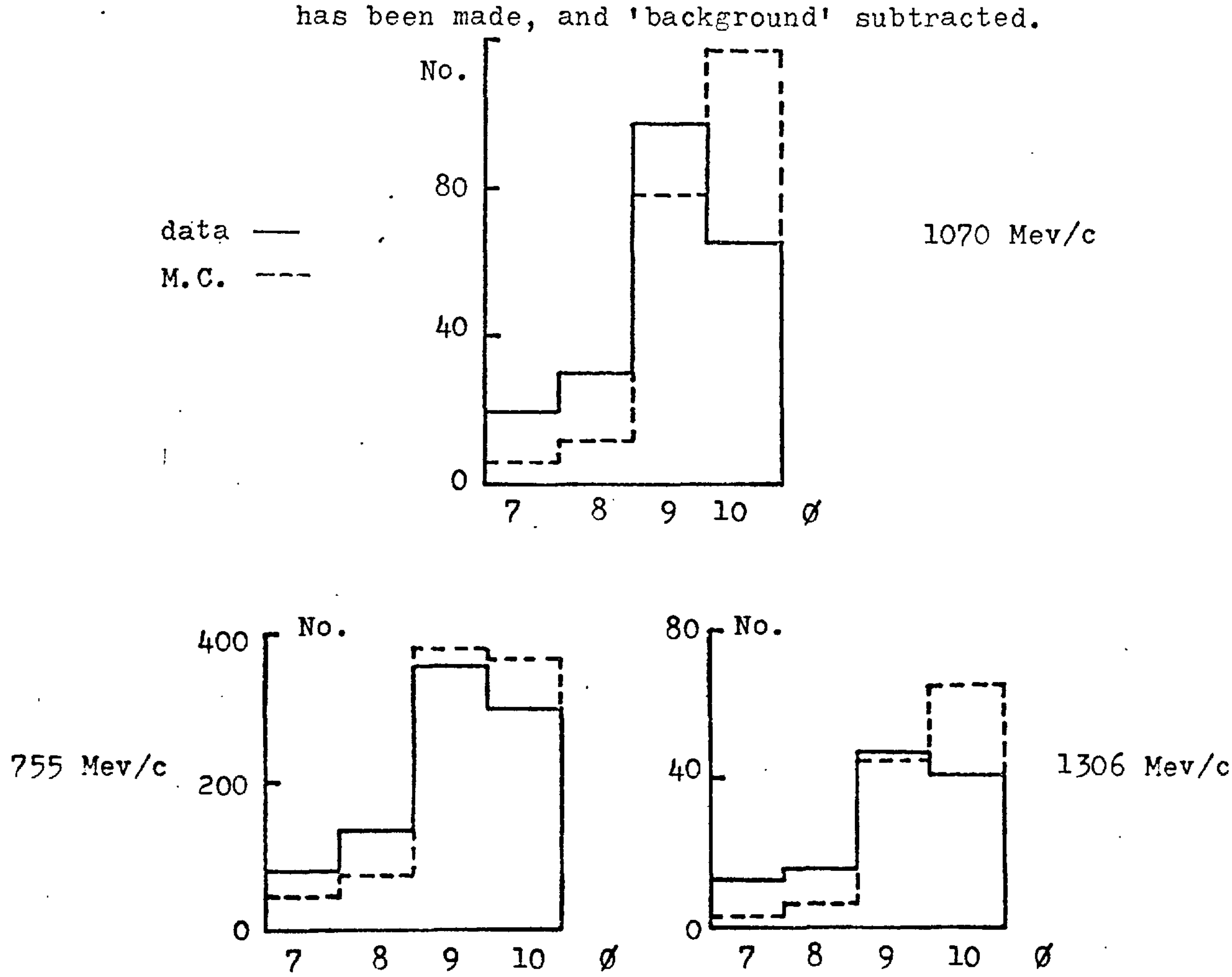

non-$\pi^-\pi^0 p$ events. The shapes of the distributions of the selected events were satisfactorily fitted by the Monte-Carlo predictions. Combining the signals of the five classifications used in the analysis program, KRUNCH, it was estimated that at 755 Mev/c some 4 ± 1 % of the total was due to background non-$\pi^-\pi^0 p$ events: at 1070 Mev/c the figure was 25 ± 2 %.

Selected events from the classifications 100020, 100011 and 000120 were also used as comprising events from the $\pi^-\eta p$, $\eta \rightarrow \gamma\gamma$ channel. Such events had to satisfy the following requirements: $5 \leqslant \phi_1 \leqslant 10$ counters, where ϕ_1 is the azimuthal separation between the two gamma-rays; and $6 \leqslant \phi_2 \leqslant 10$ counters, where ϕ_2 is the azimuthal separation between the charged pion and the bisector of the gamma-rays. From the Monte-Carlo program it was estimated that at 1070 Mev/c some 10 % of $\pi^-\pi^0 p$ events would "feed-through" into the selections used for the $\pi^-\eta p$ channel.

3.4.2 Comparative rates.

In fact many other aberrant classifications could be expected to include events from the $\pi^-\pi^0 p$ channel: 010020 and 001020 are just two possibilities. The final choice of the four used in the analysis was made by studying the relative rates of events in such possible classes. In the discussion which follows, appropriate cuts have been applied to the raw data, and the rates of the various classes were obtained from fixed timing gates. The following classifications were examined:

1: 100020 : a simple pion and two gammas;

2: 100010 : a simple pion and a single gamma;

3: 100001 : a simple pion and a double-gamma;

4: 100011 : a simple pion, a gamma and a double-gamma;

5: 000120 : a delta and two gammas;

6: 010020 + 010001 : a π-gamma and two gammas or a double-gamma;

7: 001020 + 001001 : a π-delta and two gammas or a double-gamma;

8: 000120 + 000101 : a delta and two gammas or a double-gamma.

In a first analysis no account was taken of the background contaminations remaining in the signals even after the relevant cuts have been made. A criterion for the inclusion of individual classes was therefore needed. This was established by demanding that when the classes were combined, the number of $\pi^-\pi^0 p$ events was greater than that of the background non-$\pi^-\pi^0 p$ contribution (here the two numbers add to give the total observed rate). This can be ensured if individual classifications each contribute more signal ($\pi^-\pi^0 p$ events) than background. This was taken as equivalent to requiring that the total rate in each classification was less than double its predicted value, when the absolute normalization was taken from a comparison of data with prediction for the "pure" 100020 mode.

Thus, table 3.1 shows the ratios of the observed total rates (obtained from SIP) compared to the rate of the 100020 class for the data at 755 and 1306 Mev/c. The predicted ratios (obtained from the Monte-Carlo simulation program) are also given. On the whole, there is good agreement - although the 100010 class at the higher momentum contains a good deal of background, as in fact anticipated from the study of the distributions of the azimuthal separations of the particles. However, no class would need to be vetoed on the "more background than signal" criterion.

TABLE 3.1

The observed and predicted ratios of the rates in various classifications containing $\pi^-\pi^0 p$ events to that in the 100020 mode: the rates were obtained for protons in the fixed timing gates shown.

Data at 755 Mev/c in a gate 12-22 ns. after the fast-peak.

Classification	Ratio	Data %	Prediction %
1 100020			
2 100010	2:1	110.0 ± 5.4	119.0 ± 6.1
3 100001	3:1	17.3 ± 1.5	19.9 ± 1.7
4 100011	4:1	17.4 ± 1.5	18.8 ± 1.6
5 000120	5:1	7.2 ± 1.0	7.2 ± 1.0
6 010020 + 010001	6:1	6.2 ± 0.9	6.1 ± 0.9
7 001020 + 001001	7:1	4.3 ± 0.7	4.6 ± 0.8
8 000120 + 000101	8:1	8.1 ± 1.0	8.9 ± 1.1

Data at 1306 Mev/c in a gate 10-22 ns. after the fast-peak.

Ratio	Data %	Prediction %
2:1	138.0 ±13.7	75.7 ± 3.9
3:1	33.9 ± 4.4	38.0 ± 2.1
4:1	36.2 ± 4.6	29.9 ± 1.9
5:1	9.2 ± 2.3	9.2 ± 1.0
6:1	9.2 ± 2.3	9.8 ± 1.1
7:1	8.6 ± 2.2	4.5 ± 0.7
8:1	14.4 ± 2.9	12.6 ± 1.2

As the analysis program was to include only five classifications containing events from the $\pi^-\pi^0 p$ channel, the "pure" 100020 and the four aberrant classes having the largest rates were chosen. The four were the 100010, the 100001, the 100011 and the 000120: the rate in the latter was just greater than that of any other single class, remembering that the rates in groups 6 to 8 were combinations, as seen in table 3.1.

In a second analysis these five classes were re-analysed, again using output from the program SIP. For each of them, the fraction of the total rate estimated to be contributed by non- $\pi^-\pi^0 p$ events was removed, leaving the rate of events from the $\pi^-\pi^0 p$ channel. The background estimates were calculated as before - that is by extrapolating a constant level obtained from the region of non- $\pi^-\pi^0 p$ events into the region where the $\pi^-\pi^0 p$ events were expected, on the plot of the dipion azimuthal separation (as in Fig.3.3A) or its equivalent (as in Fig.3.4A). Table 3.2 shows the results at 755 and 1306 Mev/c compared with the predictions of the Monte-Carlo. There is good agreement between the two.

In particular it should be noted that the studies of data at 755 Mev/c have shown that the number of events from the $\pi^-\pi^0 p$ channel which were not used by the analysis represented some 11 ± 1 % of the detected rate, while Monte-Carlo predicted 13 ± 1 % for this figure. Further studies revealed that another 9 ± 1 % was undetected as a result of vetoing events where the droop counters had been triggered, compared with a prediction of 10 ± 1 % . The agreement between these numbers illustrates that the Monte-Carlo provided a good estimate of the overall efficiency and performance of the decay array. As such, it may be used with some confidence to predict numbers used in the cross-section calculation at 755 Mev/c (see section 4.4.3).

TABLE 3.2

The predicted and observed ratios of the rates in classifications containing $\pi^-\pi^0p$ events to that in the 100020 mode. The rates were obtained for protons in the fixed timing gates shown: the observed rates have had the estimated background events removed: the classifications are those used in the data analysis program KRUNCH.

Data at 755 Mev/c in a gate 12-22 ns. after the fast-peak.

	Classification	Ratio	Data	Prediction
1	100020		%	%
2	100010	2:1	103 ± 6	119.0 ± 6.1
3	100001	3:1	17 ± 2	19.9 ± 1.7
4	100011	4:1	18 ± 2	18.8 ± 1.6
5	000120	5:1	7 ± 1	7.2 ± 1.0

Data at 1306 Mev/c in a gate 10-22 ns. after the fast-peak.

Ratio	Data	Prediction
2:1	78 ± 10	75.7 ± 3.9
3:1	32 ± 6	38.0 ± 2.1
4:1	38 ± 7	29.9 ± 1.9
5:1	7 ± 2.	9.2 ± 1.0

For protons detected in the range 0 to 30 ns. after the fast-peak, the Monte-Carlo predicts that an estimated 45 ± 1 % of all $\pi^-\pi^0$ decays are detected in the decay array at 755 Mev/c; at 1306 Mev/c the number is 48 ± 1 %, using these five classifications.

3.4.3 Consistency of the data.

To perform a rough check on the consistency of the data for the $\pi^-\pi^0p$ channel, for both 5 and 6 mt. sets, a simple test was used. Thus, curves of the ratios of the rates in the aberrant classifications to that in the "pure" 100020 mode were plotted against incident momentum for the sets of data in the region considered here. The yields in the cms gate were taken as the test rates - obtained directly from the output of the program that analysed the data summary tape. Although the data had of course been selected by the analysis program KRUNCH (using the cuts discussed in section 3.4.1), there still remained some contribution from non-$\pi^-\pi^0p$ events. So when comparing the curves with their Monte-Carlo equivalents, the factor of two limit (derived in section 3.4.2) was allowed above the predicted values before the data would become suspect, or be considered to include too much background.

To obtain better statistics the three smaller rates (table 3.2) were combined for one test, and the rate in the 100010 classification examined in another. The results (Fig.3.5) for the 5 mt. data show that it does constitute a consistent set. Similar results were obtained for the 6 mt. data.

3.5 The $\pi^+\pi^-n$ Channel.

Assuming neutron triggers, the "pure" classification 200000 - two simple (or charged) pions - is the most obvious candidate to comprise events from this channel.

Because they include events from the $\pi^+\pi^-n$ final

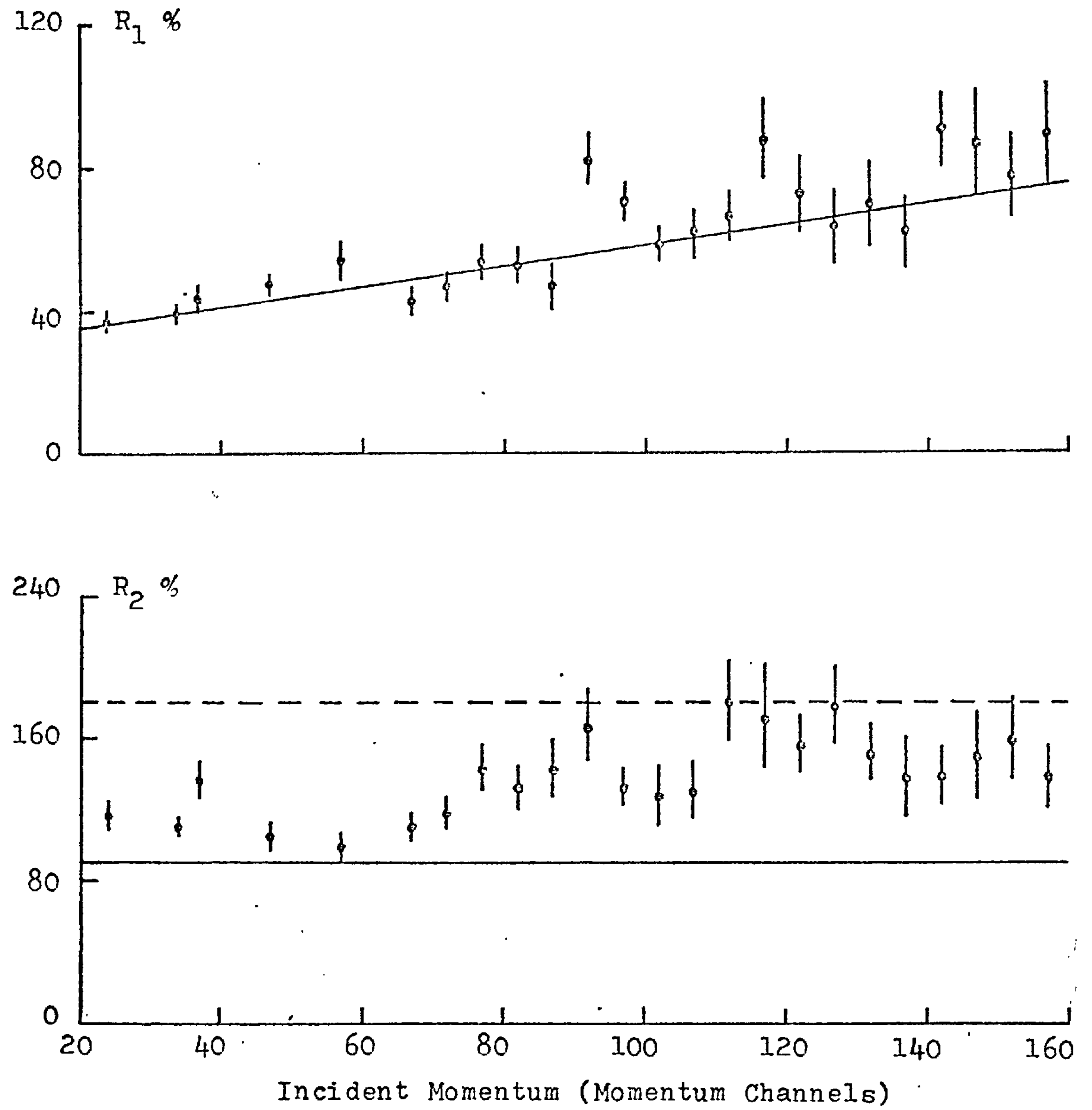

FIG. 3.5

Plots of the ratios $R_1 = \frac{\text{Rate}(100011 + 100001 + 120)}{\text{Rate}(100020)}$

and $R_2 = \frac{\text{Rate}(100010)}{\text{Rate}(100020)}$

as functions of incident momentum. The solid line is the corresponding Monte-Carlo prediction in each case, and the broken line the 'factor of two' limit.

state, the three following aberrant classifications were also used in its analysis:

	200100 :	two simple pions and an extra delta;
	110000 :	a simple pion and a π-gamma;
and	101000 :	a simple pion and a π-delta.

The analysis program had the facility of subdividing the rates in these four classes according to the polar regions where the particles were detected (the lid, cylinder, and for the 6 mt. data, the L counter region). However, the results presented here refer to rates integrated over the allowed polar regions. To provide compatibility with the results from the $\pi^-\pi^0p$ channel, events in which the droop counters had been triggered were vetoed. The Monte-Carlo program demonstrated that no pions should be detected in the ring counter - so the analysis program excluded from these classifications any events in which it had been triggered. The rate in the "pure" 200000 classification was dominant; the combined rates of the other three classes accounted for only some 30 % of that of the 200000.

Tests on the $\pi^+\pi^-n$ data closely followed the pattern for those on the $\pi^-\pi^0p$ data; runs at 673, 1097 and 1306 Mev/c in the 5 mt. set were used as the sample.

A necessary requirement for inclusion in any of the four classifications was demanded of the azimuthal separation between the two pions. The Monte-Carlo simulation showed that separations of less than nine counters were not allowed for events in the $\pi^+\pi^-n$ channel. Thus the analysis program selected only those having separations of nine or ten counters. Fig.3.6A shows the distribution for the raw data in the 200000 class obtained from SIP for the run at 1097 Mev/c. Obviously there is a small non- $\pi^+\pi^-n$ element at smaller separations which the cut used in the KRUNCH analysis would remove. Assuming a constant level of this background over the distribution, it was estimated that some 5 ± 1 % of the selected events was contamination. Fig.3.6B shows the comparison between the data and the prediction after this background has been removed. Figs.3.6C and D show the same plots for the combined aberrant classifications; it was estimated that about 7 ± 1 % of the events selected for these classifications were not $\pi^+\pi^-n$. (The predicted histograms shown in the figures have again been normalized to contain the same numbers of events as the data plots.)

When all four classifications were added, about 5 ± 1 % of the total selected rate was thought to be due to non- $\pi^+\pi^-n$ events.

The relative rates in the three aberrant classes were also examined, and compared with the predictions of the Monte-Carlo simulation. As before, background events were removed, and the resulting rates in fixed timing gates were compared to that in the "pure" 200000 mode. The ratios thus obtained were then checked against their Monte-Carlo equivalents. Table 3.3 shows the results, and agreement between the two is good.

FIG. 3.6

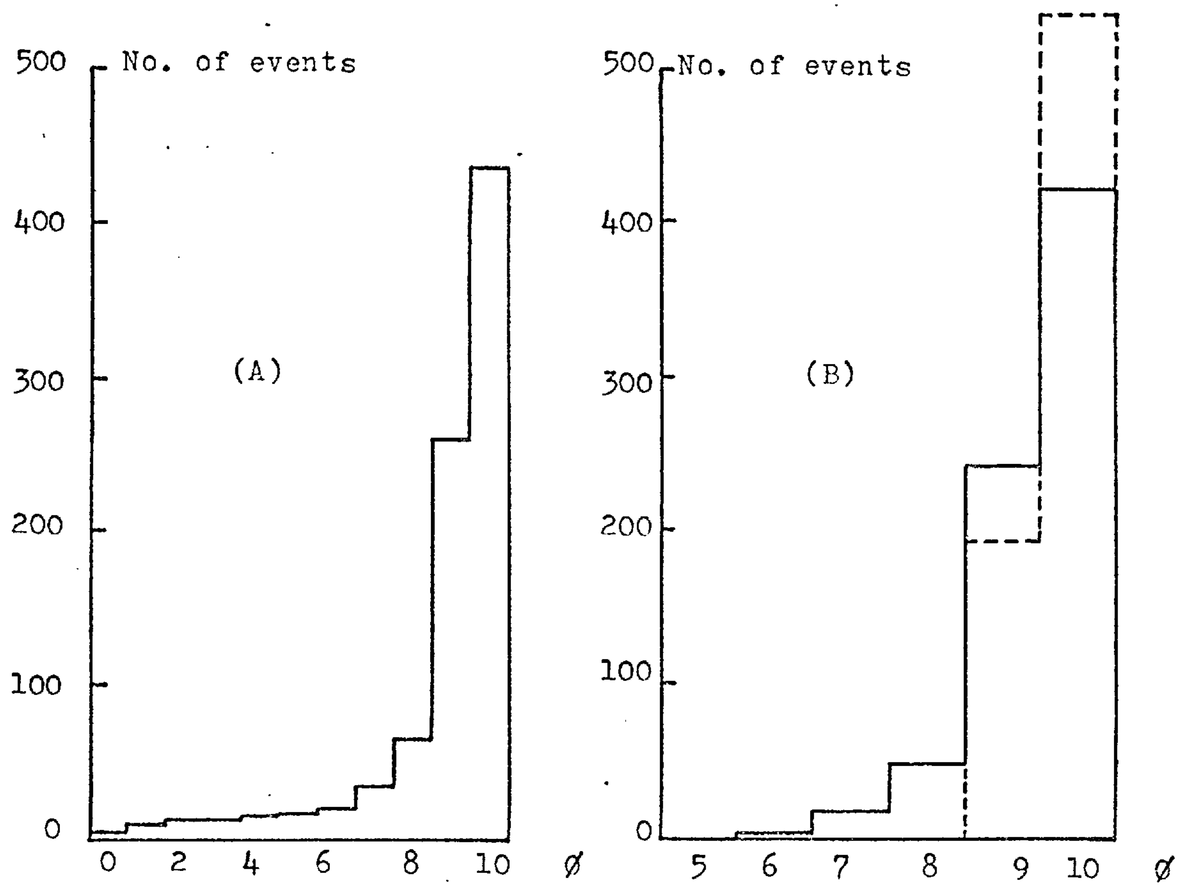

The azimuthal counter separation, Ø, in 18° bins, between the two charged pions for events in the 200000 classification, before (A) and after (B) background subtraction; the prediction (broken line) is also shown in (B).

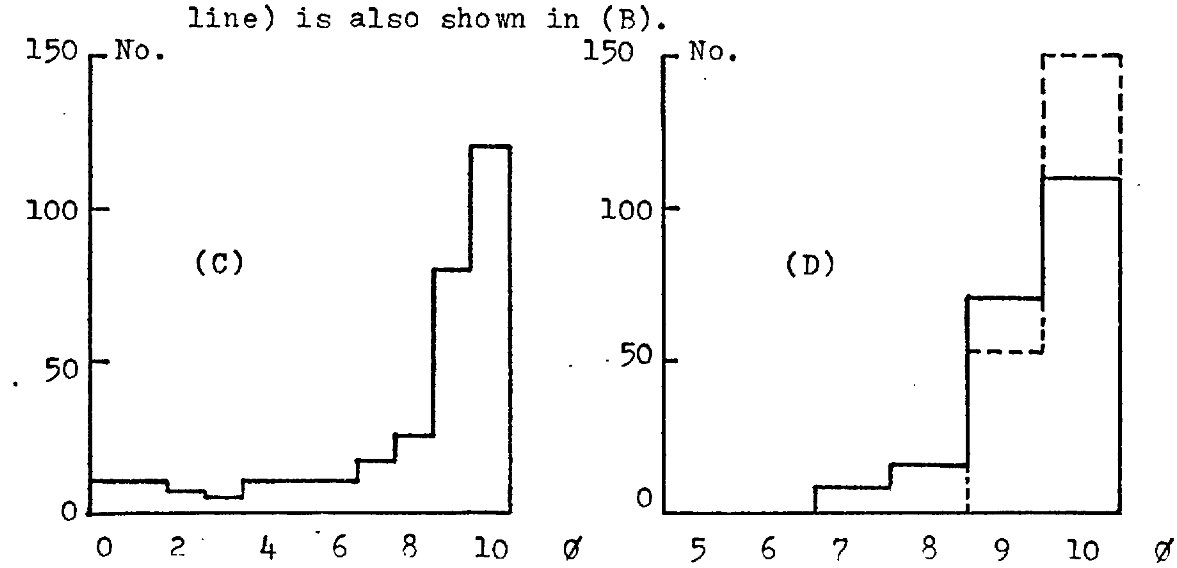

The azimuthal counter separation, Ø, in 18° bins, between the two charged pions for events in the combined aberrant classifications containing $\pi^+\pi^-n$ events, before (C) and after (D) background subtraction; the prediction (broken line) is shown in (D).

TABLE 3.3

The predicted and observed ratios of the rates in classifications containing $\pi^+\pi^-n$ events to that in the 200000 mode. The rates were obtained for neutrons in the fixed timing gates shown: the observed rates have had the estimated background events removed: the classifications are those in the data analysis program KRUNCH.

Data at 673 Mev/c in a gate 10-20 ns. after the fast-peak.

	Classification	Ratio	Data	Prediction
1	200000		%	%
2	110000	2:1	10 ± 1	11.2 ± 0.8
3	101000	3:1	5 ± 1	6.0 ± 0.6
4	200100	4:1	7 ± 1	6.4 ± 0.6

Data at 1097 Mev/c in a gate 10-20 ns. after the fast-peak.

Ratio	Data	Prediction
2:1	10 ± 1	11.7 ± 0.7
3:1	7 ± 1	8.3 ± 0.6
4:1	10 ± 1	7.7 ± 0.6

Data at 1306 Mev/c in a gate 7-15 ns. after the fast-peak.

Ratio	Data	Prediction
2:1	12 ± 1	18.0 ± 2.0
3:1	8 ± 1	9.9 ± 1.5
4:1	8 ± 1	11.0 ± 1.6

For neutrons detected in the range 0 to 30 ns. after the fast-peak, the Monte-Carlo predicts that an estimated 58 ± 1 % of all $\pi^+\pi^-$ decays are detected in the array at 1306 Mev/c using these four classifications.

Finally, the data was subjected to a consistency test: the combined yield in the cms gate for the three aberrant classifications was compared with that for the "pure" 200000 mode, and this ratio plotted as a function of incident momentum. The plot for the 5 mt. data set is shown in Fig.3.7; the figure also shows the Monte-Carlo prediction for the curve, together with the factor of two limit beyond which the data would either become suspect or thought to contain too much background. The results suggest that the data constitute a consistent set. Similar results were obtained for the 6 mt. set.

The main conclusion from this study is that the combination of classifications used by the analysis program KRUNCH to identify events in the $\pi^+\pi^-n$ channel was at the same time efficient in rejecting background contamination from this selection.

When KRUNCH had analysed all the raw data tapes, and for each momentum run written the set of ninety time-of-flight spectra on the DST, it was possible to study different final states individually. Thus at each momentum, by adding together the spectra of the five classifications used to identify events in the $\pi^-\pi^0p$ channel, a single spectrum composed mainly of such events was produced. From such spectra yield curves and mass plots could be generated. An exactly similar procedure was followed for the $\pi^+\pi^-n$ channel.

FIG. 3.7

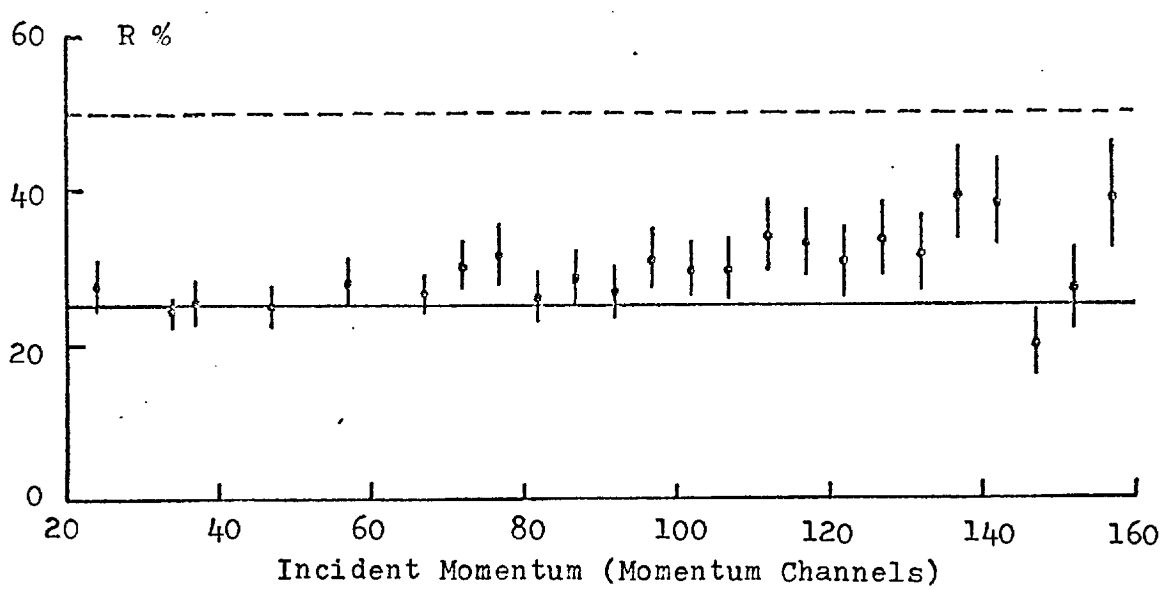

Plot of the ratio $R = \dfrac{\text{Rate}(110000 + 101000 + 200100)}{\text{Rate}(200000)}$

as a fuction of incident momentum. The solid line is the Monte-Carlo prediction, and the broken line the 'factor of two limit'.

Chapter Four

Enhancements in the yield curve of the $\pi^-\pi^0$ p final state.

4.1 Introduction.

The results are presented in the form of yield curves for the two single pion production channels $\pi^-p \rightarrow \pi^-\pi^0 p$ and $\pi^+\pi^- n$. Fig.4.1 shows the curves obtained from the yields in the cms gate for the 5 mt. data: to achieve better statistics, the yields in the five momentum channels of each run have been added together, and normalized to a rate of 100 million incident pions. The error bars represent the statistical errors involved. Positions of the currently established (5) N^* and Δ resonances in this momentum range are also indicated; the notation is the standard, L2I2J, where L is the orbital and J the total angular momentum, and I is the isotopic spin.

The most striking features in the yield curve of the $\pi^-\pi^0$ p channel are the large enhancement at an incident momentum of approximately 750 Mev/c, and a smaller structure at about 1070 Mev/c. These momenta correspond to centre-of-mass energies of approximately 1520 and 1710 Mev, respectively, the latter equivalent to a missing mass of 765 Mev/c^2. In the yield curve of the $\pi^+\pi^-$ n channel there is a much less pronounced structure (slightly displaced) corresponding to the large one in the $\pi^-\pi^0$ p channel; a broad structure at a slightly higher momentum; and no visible enhancement at 1070 Mev/c to correspond to the smaller one in $\pi^-\pi^0$ p.

Part of this momentum range was "re-scanned" with

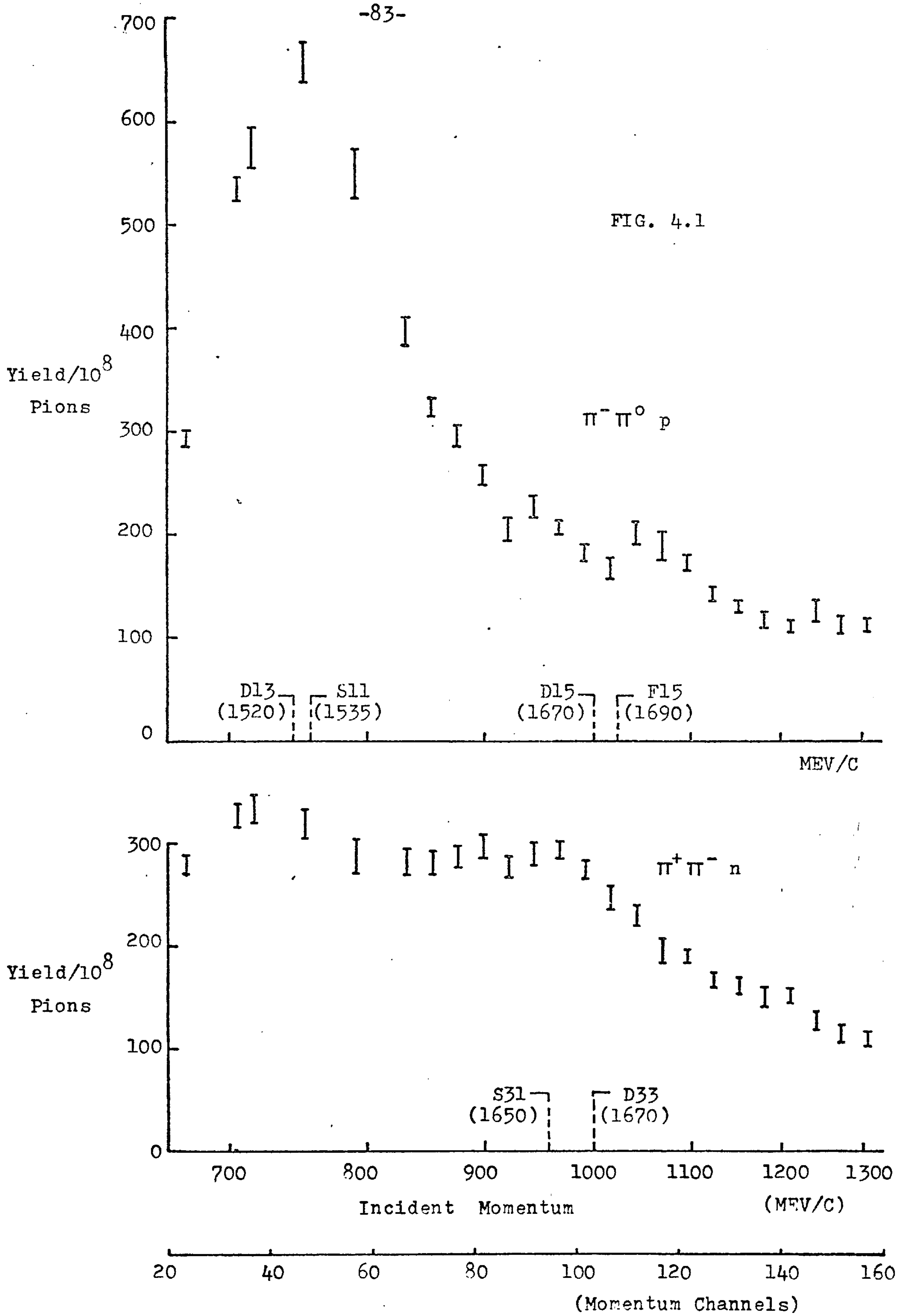

The yield curves generated from the cms gate for the 5 mt. data for the single pion production channels shown.

the neutron counters a further metre downstream of the target. The yields from the cms gate for the same two channels are shown in Fig.4.2. They appear similar to those obtained from the 5 mt. data. In particular, in the yield curve of the $\pi^- \pi^0 p$ channel there is again a very clear enhancement at 1070 Mev/c, but no evidence for a corresponding structure in the $\pi^+ \pi^- n$ channel.

To interpret such structure in terms of either meson resonance production or nucleon resonance formation, it was necessary to study yield curves generated from a variety of different timing gates. Before describing the results of such studies, the programs which were used to simulate the effects of the two types of resonance, and to predict the differences in behaviour between them, are outlined in the following two sections.

4.2 The Program to simulate the effects of Meson Resonance Production in the Yield Curve.

Recalling the discussion of section 1.2, it was shown that, for a reaction of the type $\pi^- + p \longrightarrow X + N$, the missing mass M of the group of particles X could be written

$$M = M(p, p_N, \theta)$$

where p and p_N are the momenta of the incident pion and the recoiling nucleon respectively, and θ is the angle between the two. At a fixed angle θ, and with $p_N = p_N(t)$,

FIG. 4.2

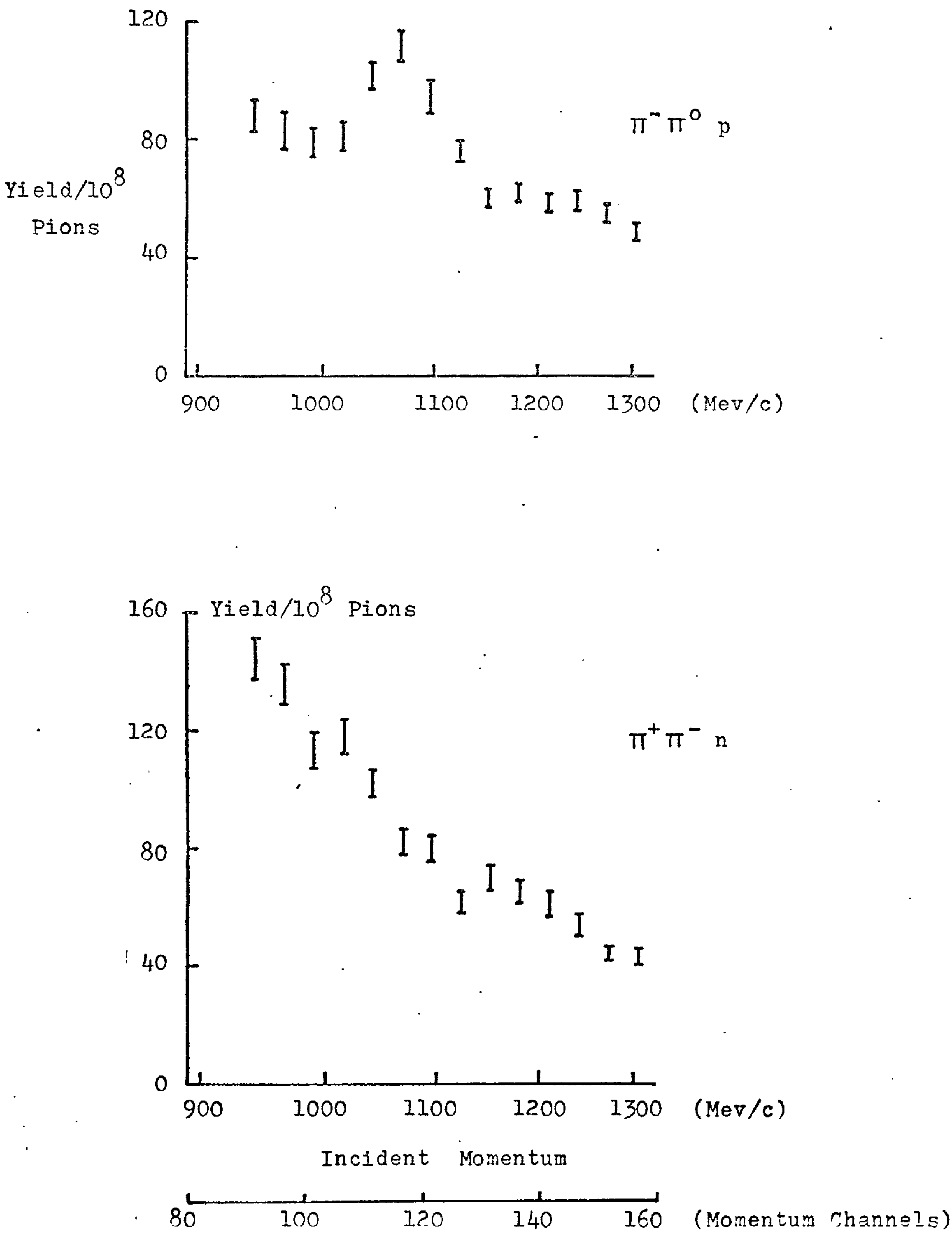

The yield curves generated from the cms gate for the 6 mt. data, for the single pion production channels shown.

$$M = M(p,t)$$

where t is the time-of-flight of the recoiling nucleon.

In a counter subtending a small solid angle $\delta\Omega$ at the target, and in a small interval of time δt, the counting rate of nucleons produced in such reactions can be written

$$d^2R \propto \frac{d^2\sigma}{dt\,d\Omega} \,.\, \delta t \,.\, \delta\Omega \,, \text{ with } \delta\Omega = \delta\cos\theta \,.\, \delta\phi.$$

Using a suitable Jacobian transformation, the differential cross-section can be replaced by an invariant equivalent, so that

$$d^2R \propto \frac{d^2\sigma}{dT\,dM} \,.\, J \,.\, \delta t \,.\, \delta\Omega$$

where $J = \dfrac{\partial(T,M)}{\partial(t,\Omega)}$ is the relevant Jacobian.

and T and M are the invariant 4-momentum transfer and missing mass respectively. The yield in the neutron counters of this experiment in a timing gate t_2-t_1 may therefore be expressed as the integral

$$\text{yield} \propto \int d^2R \propto \iint_{\Omega\ t_1}^{t_2} \frac{d^2\sigma}{dT\,dM} \,.\, J.\ dt \,.\, d\Omega \qquad \text{...........(4.1)}$$

The integration over solid angle is trivial, and can be absorbed into the proportional sign.

To make further progress, a particular form for the differential cross-section must be chosen. Now if X in the interaction represents a meson resonance of mass M_0 and width Γ_0, the simplest form will be such that:

(1) at fixed T,

$$\frac{d\sigma}{dM} = \frac{A}{A + (M - M_0)^2} \quad , \text{ with } A = (\Gamma_0/2)^2;$$

(2) at fixed M,

$$\frac{d\sigma}{dT} = C \qquad \text{with } C = \text{constant.}$$

The first form assumes a simple Breit-Wigner resonance; the second that the resonance is produced isotropically in the c-system. This is not unreasonable since its momentum p^* is so small - for example in the cms gate $p^*c \leq 40$ Mev. So on a simple impact parameter model, assuming a typical interaction radius of $\hbar/m_\pi c$, the approximation

$$\frac{40.\hbar}{m_\pi c^2} \simeq n\hbar \quad , \quad \text{where n is an integer,}$$

is only satisfied for n = 0, corresponding to S-wave, isotropic production.

The differential cross-section can then take the form:

$$\frac{d^2\sigma}{dTdM} = \frac{C.A}{A + (M - M_0)^2} = C.BW_m(M) \quad ......(4.2)$$

Remembering that $M = M(p,t)$,

$$\frac{d^2\sigma}{dTdM} = C.BW_m(p,t)$$

Furthermore, after the necessary algebra, the Jacobian J reduces to

$$J = \frac{1}{2\pi}\begin{vmatrix} \frac{\partial T}{\partial t} & \frac{\partial T}{\partial \cos\theta} \\ \frac{\partial M}{\partial t} & \frac{\partial M}{\partial \cos\theta} \end{vmatrix} = \frac{1}{2\pi}\cdot\frac{2.m_p.p.p_N^4}{m_N^2.t_\gamma.M} \quad .....(4.3)$$

where t_γ is the time-of-flight of gamma-rays and m_p and m_N are the masses of the proton and recoiling nucleon respectively. So,

$$J = J(p,t).$$

The function Y(p) representing the yield curve for meson production is therefore given by

$$Y(p) \propto \int_{t_1}^{t_2} BW_m(p,t).J(p,t).dt \quad ...(4.4)$$

absorbing the constant C into the proportion sign.

The position of the peak in the yield curve due to the presence of the meson resonance will therefore occur at the value of incident momentum p which makes the function Y(p) a maximum.

In chapter one it was shown that such a peak occurs at different p in yield curves generated from the yields in different timing gates (simply by looking at the kinematics curves of Fig.1.3). This can be examined more rigorously as follows: consider the yield curve $Y(p,t_o)$ produced from yields in an infinitesimal gate δt at t_o :

$$Y(p,t_o) \propto J(p,t_o).BW_m(p,t_o).\delta t$$

For a zero-width resonance - or if J were independent of p - the maximum value of the function $Y(p,t_o)$ will occur at the maximum of $BW_m(p,t_o)$. This is obviously satisfied at $p = p_o$ for which

$$M = M(p_o,t_o) = M_o \text{ , the meson mass.}$$

For a curve $Y(p,t_1)$ generated from yields in a similar gate δt at t_1, the maximum will no longer occur at $p = p_o$, since,

$$M = M(p_o,t_1) \neq M_o$$

However, in general, p can be re-chosen so that at $p = p_1$

$$M = M(p_1,t_1) = M_o \quad ,$$

thus making $Y(p,t_1)$ its maximum - that is $Y(p_1,t_1)$. In other words, the position of the peaks in the yield curves for infinitesimal gates at t_o and t_1 occur at momenta p_o and p_1 respectively; separated that is by a momentum $p_1 - p_o$.

But in fact J is not independent of p - it is a slowly-varying, well-behaved function of it - and resonances do not have zero-widths. Moreover, for all practical purposes it is only possible to evaluate yields in gates of finite widths $t_2 - t_1$:

$$Y(p,t_2-t_1) \propto \int_{t_1}^{t_2} BW_m(p,t).J(p,t).dt \quad ......(4.5)$$

This infers that the position of the peak in the yield curve - and hence its movement as a function of timing gate - is not necessarily prescribed by the kinematics curves. In fact, the only reliable way of predicting the position of the meson - and its movement as a function of timing gate - is to perform integrations like those of equation (4.5) over a suitable range of values of p suggested by the kinematics curves.

In the program to simulate the effects of meson resonance production in the yield curve, the integrations like those in equation (4.5) were performed numerically. The values of t_1, t_2, M_0 and Γ_0 were used as input to the program. At each momentum the timing interval $t_2 - t_1$ was divided into an even number of small intervals, and the value of $BW_m(p,t).J(p,t)$ evaluated at each abscissa thus produced, by using equations (1.2), (4.2) and (4.3). The area under the curve $Y(p,t_2-t_1)$ was then calculated using Simpson's formula (17). To allow for the uncertainty in the measurement of the nucleon time-of-flight, the gate limits were readjusted to t_1-3dt and t_2+3dt, where dt is the timing uncertainty ($\pm$0.6 ns.). To allow for the spread in the beam momentum in each channel, the yield was taken to be the sum of three integrations:

$$\text{simulated yield} = Y(p_i) + \tfrac{1}{2}\left(Y(p_i+dp_i/2) + Y(p_i-dp_i/2) \right)$$

where p_i is the central momentum of channel i, and the full-width at half-height dp_i of the momentum distribution in the channel is such that $dp_i/p_i = \frac{1}{2}$ %.

From such calculations, the effect of the magnitude of Γ_0 was found to be important only in the cms gate. This is illustrated in Fig.4.3: here the predicted separation between peaks due to meson production, in yield curves generated from two different fixed gates, is plotted as a function of meson width Γ_0. As can be seen the separation is independent of Γ_0. The figure also shows the predicted separation for yields in the cms and a fixed gate: in this case the separation decreases as Γ_0 is increased.

4.3 The Program to Simulate the Effects of Nucleon Resonance Formation in the Yield Curve.

For interactions of the type

$$\pi^- + p \longrightarrow N^* \longrightarrow \pi\pi N$$

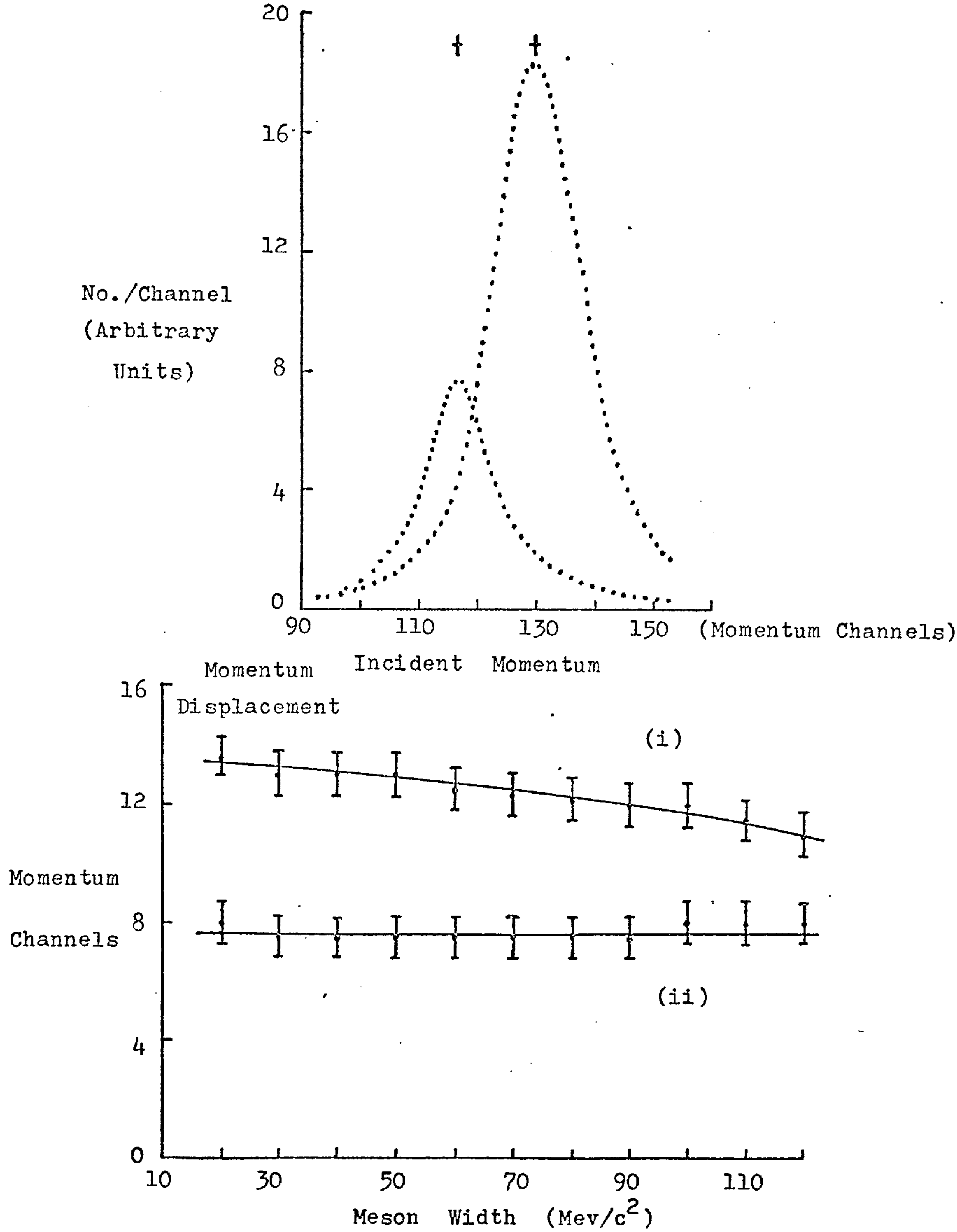

FIG. 4.3

The curves in the upper graph are the simulated yield curves generated from two different timing gates for a meson of mass 765 Mev/c^2. In the lower graph, the displacement between the peaks in such curves is plotted against the meson width; for (i) the displacement between the peaks in the yield curves from the cms and a fixed gate; and for (ii) between peaks in yield curves from two different fixed gates.

the simple model used to predict the effect of such a nucleon resonance in the yield curve assumed that it decayed according to an isotropic, 3-body phase space distribution in the c-system.

The program which simulated this effect was a slightly generalized version of that used in the studies of the detection efficiency of the decay array (section 3.3). Now, however, the nucleon was produced isotropically in the c-system.

Pions from the incident beam - assumed to have a triangular distribution in momentum with a full-width at half-height of ½ % - were allowed to interact with equal probabilities anywhere along the length of the target. Using the conservation of 4-momentum, events in the final 3-body state were then uniformly generated in the KE_2- KE_3 space of the c-system (KE_i is the kinetic energy of particle i). Events were firstly restricted to the rectangle defined by

$$KE_2 = 0 \ , \ KE_2 = KE_{2max}$$
$$KE_3 = 0 \ , \ KE_3 = KE_{3max}$$

and those generated outside the Dalitz boundary - essentially defined by the incident pion momentum - were then discarded. For those remaining, the particles were rotated about a randomly chosen direction to ensure that none had a preferred direction in the c-system, and finally transformed back to the laboratory system.

The six neutron counters were represented by a single annular disc: a nucleon directed towards the face of this disc was detected irrespective of its charge. The true time-of-flight was adjusted by adding a timing error with a gaussian distribution of standard deviation dt = 0.6 ns. corresponding to the instrumental uncertainty.

The interaction of the pions with the decay array was treated exactly as described before (section 3.3).

For events in which the nucleon was detected, various time-of-flight spectra were produced, and classified, as in the data, according to the state of the decay array. These were then combined to represent the single time-of-flight spectra of each of the two single pion production channels.

By using the program at several incident momenta, simulated yield curves of the 3-body phase space production process could be obtained from such spectra. The following definitions were used for a given incident momentum:

c_1 : the number of events for which the nucleon is detected per fixed number of incident pion attempts;

c_2 : the fraction of events in c_1 for which the pions are also detected;

$c_3(t_2-t_1)$: the fraction of events in c_2 where the nucleons have times-of-flight in the gate t_2-t_1.

It follows from these definitions that

$c_1.c_2.c_3(t_2-t_1)$ = the number of events per fixed number of attempts for which all three decay products are detected and the nucleon time-of-flight is in the gate t_2-t_1.

So,

$$c_1.c_2.c_3(t_2-t_1) = \text{the simulated yield in that gate} = PS(t_2-t_1).$$

Two further definitions were also useful:

$f_1(t_2-t_1)$: the fraction of events in c_1 for which the nucleons have times-of-flight in the gate t_2-t_1;

$f_2(t_2-t_1)$: the fraction of events in f_1 for which the two pions are also detected.

From these definitions it is obvious that the predicted yield in gate t_2-t_1 is

$$PS(t_2-t_1) = c_1.c_2.c_3(t_2-t_1) = c_1.f_1(t_2-t_1).f_2(t_2-t_1).$$

These parameters have been studied using the results of the Monte-Carlo program at a series of incident momenta, to investigate the overall detection efficiency of the system to the three-body $\pi\pi N$ final state. Fig.4.4 shows curves of c_1, $c_1.c_2$ and PS = $c_1.c_2.c_3$ for the $\pi^-\pi^0 p$ channel. The curves of c_1 and $c_1.c_2$ are of course independent of timing gate; PS has been plotted for two timing gates (the cms gate and one 20 to

26 ns. after the fast-peak have been shown as typical examples). For all gates except the cms, PS decreases with increasing incident momentum p; but since the limits of the cms gate were chosen to vary with p (section 1.4.1) the yields predicted for this gate turn out to be independent of it.

To complete the picture, Fig.4.5 shows the curves of the parameter f_2 for two fixed gates at 9 to 12 and 20 to 26 ns. after the fast-peak. As can be seen, the detection efficiency of the two pions ($\pi^-\pi^0$) is independent of the incident momentum, except in the faster gate at the lowest momenta ($<$ 750 Mev/c.). Here the nucleon accounts for most of the available energy; in consequence the other particles are not detected with full efficiency, since they do not always have sufficient energy to trigger the counters in the decay array.

With this simple model, the predicted yield curve $Y(p,t_2-t_1)$, generated from the yields in the gate t_2-t_1 for a nucleon resonance of mass M_s and width Γ_s, would have the form:

$$Y(p,t_2-t_1) \propto BW_s(p).PS(p,t_2-t_1)$$

with

$$BW_s(p) \propto \frac{A}{A + (E^* - M_s)^2} \quad , \quad A = (\Gamma_s / 2)^2$$

and $E^* = E^*(p)$, the centre-of-mass energy of the system.

Obviously if PS were independent of p (as is in fact the case for yields in the cms gate), the position of the maximum of the function $Y(p,t_2-t_1)$ would occur at the value of

FIG. 4.4

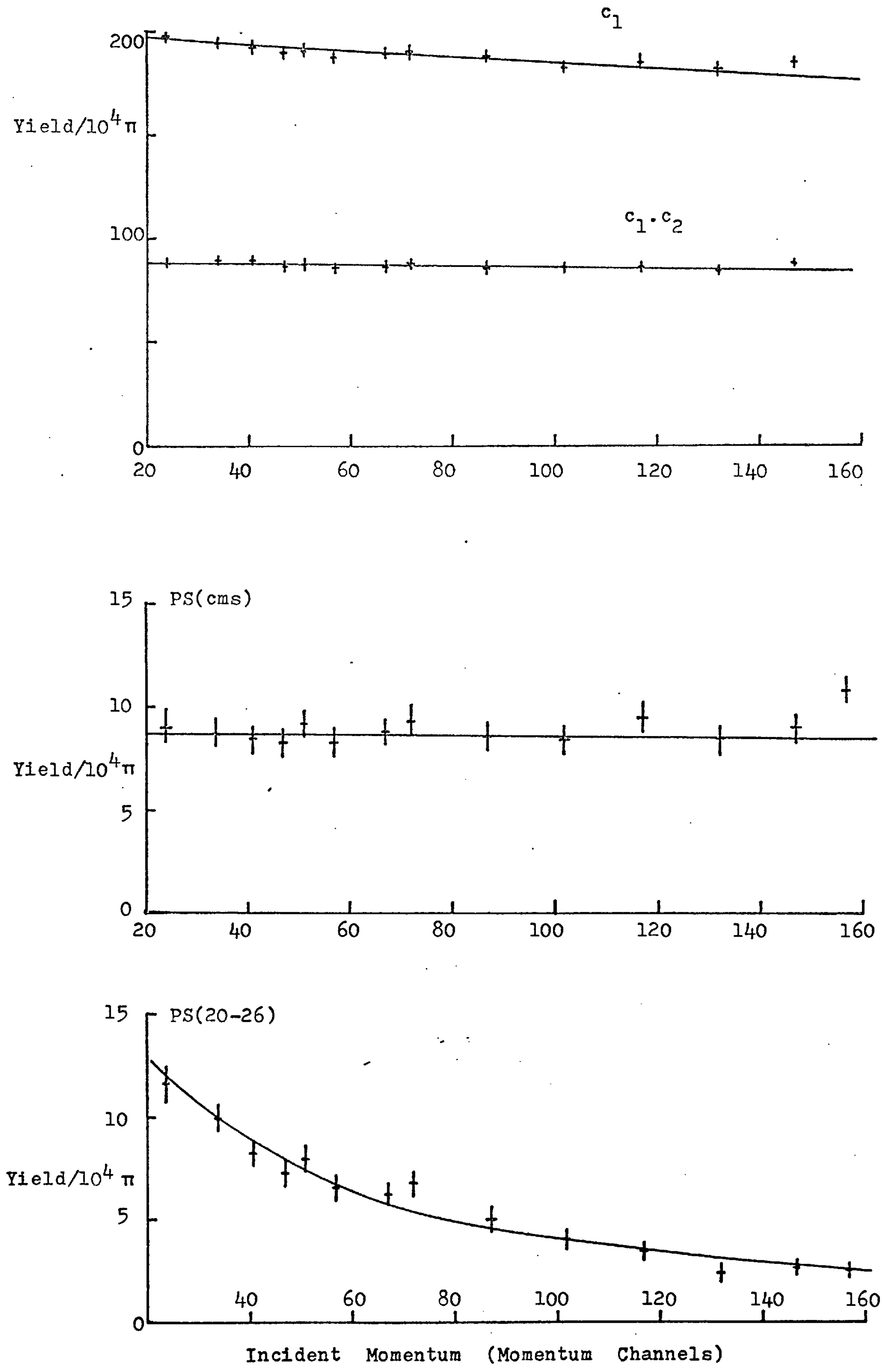
c_1
$c_1 \cdot c_2$
200
100
0
Yield/$10^4\pi$
20
40
60
80
100
120
140
160
PS(cms)
15
10
5
0
Yield/$10^4\pi$
20
40
60
80
100
120
140
160
PS(20-26)
15
10
5
0
Yield/$10^4\pi$
40
60
80
100
120
140
160
Incident Momentum (Momentum Channels)

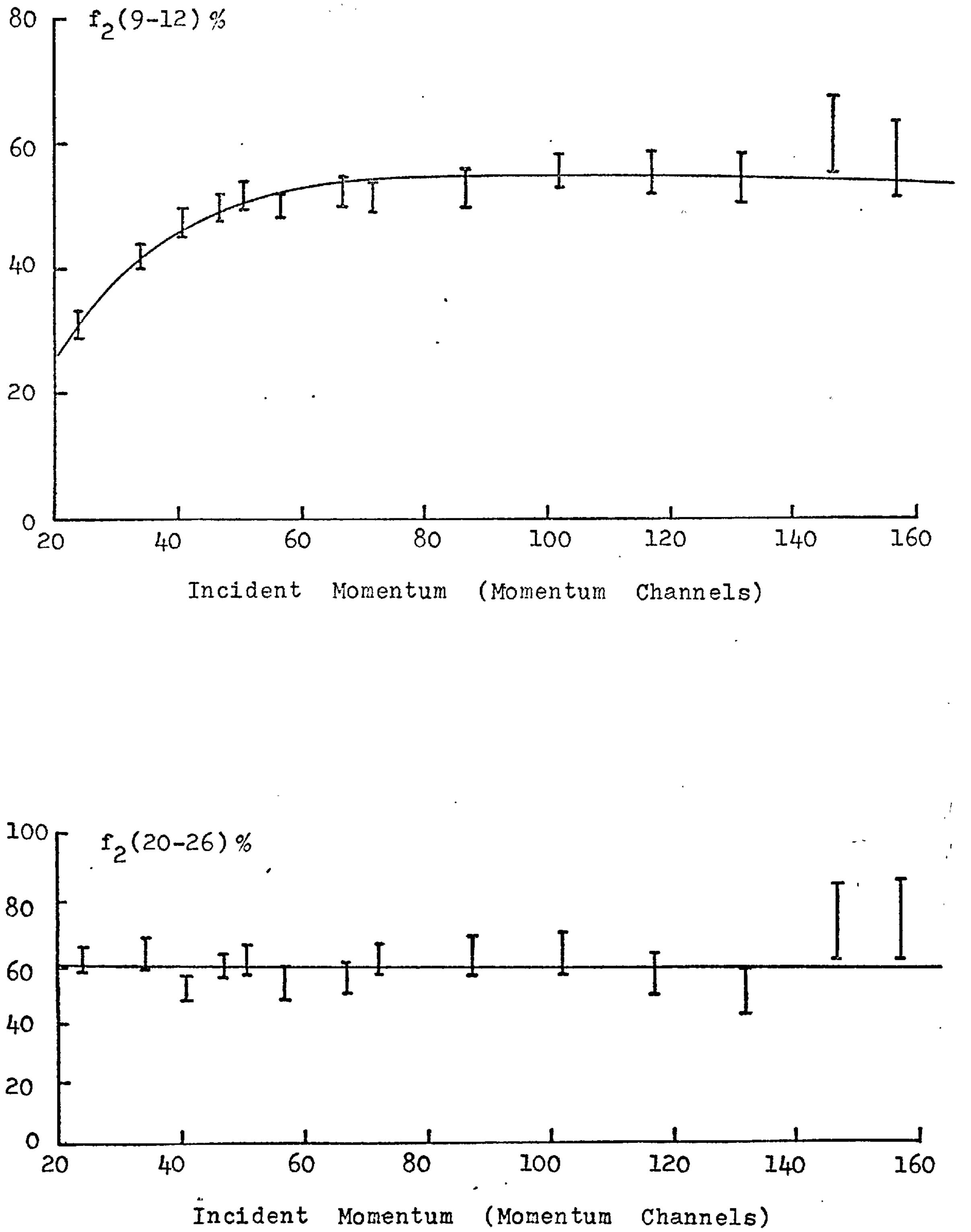

FIG. 4.5

Plots of $f_2(t_2-t_1)$, the detection efficiency of the $\pi^-\pi^0$ dipion for nucleons in the gate t_2-t_1, against incident momentum.

p which makes $BW_s(p)$ its maximum. This is satisfied at $p = p_s$ for which $E^*(p) = E^*(p_s) = M_s$, the resonance mass. Now $BW_s(p)$ does not depend on the choice of the timing gate t_2-t_1; so it is clear that the momentum at which the maximum occurs in the yield curve generated from a different timing gate would be the same (p_s), a result anticipated in section 1.5. The dependence of PS on the incident momentum p , however, can slightly modify this conclusion (see section 4.4.1).

For a process involving direct s-channel nucleon resonance formation and associated meson resonance production, the function representing the yield curve would include terms like $BW_s(p)$ and $BW_m(p,t)$. The presence of the latter would be enough to ensure that the part of the enhancement due to the production of the meson would occur at different momenta in yield curves generated from different timing gates; its magnitude would be modulated by the strength of the term $BW_s(p)$.

4.4 The Analysis of the Enhancement in the $\pi^-\pi^0 p$ Channel at a Centre-of-Mass Energy of 1520 Mev.

4.4.1 Yield curves generated from different timing gates.

Using the Monte-Carlo simulation program a time-of-flight spectrum was produced for the $\pi^-\pi^0 p$ channel, at a momentum corresponding to the centre of this enhancement (755 Mev/c). Fig.4.6 shows the comparison between the data and the simulation (the spectra have been normalized so as to have the same number of events in each). Clearly there is good agreement between the two shapes: in particular, there is no evident structure in the data (structure would be required if the enhancement in the yield curve was due to meson production, as discussed in section 1.2).

To study the source of this enhancement more fully, yield curves obtained from different timing gates were investigated; the following definitions were used:

$Y(p)$	:	the yield curve of the data, generated from the cms gate;
$PS(p)$	:	the simulated yield curve obtained from the Monte-Carlo for yields in the cms gate, assuming a 3-body phase space distribution for the final state;
$PS_1(p)$	:	the simulated yield curve generated from a different, fixed gate.

If the 3-body final state can be described by a phase space distribution, and if the enhancement is due to a nucleon resonance directly formed in the s-channel, then,

$$Y(p) = BW_s(p).PS(p)$$

and

$$Y_1(p) = BW_s(p).PS_1(p)$$

so that

$$Y_1(p) = Y(p).\frac{PS_1(p)}{PS(p)} \qquad \ldots\ldots\ldots\ldots(4.6)$$

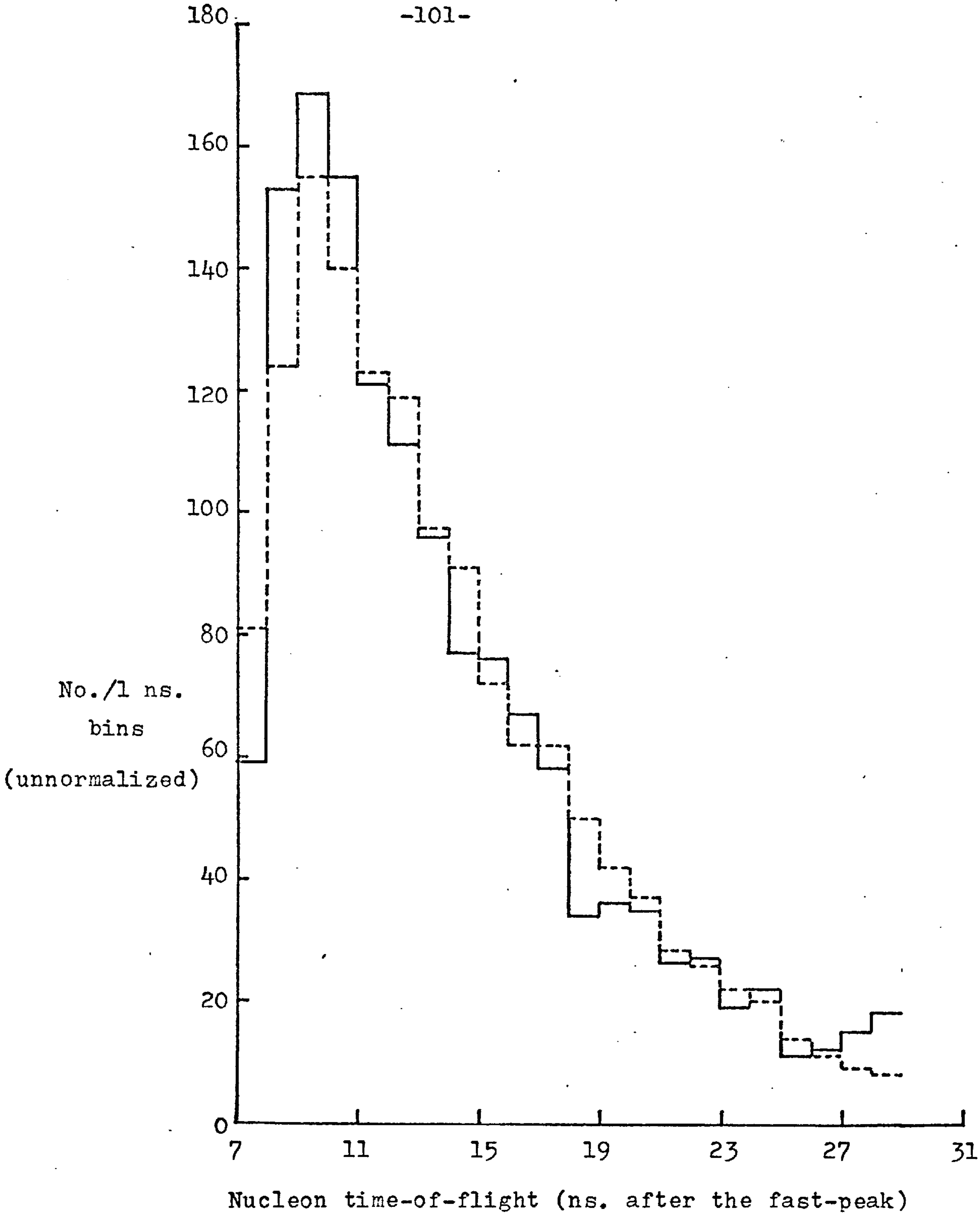

FIG. 4.6

The comparison of the observed (broken line) and predicted (solid line) time-of-flight spectra of the combined classifications (used in analysis) containing events from the $\pi^-\pi^0 p$ final state at 755 Mev/c.

is the yield curve predicted for the data in the new timing gate. For this description to be valid, when this predicted curve is compared with that for the actual data, the two curves should be identical in shape and magnitude.

On the other hand, if the enhancement is due to meson production, the same will not of course be true: in this case, the enhancement will move to a higher momentum in the yield curve generated from the new timing gate, as already discussed in section 4.2. So the curve of equation (4.6), which implies, to first order, that the position of the enhancement is independent of the choice of timing gate, will be inadequate to describe such an effect.

In Fig.4.7 the comparison is shown between the predicted curve of equation (4.6) and that for the actual data, generated from yields in a fixed gate 20 to 26 ns. after the fast-peak.

As the predicted curve provided a reasonable fit to the data, the technique was extended to several other fixed gates - so that most of the available time-of-flight spectrum was utilized: the required movement of the enhancement if its source was meson production would then be clearly observable.

In Fig.4.8 the data is compared with predictions of both meson and nucleon resonance models for a series of fixed timing gates. Thus the arrows indicate where the peak in the yield curves should occur if a meson of mass 580 Mev/c^2 is the cause of that in the yield curve of the cms gate. (A mass of 580 Mev/c^2 is used since this is the value of the missing

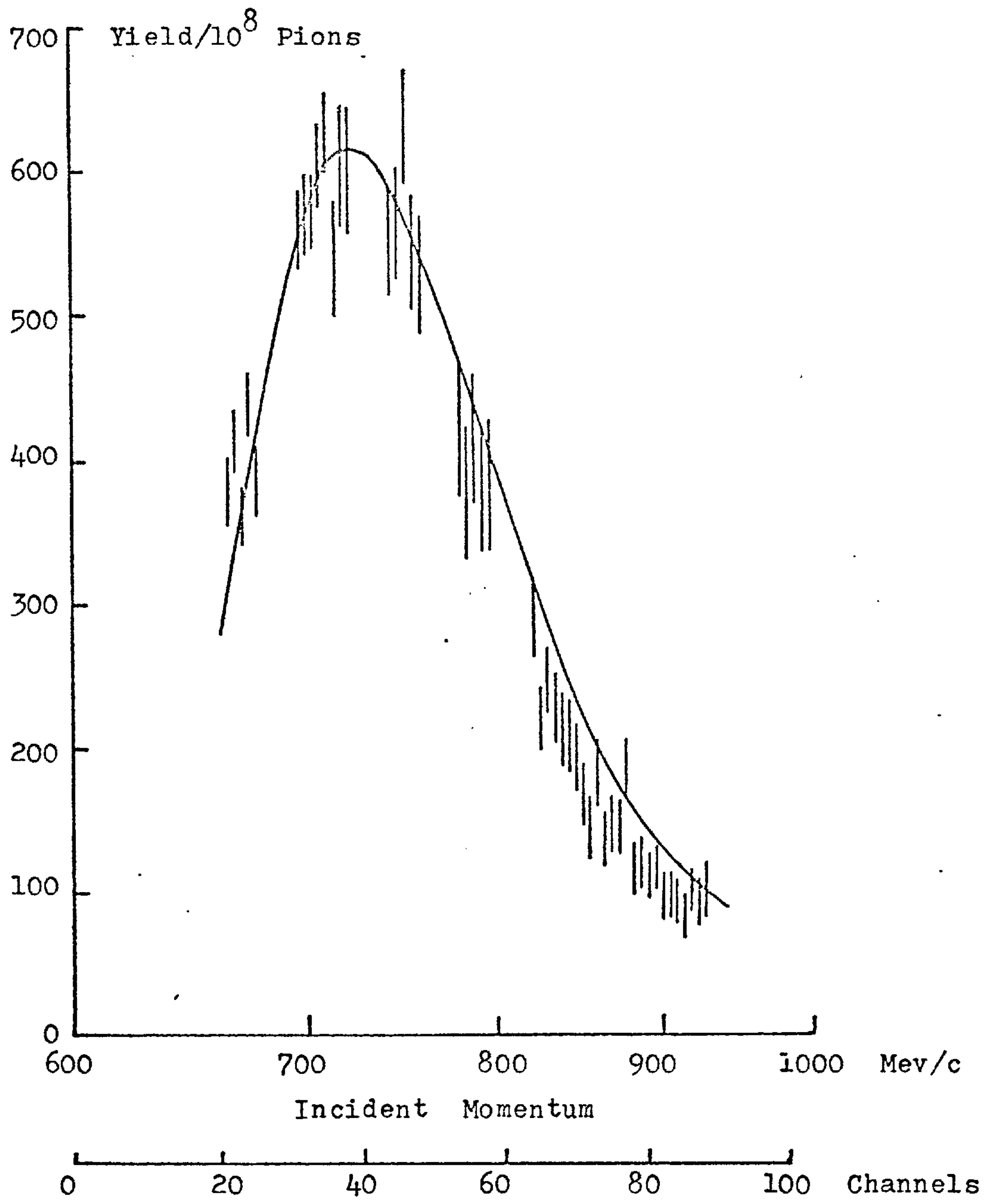

FIG. 4.7

The fit (solid line) to the yield curve generated from the fixed gate 20 to 26 ns. after the fast-peak, predicted by the 'phase space model' from the data in the cms gate.

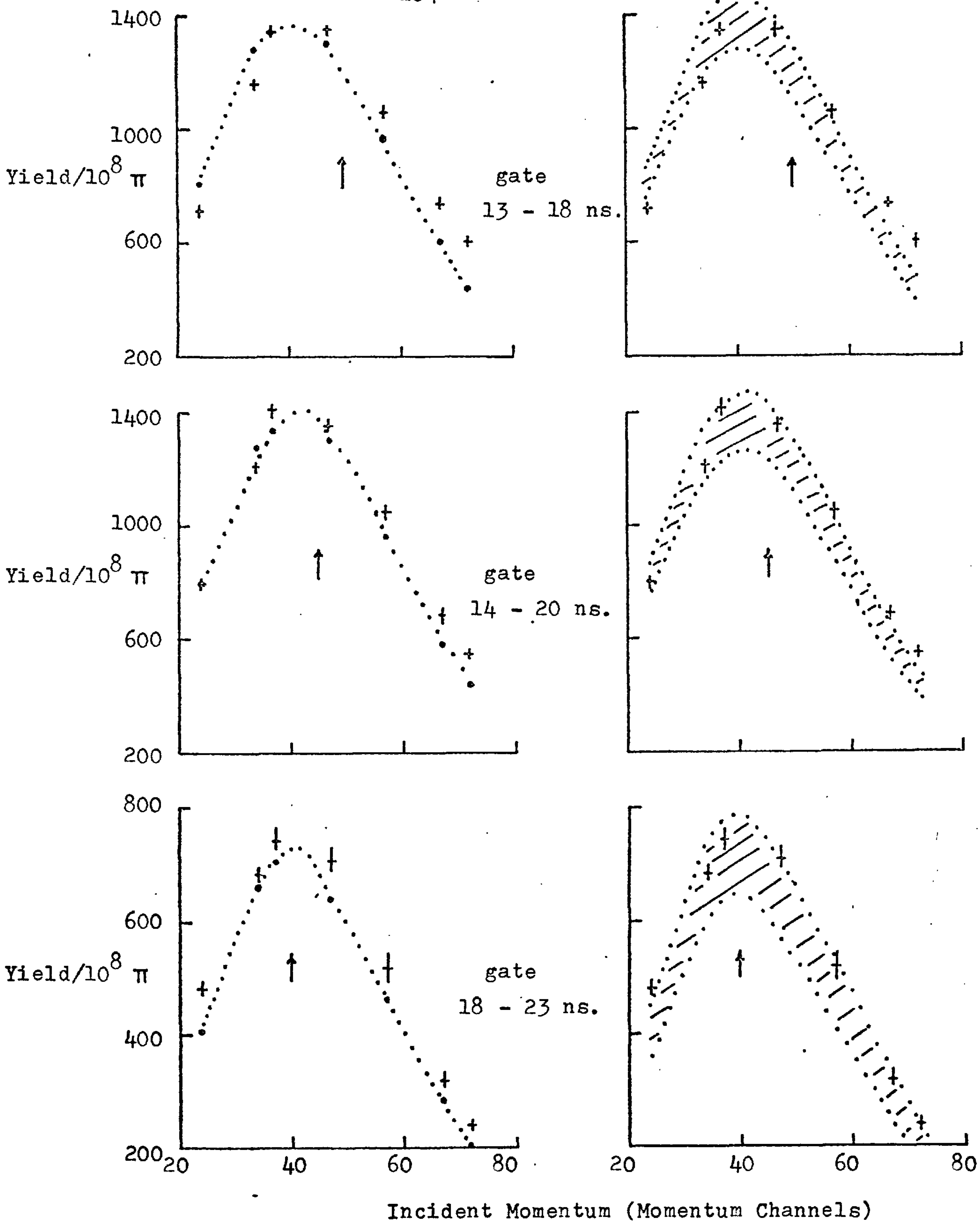

FIG. 4.8

The fits (dotted lines) predicted by the phase space model to the yield curves generated from different timing gates for the $\pi^- \pi^o$ p channel. On the right, the hatched band represents the limits of the predicted values allowing for statistical errors. The arrows indicate the predicted peaks assuming meson resonance production.

mass produced at the centre of the peak generated from the cms gate). The predictions of the nucleon resonance model are also shown: the hatched band represents the limits of the predicted values allowing for the statistical errors in the Monte-Carlo yields.

Clearly, the meson hypothesis does not fit the observed data. Conversely, the predictions based on the nucleon resonance - phase space model furnish extremely reasonable fits - particularly in the absence of any normalizing constants.

4.4.2 Mass and width of the enhancement.

It has been demonstrated above that the structure in the $\pi^-\pi^0p$ channel at a centre-of-mass energy of 1520 Mev. cannot be explained as an effect of meson resonance production. However, the yields from different timing gates do behave in a manner reasonably compatible with their being produced by a final state describable in terms of a phase space model. It is therefore tempting to explain the enhancement on the basis of a single nucleon resonance model (although this was tacitly assumed in the preceding section, the result expressed by equation (4.6) is not changed if the enhancement is due to some combination of s-channel nucleon resonances). This model would assume that the nucleon resonance is formed in the s-channel, and subsequently decays according to a 3-body phase space distribution involving the isotropic production of the recoiling nucleon. The mass and width of such a resonance are the two parameters to be determined.

There are reasons why such a model seems to be a simplification of the true situation:

(1) many partial waves are known to contribute to the total $\pi^-\pi^0 p$ cross-section in this region. For example, Fig.4.9 shows the total inelastic cross-section of five $I = \frac{1}{2}$ waves present here; most of these cross-sections are due to $\pi\pi N$ final states (see section 5.1). The curves were obtained from the results of a typical recent phase shift analysis (18). In particular, two of these waves are resonant in the vicinity of the enhancement seen in the yield curve. These are the D13(1520) and S11(1535), although the latter decays predominantly into ηN final states in its inelastic channel (5); the notation is as before, L2I2J(mass), where L is the orbital, and J the total angular momentum, and I is the isotopic spin;

(2) the transition matrix for the process $\pi + N \rightarrow N^* \rightarrow \pi\pi N$ is unlikely to be entirely describable by a simple phase space model; the D13(1520), for example, is thought to couple strongly to $\Delta(1236)\pi$ final states (19).

Further discussion of these problems will be postponed until chapter five; for the moment, the determination of the best mass and width of the enhancement on the basis of this simple model is pursued.

In affecting such a determination, another problem is the lack of data below 670 Mev/c: no suitable background subtraction from under the peak is therefore feasible - although this is somewhat mitigated by the strength of the signal.

FIG. 4.9

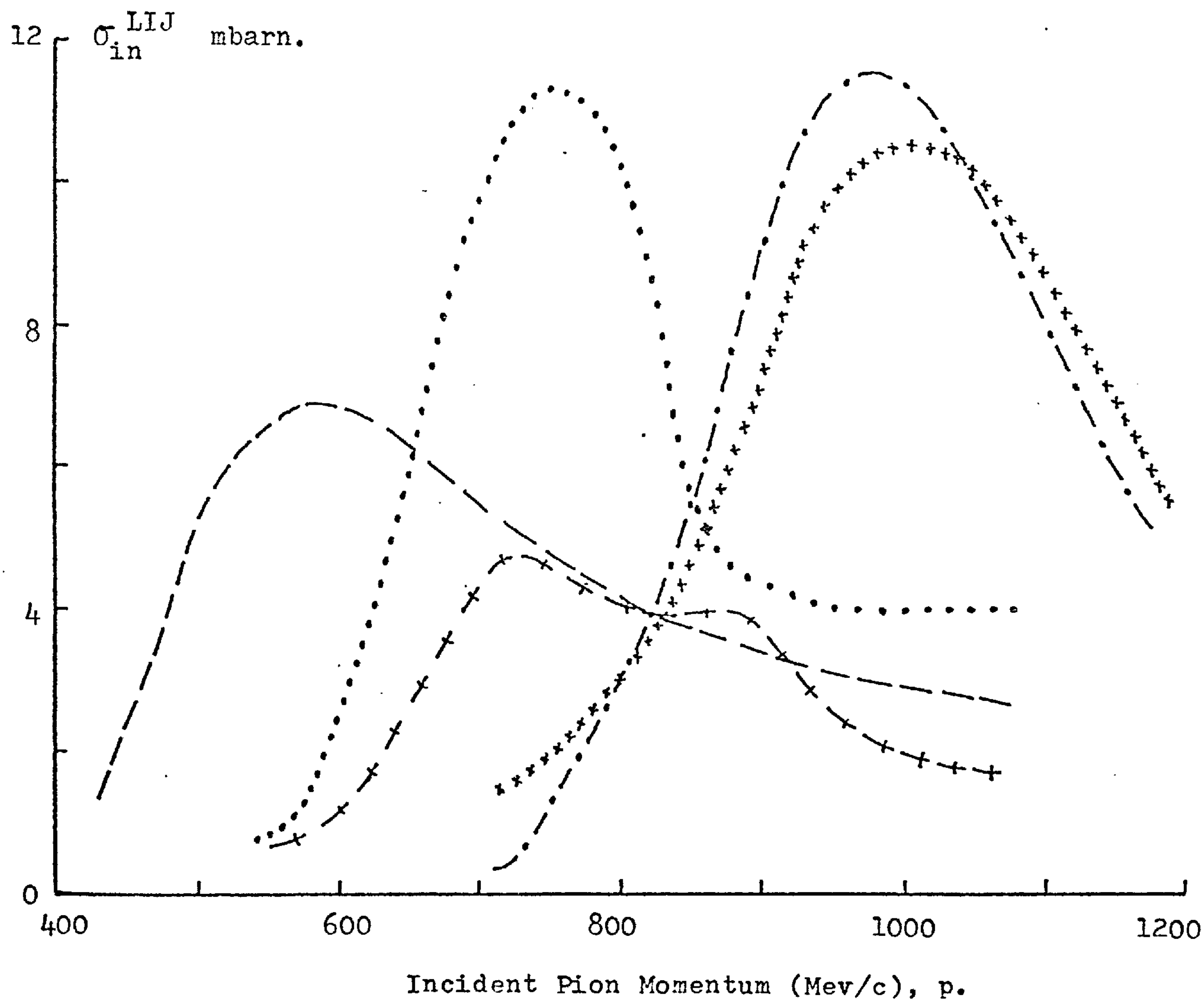

The total inelastic cross-sections of the I = 1/2 partial waves from a recent πN phase shift analysis(18), σ_{in}^{LIJ}, plotted against incident pion momentum, p.

KEY

S11	—+ —+
P11	— — —
D13	• • • • •
D15	—·—·
F15	x x x x

Following the analysis developed in section 4.3, the observed yield curve, $Y(p,t_2-t_1)$, generated from a gate t_2-t_1, using the nucleon resonance - phase space model can be expressed as

$$Y(p,t_2-t_1) \propto BW_s(p).PS(p,t_2-t_1)$$

where $PS(p,t_2-t_1)$ is the simulated 3-body phase space yield curve, and

$$BW_s(p) \propto \frac{A}{A + (E^*(p) - M_s)^2} \quad , \quad A = (\Gamma_s/2)^2$$

where M_s and Γ_s are the mass and width of the nucleon resonance, E^* is the centre-of-mass energy, and p is the incident pion momentum.

From the Monte-Carlo simulation, PS(p) is indeoendent of p for yields in the cms gate (Fig.4.4); so that for the yield curve in this gate

$$Y(p) \propto BW_s(p) \quad \text{only.}$$

The yield curve generated from this cms gate was therefore fitted by tabulated functions of $BW_s(p)$ for various values of M_s and Γ_s to obtain their best values. The fitting was performed using the program MIXFIT (20) which subjected the curve-fitting procedure to a standard χ^2- test while automatically taking care of the normalization. The best fit (Fig.4.10) was obtained for values of M_s = 1535 Mev/c^2 and Γ_s = 105 Mev/c^2. The quality of the fit was, however, extremely poor (giving a confidence level $\leq$ 0.1 %); so then the data was fitted by $BW_s(p)$ plus a straight-line background. This furnished much better fits, the best of which was obtained for M_s = 1520 Mev/c^2: although the fit was less sensitive to variations in the value of Γ_s , for values of M_s = 1520 Mev/c^2 and Γ_s = 120 Mev/c^2 a confidence level of 79 % was obtained (Fig.4.11).

4.4.3 An estimate of the total cross-section corresponding to the enhancement.

The numerical values and definitions used in this section are as follows:

ρ :	density of liquid hydrogen	: 0.071 gm/cm^3
N_o:	Avogadro's number	: 6.02 . 10^{+23} mole^{-1}
A :	atomic wt. of hydrogen	: 1.01
l :	length of hydrogen target	: 29.4 cm.
$\rho . N_o . l/A$		: 1.24 . 10^{24} cm^{-2}

Using the phase space model, and recalling the definitions of section 4.3,

FIG. 4.10

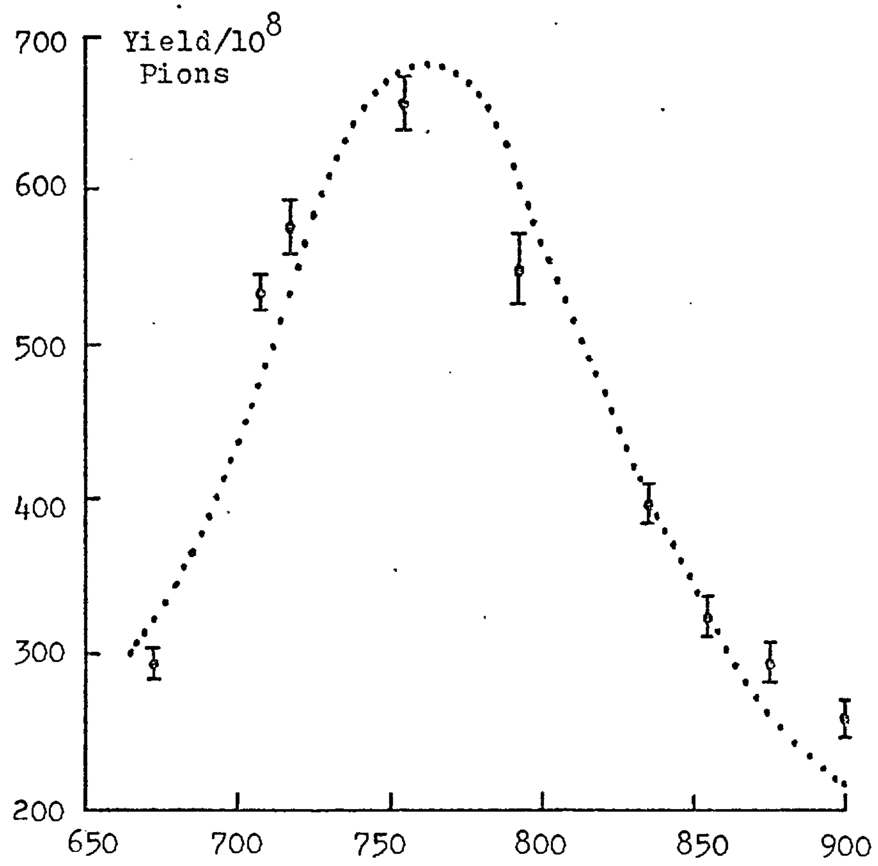

FIG. 4.11

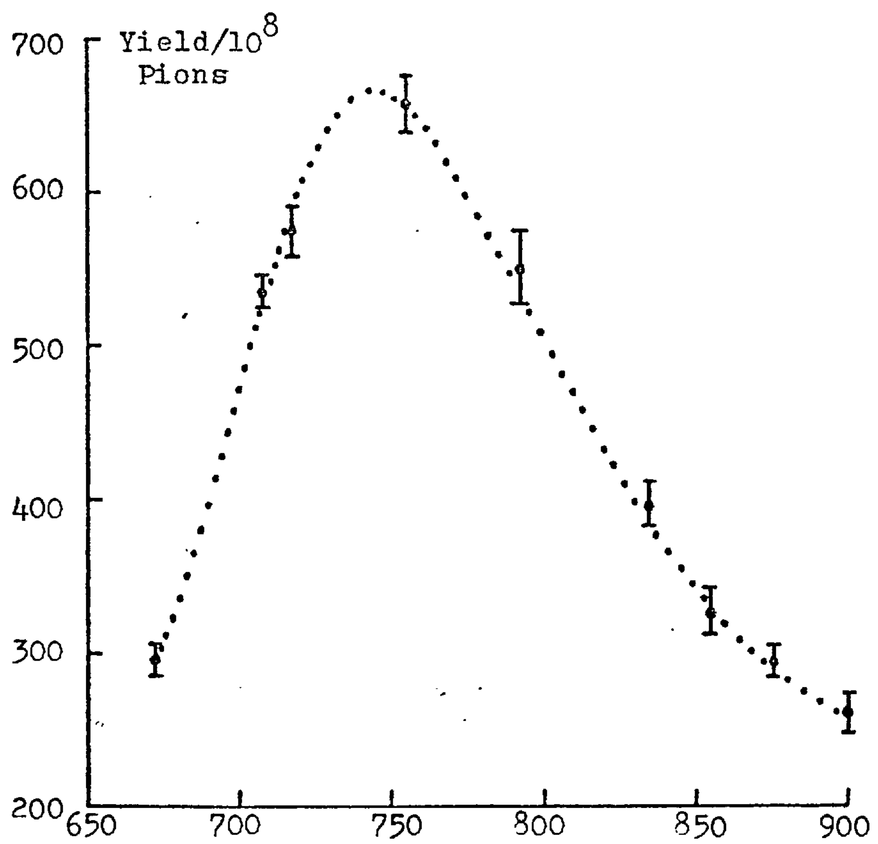

FIG. 4.10 : The best fit to the $\pi^- \pi^0 p$ yield curve by a single Breit-Wigner resonance (Mass 1535, width 105 Mev/c^2).

FIG. 4.11 : The best fit by a straight-line background plus a single Breit-Wigner resonance (Mass 1520 and width 120 Mev/c^2).

PS : the simulated yield of events in the $\pi^-\pi^0 p$ channel for which the nucleon is in the cms gate, per fixed number of incident pion attempts;

PS = $c_1 . c_2 . c_3$

y : the total number of events in the $\pi^-\pi^0 p$ channel detected by the apparatus per 10^8 incident pions;

Y : the number of events in y for which the nucleon is in the cms gate

Y = the yield observed in the cms gate per 10^8 pions.

So,

$Y/y = c_3$, the fraction of all events detected in the cms gate.

The centre-of-mass differential cross-section $d\sigma / d\Omega$ is then given by

$$\frac{d\sigma}{d\Omega} = \frac{y}{c_2} . \frac{1}{\Delta\Omega} . (1.24 . 10^{24})^{-1} \qquad cm^2/st.rad.$$

where c_2 is the efficiency of the array for detecting the two pions, and $\Delta\Omega$ is the solid angle subtended by the neutron counters in the c-system. It follows that

$$\Delta\Omega = 4\pi . c_1$$

where c_1 is the number of events detected by the neutron counters in the phase space simulation, per fixed number of incident pion attempts. So the differential cross-section reduces to:

$$\frac{d\sigma}{d\Omega} = \frac{Y}{4\pi . c_1 . c_2 . c_3} \quad . \quad (1.24 \; . \; 10^{24}\;)^{-1}\; cm^2/st.rad.$$

$$= \frac{Y}{4\pi . PS} \quad . \quad (1.24 \; . \; 10^{24}\;)^{-1}\; cm^2/st.rad.$$

This is the expression which links the differential cross-section to the observed yield Y in the cms gate. To obtain an estimate of the total cross-section, isotropy is assumed, so that

$$\sigma = 4\pi \; . \; \frac{d\sigma}{d\Omega} = (Y/PS) \; . \; (1.24 \; . \; 10^{24}\;)^{-1}\; cm^2$$

At the centre of the peak at an incident momentum of 755 Mev/c, $Y = 658 \pm 19$ from the data, and $PS = 164.9 \pm 12.8$ from the Monte-Carlo, for 100 million and 200,000 pions respectively. A better estimate for PS can be obtained by recalling that PS is independent of p (Fig.4.4), so that it is reasonable to take an average of the values from the Monte-Carlo outputs. Then $PS = 175.4 \pm 8.5$, per 200,000 pions. Inserting these values in the expression for the total cross-section gives $\sigma = 6.1 \pm 0.3$ mbarn. Remembering from section 3.4.1 that an estimated 4 ± 1 % of the total observed rate is due to non-$\pi^-\pi^0 p$ events, a corrected value for the total cross-section, assuming isotropy, of the reaction $\pi^- + p \rightarrow \pi^-\pi^0 p$ at an incident momentum of 755 Mev/c is obtained:

$$\sigma = 5.8 \pm 0.3 \text{ mbarn.}$$

Values of the total cross-section for this reaction at momenta close to 755 Mev/c have previously been determined (directly in bubble chamber experiments where the recoiling proton is detected at all angles in the c-system). These are:

$$\sigma = 4.98 \pm 0.54 \text{ mbarn. at } 735 \text{ Mev/c} \quad (21),$$

and $$\sigma = 5.37 \pm 0.25 \text{ mbarn. at } 761 \text{ Mev/c} \quad (22).$$

Above 755 Mev/c there is obviously disagreement between the shapes of the total cross-section (Fig.1.5) and the yield curve (Fig.4.1) for this channel: the total cross-section remains fairly constant, whereas the yield curve decreases rapidly.

From these observations, it is possible to draw two conclusions. Thus at around 755 Mev/c, a phase space model involving the isotropic production of the proton in the c-system provides a reasonable estimate of the total cross-section: at higher momenta, a non-isotropic differential cross-section is required to explain the difference in shape between the total cross-section and the yield curve, and in particular, the emergence of the enhancement seen in the latter.

Another important quantity is the ratio of the total cross-sections for the reactions $\pi^- + p \rightarrow \pi^+\pi^- n$ and $\pi^-\pi^o p$:

$$R = \frac{\sigma(\pi^+\pi^-)}{\sigma(\pi^-\pi^o)} .$$

From the data of this experiment the quantity dR can be extracted, where,

$$dR = 4.\frac{Y(\pi^+\pi^-).f_2(\pi^-\pi^o)}{Y(\pi^-\pi^o).f_2(\pi^+\pi^-)} .$$

Here Y is the observed yield in the cms gate, and f_2 is the detection efficiency of the dipion for nucleons in this gate. A factor of 4 is included to compensate for the difference in detection efficiency of the neutron counters for protons (100 %) and neutrons (25 %). If the phase space model is valid, then at each incident momentum the value of dR should be the same as R. Thus Fig.4.12 shows the plot of dR against incident momentum, together with values of R obtained from an early compilation (23), and recent experiments (22,24). As can be seen, at around 755 Mev/c the values of dR are the same as those of R: at higher momenta, dR becomes larger than R. To try to see what this implies, it should be remembered that for nucleons detected in the cms gate, the effective mass of the dipion is almost its maximum value (this is true at each incident momentum). So if $dR > R$, it can be inferred that there might be some mechanism which preferentially produces the $\pi^+\pi^-$ system with high masses; or alternatively, there might be

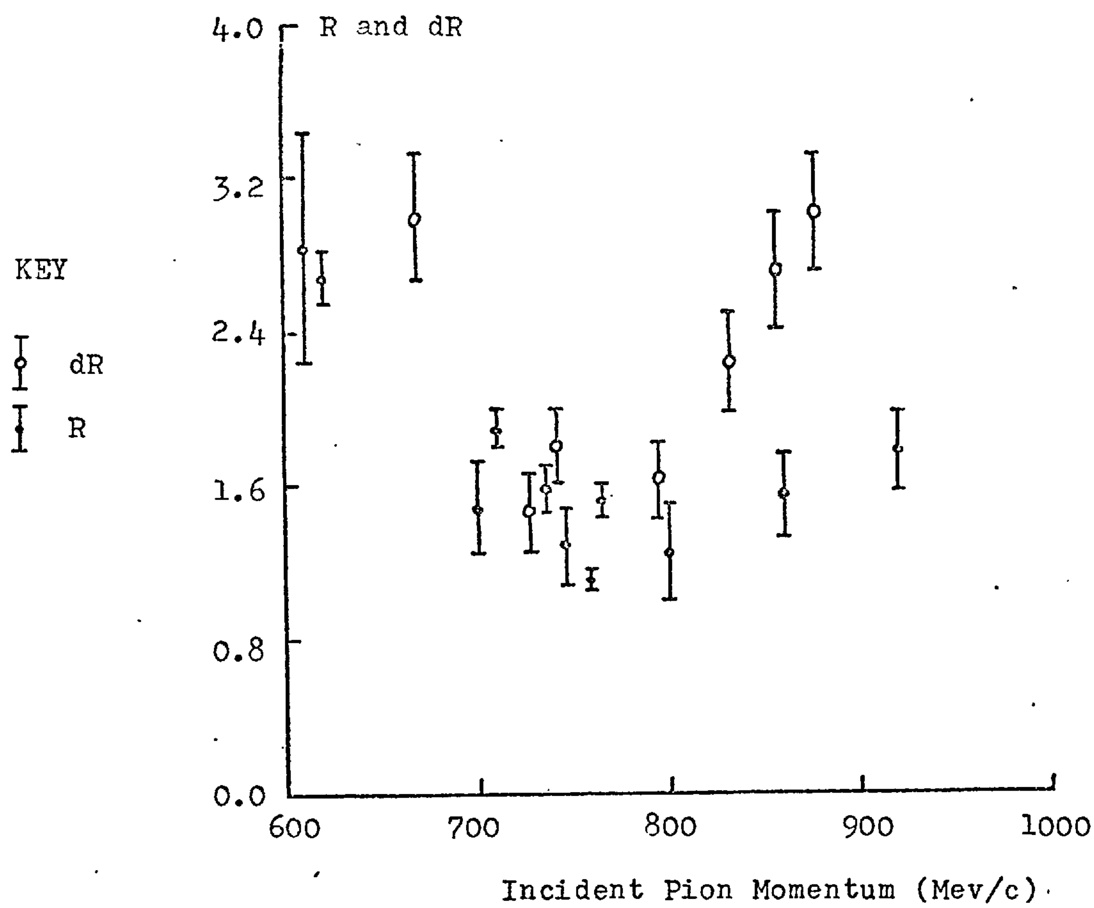

FIG. 4.12

Plots of R and dR against incident pion momentum. The values of R come from references (22,23,24); those of dR come from this experiment.

a mechanism which prevents $\pi^-\pi^0 p$ production with high dipion masses; or a combination of both these effects may be present. Further discussion of these possibilities follows in chapter five.

4.5 The Analysis of the Enhancement in the $\pi^-\pi^0 p$ Channel at a Centre-of-Mass Energy of 1710 Mev.

The yield curves generated from the cms gate for both the 5 and 6 mt. data (Figs.4.1 and 4.2) show a narrow enhancement at an incident momentum of approximately 1070 Mev/c (corresponding to a centre-of-mass energy of about 1710 Mev. and a missing mass of 765 Mev/c^2). The 6 mt. data was chosen for the detailed study of this effect, since it provided both better statistics and mass resolution, coupled with a greatly reduced level of "casual" events (see section 2.5).

4.5.1 Evaluation of the best mass and width of the enhancement.

In analysing this effect, the enhancement was seen to move to different momenta in the yield curves generated from different timing gates (Fig.4.15). As a result, the numerical integration program (section 4.2) was used to simulate the yield curves predicted for meson resonances of varying masses and widths; these were then fitted to that obtained from the data, to establish best mass and width values of the enhancement. The yield curve from the cms gate, where there is the best mass resolution, was used; the statistics of the data in this gate (Fig.4.13A) merited the use of the yields in individual momentum channels for these evaluations.

The first problem was to remove the background under the signal. This was achieved by fitting low-order polynomials to the data points to the left and right of the enhancement (Fig.4.13B). Polynomials of increasing degree were successively tried, using a Least Squares fitting technique (25), until one was found such that increasing its order did not improve the quality of the fit significantly. Fig.4.13B shows the data and the polynomial of degee 3 which satisfied this condition. Subtracting this curve from the observed data over the region of the enhancement left the signal whose mass and width were the parameters to be determined (Fig.4.13C).

Tabulated functions corresponding to the predicted yield curves of meson resonances with varying masses and widths were then generated by the numerical integration program. Each of these was fitted to the data using the program MIXFIT (20). Kinematics curves were used to provide approximate mass and width values about which these parameters were chosen to vary. Fig.4.13C shows the best fit obtained in this way: this gave a mass of 765 Mev/c^2 and a width of 35 Mev/c^2, with a Confidence Level of 93 % (there were 21 degees of freedom). As an indication of the errors involved in the fitting procedure, Fig.4.14 shows typical curves of the Confidence Level obtained for various values of the resonance parameters.

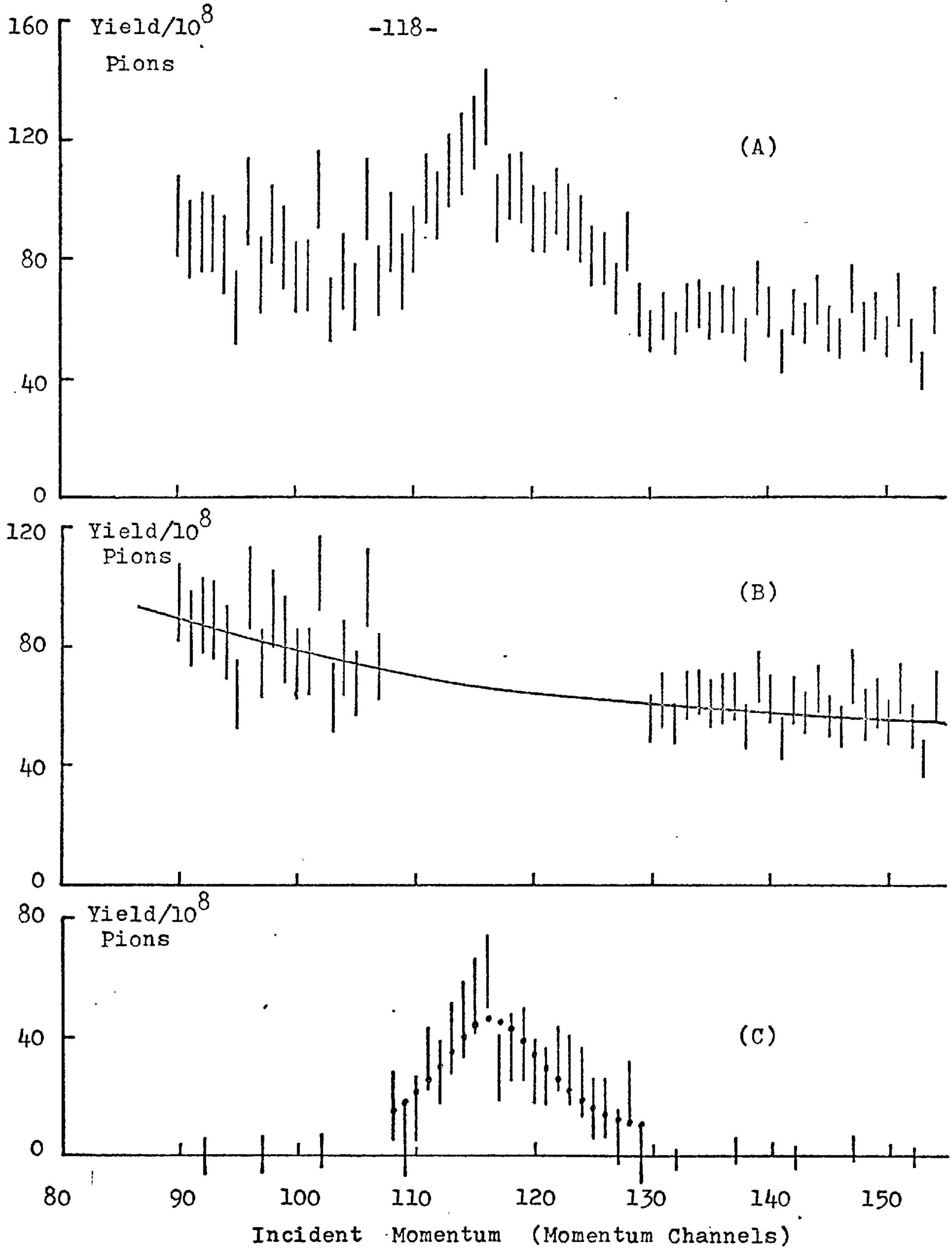

FIG. 4.13: (A) is the yield curve generated from the cms gate for the $\pi^- \pi^0$ p channel (for yields in individual channels);
(B) shows the fit (solid line) to the background;
(C) shows the fit (dotted line) to the enhancement, after background subtraction, by a single Breit-Wigner resonance.

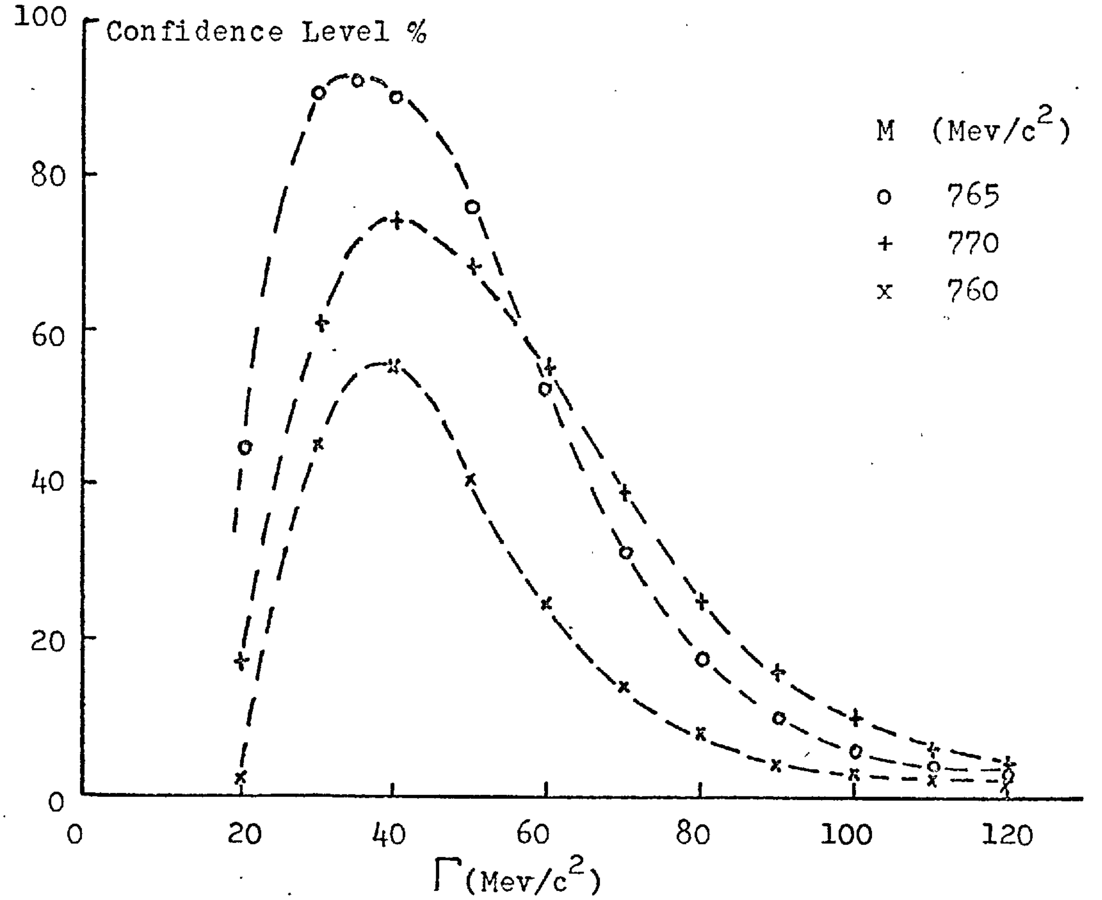

FIG. 4.14

The quality of the fits to the enhancement in the yield curve of the $\pi^-\pi^0 p$ final state by a single Breit-Wigner (meson) resonance; various masses, M, and widths, Γ, are tried for the resonance.

4.5.2 The position of the enhancement in yield curves generated from different timing gates.

As noted above, the position of the enhancement, in yield curves obtained from different timing gates, was seen to move (Fig.4.15). To establish if such movements were consistent with the production of a meson resonance of mass 765 Mev/c^2, a study of these curves was made.

In fact the choice of timing gates suitable for the generation of yield curves is limited by practical difficulties: as a result, the observable movement of the position of the enhancement will similarly be restricted.

In this momentum range the time-of-flight t_c, corresponding to the centre-of-mass velocity, is fairly long (at 1070 Mev/c it is 18 ns. after the fast-peak). Now the recoiling protons lose energy in ionising collisions in the hydrogen of the target before being detected at the neutron counters. For slow protons with times-of-flight $t > t_c$ this results in a relatively large systematic timing error in the recorded value. Thus for a proton produced at the centre of the target and having a recorded time-of-flight of 30 ns. after the fast-peak, a correction of 5 ns. would be required: for one produced at the upstream end of the target (traversing some 30 cm. of hydrogen), the correction would be 7 ns.[1e] In the 5 mt. data, where no attempt was made to define the point of interaction, this would result in a worsening of the mass resolution if such protons were used for the missing mass

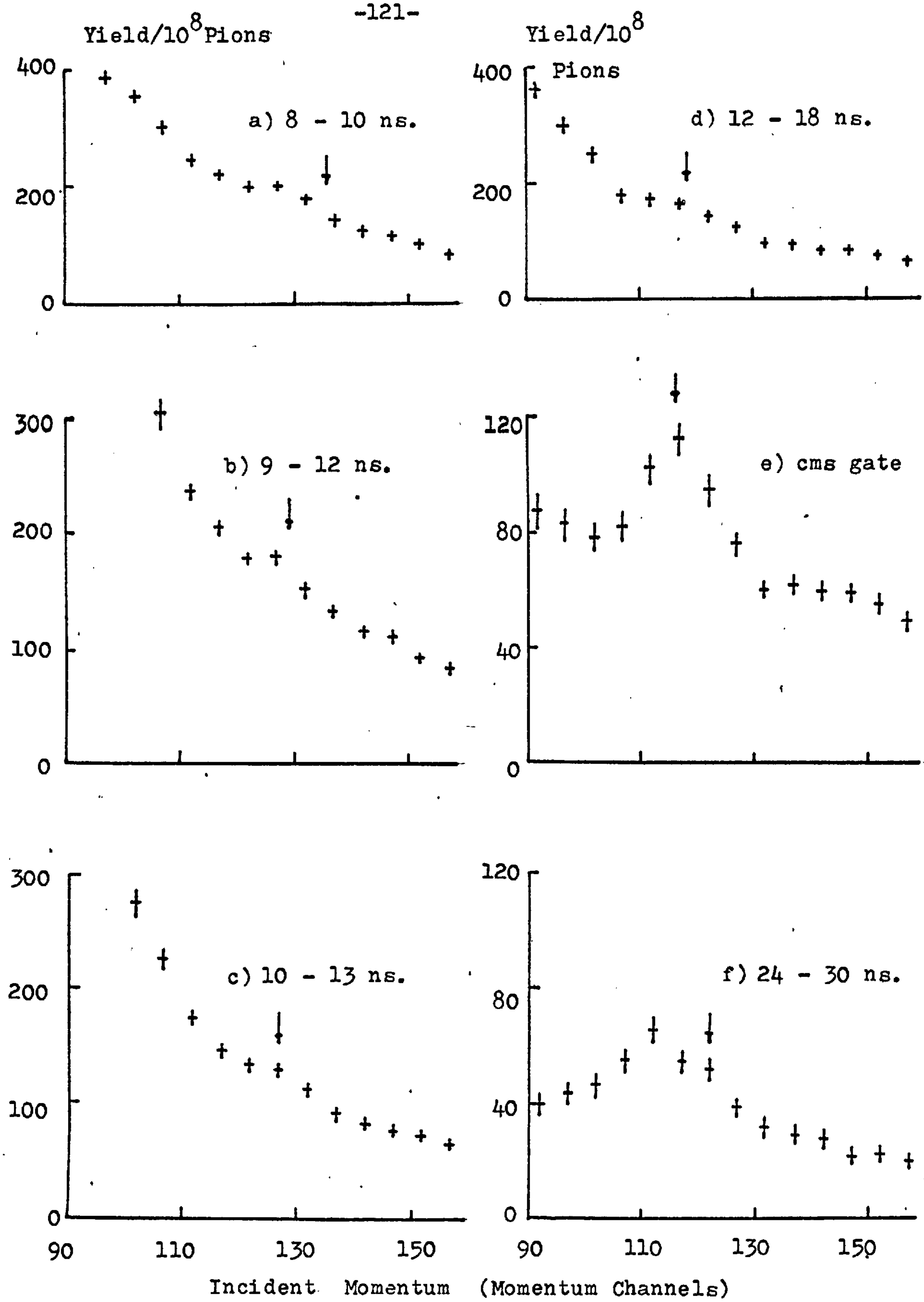

FIG. 4.15

The yield curves of the $\pi^-\pi^0 p$ final state generated from different timing gates; the arrows indicate the predicted positions of a meson resonance of mass 765 Mev/c^2; the fixed gates are all measured relative to the fast-peak; at the centre of the peak e) the cms gate limits are 16 - 21 ns.

determination. For the 6 mt. data, the target counters (section 2.4.1) furnished a more precise definition of the interaction vertex, and the analysis program made a corresponding correction to the raw time-of-flight (le). In the program the proton was assumed to have traversed a particular length of hydrogen depending on which of these counters had been triggered by the charged pion in the final state. In fact these values were specifically designed for studies of the reaction $\pi^- + p \rightarrow A_2^- + p$, $A_2^- \rightarrow \pi^-$ + neutrals, mainly $\pi^-\pi^0\pi^0$ (lb), but were also adequate for the $\pi^-\pi^0 p$ final state. When the correction was made to proton times-of-flight 30 ns. after the fast-peak, the timing error introduced was reduced by almost an order of magnitude compared with that for the 5 mt. data. It was thus of the same order as the uncertainty introduced by the electronic timing resolution, and would no longer seriously affect the mass resolution.

For times-of-flight greater than 30 ns., the required correction for the loss of energy in ionising collisions in the hydrogen becomes increasingly large and non-linear. It is consequently much less reliable. So it was decided that times-of-flight of 30 ns. after the fast-peak represented the limit of reliable measurement for protons.

The meson simulation program was used to predict the momentum at which the enhancement due to a resonance of mass 765 Mev/c^2 would occur in a yield curve generated from a gate 24 to 30 ns. after the fast-peak. It was found that it would move only 6 momentum channels relative to its position in the curve generated from the cms gate. This shift in momentum would be difficult to detect with the available statistics.

On the fast side of t_c, for times-of-flight $t < t_c$, the mass resolution becomes increasingly worse as $\partial M/\partial t$ rises rapidly (Fig.1.3). In this region it is dominated by the term $\partial M/\partial t . dt$, where dt is the intrinsic electronic timing resolution ($\pm$ 0.6 ns.). For a gate 8 to 10 ns. after the fast-peak, for instance, this leads to an uncertainty of about $\pm$ 14 Mev/c^2 (standard deviation) in a missing mass determination of 765 Mev/c^2. This should be compared with the value of $\leq \pm 3$ Mev/c^2 obtainable in the determination from yields in the cms gate (section 1.4.2). At the lower momenta in the data set, for times-of-flight less than 8 ns. the nucleons are reaching the limit available from 4-momentum conservation.

In this analysis, a variety of gates in the range from 8 to 30 ns. after the fast-peak was used. The numerical integration program predicted the momenta at which a meson of mass 765 Mev/c^2 would be expected to occur in yield curves generated from these gates. (A Breit-Wigner form with a width of 35 Mev/c^2 was used to obtain these predictions; following the discussion of section 4.2, the results are independent of the choice of width.)

Thus in Fig.4.15 the predictions are denoted by the arrows. As can be seen, in some of the yield curves, the predicted position of the meson does not exactly coincide with the centre of the observed enhancement. So the problem remained to assign mass values to these enhancements. To do this, hand-drawn backgrounds were constructed by using data points to the left and right of the observed structures, the momenta, p_o, corresponding to the centres of which were then judged by eye. Next the simulation program was used to predict the momenta at which a series of mesons with masses $\simeq$ 765 Mev/c^2 would occur in the same yield curves (generated from timing gates which will be denoted by t_o): by interpolation, the mass values $M_o = M(p_o, t_o)$ corresponding to each central momentum p_o were established.

Possible systematic variations of M_o with p^* (the c-system momentum of the nucleon) and $-T$ (the 4-momentum transfer) can then be investigated. Each timing gate represents a range of values of p^* and T : formally, $p^* = p^*(p, t_o)$ and $T = T(t_o)$, where p is the incident pion momentum. To fix values of these parameters, those calculated at the centres of the gates were chosen: $p^* = p^*(p, \overline{t}_o)$ and $T = T(\overline{t}_o)$. Table 4.1 shows the values of $p^*(p_o, \overline{t}_o)$ and $T(\overline{t}_o)$ together with the corresponding missing masses $M_o(p_o, t_o)$. The same information is shown graphically in Fig.4.16. (The errors involved were calculated as follows: for the fastest gates, where the mass resolution is worst, the error in the mass determination is taken as the value of $\partial M/\partial t.dt$, where dt is 0.6 ns.; for the other gates, the error represents the uncertainty in the determination of the central momentum p_o - nominally taken as two momentum channels.) From the curves it appears that there is neither a systematic variation of M_o with p^* nor with T.

TABLE 4.1

The missing masses $M_o = M(p_o, t_o)$ corresponding to the centres of the enhancements seen at momenta p_o in the yield curves generated from a series of timing gates t_o (Fig.4.15). The corresponding parameters p^* (the c-system momentum) and $-T$ (the 4-momentum transfer) are also shown.

Timing gate t_o ns. after the fast-peak.	Missing Mass M_o Mev/c^2.	C-system momentum p^* Mev/c.	4-momentum transfer $-T$ $(\text{Gev/c})^2$.
cms	$765 {}^{+5}_{-5}$	28	0.315
8 - 10	$744 {}^{+12}_{-9}$	245	0.688
9 - 12	$765 {}^{+7}_{-7}$	175	0.586
10 - 13	$771 {}^{+8}_{-7}$	140	0.532
12 - 18	$770 {}^{+6}_{-5}$	65	0.396
24 - 30	$748 {}^{+5}_{-4}$	132	0.191

In particular, if the observed enhancements are due to the production of a meson resonance with a mass which is independent of p^*, then the plot of M_o against p^* should obviously be of the form M_o = constant.

The alternative hypothesis of nucleon resonance formation can also be tested. It is assumed that the enhancement seen in the yield curve generated from the cms gate (Fig.4.2) is due to a nucleon resonance. The enhancement occurs at an incident momentum of $p = p_s$ = 1070 Mev/c. Following the discussion of section 4.3, enhancements should, to first order, occur at the same momentum in yield curves generated from the timing gates t_o. At the momentum $p = p_s$, each timing gate t_o represents a range of $p^* = p^*(p_s,t_o)$, and there will be corresponding missing masses $M_s = M(p_s,t_o)$. So Fig.4.16 also shows the plot of $M(p_s{=}1070,t_o)$ against $p^* = p^*(p_s,\bar{t}_o)$. Now if the nucleon resonance hypothesis is valid, $M(p_o,t_o) = M(p_s,t_o)$ and $p^*(p_o,\bar{t}_o) = p^*(p_s,\bar{t}_o)$ for all the gates t_o.

Inspecting Fig.4.16 it is clear that this condition is only satisfied for one value of t_o, whereas there is only one value of t_o for which the result $M_o(p^*)$ = constant is inconsistent. The weight of evidence therefore supports the conclusion that the enhancement seen in the yield curve at 1070 Mev/c is due to meson resonance production.

FIG. 4.16

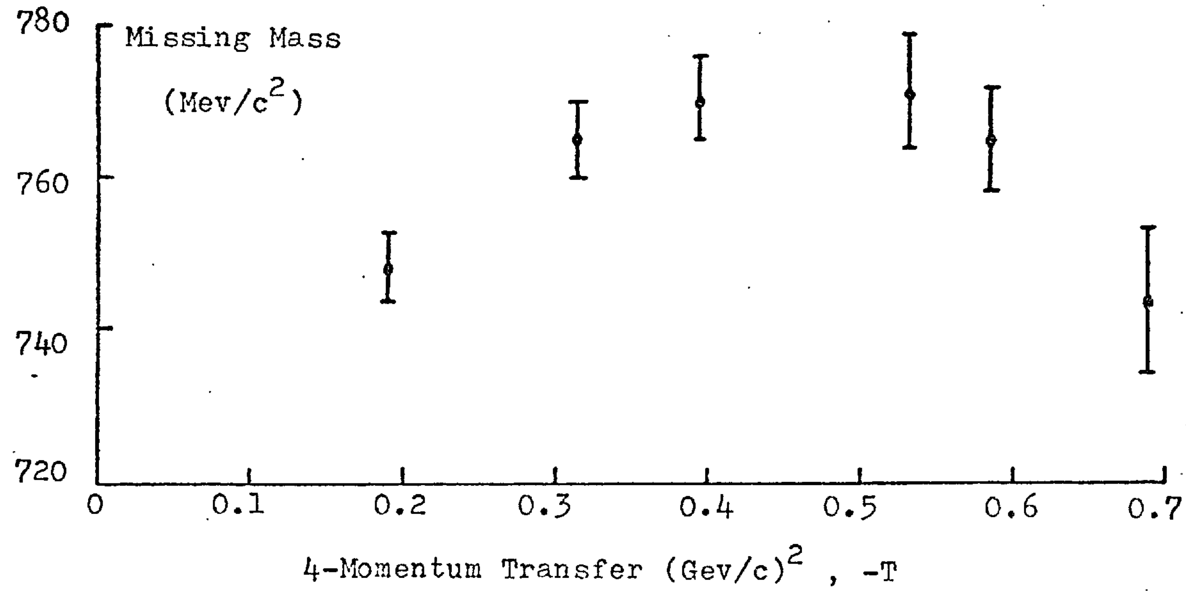

The missing mass against 4-momentum transfer.

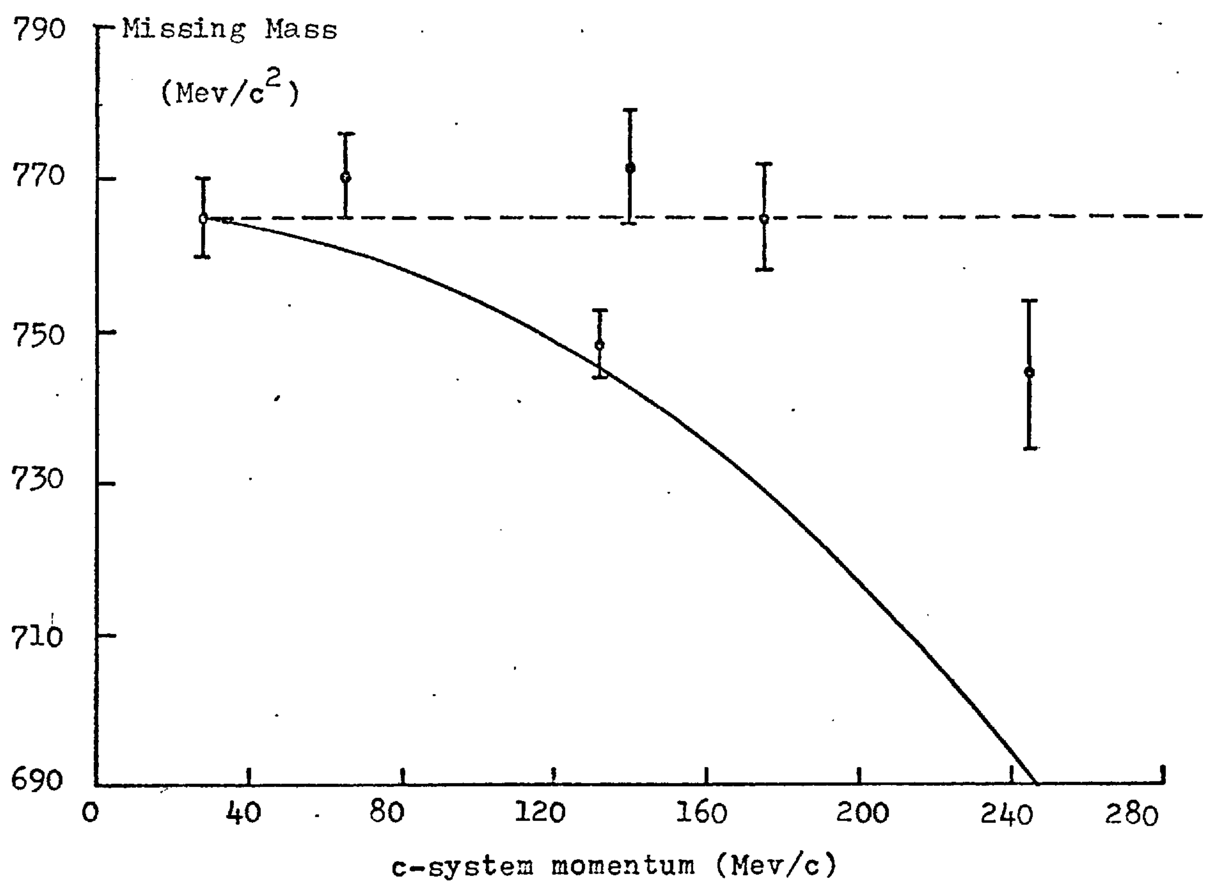

The missing mass as a function of c-system momentum. The solid line indicates the curve required for nucleon resonance formation; the broken line indicates that for production of a meson resonance of mass 765 Mev/c^2.

Chapter Five

The Interpretation and Discussion of Results.

5.1 The Region Below 1 Gev/c.

Most of the present knowledge of the various $N^*(I = 1/2)$ and $\Delta(I = 3/2)$ resonances comes from sophisticated phase shift analyses of data obtained from πN scattering experiments, in which the resonances are directly formed in the s-channel.

From the formalism developed for such an analysis, the inelastic cross-section σ_{in}^{LIJ} of a partial wave (L2I2J) is given by (26)

$$\sigma_{in}^{LIJ} = (\pi / k^2) . (J + 1/2) . (1 - \eta_{LIJ}^2)$$

where L = the orbital angular momentum;

J = the total angular momentum;

I = the isotopic spin;

$\hbar k$ = the centre-of-mass momentum;

and η_{LIJ} = the elasticity parameter (26) of the partial wave (L2I2J), derivable from the analysis.

The total inelastic cross-section σ_{in}^{I} of all the partial waves with isotopic spin I, and present at a given momentum, is then just the sum of such individual contributions σ_{in}^{LIJ} over values of L (L = 0 to L_{max}) and J ($J = L \pm \frac{1}{2}$ for πN

scattering):

$$\sigma^{I}_{in} = (\pi / k^2) \cdot \sum_{\substack{L = 0 \\ J = L \pm \frac{1}{2}}}^{L_{max}} (J + 1/2) \cdot (1 - \eta^{2}_{LIJ})$$

..............(5.1)

Below an incident pion momentum of 1 Gev/c, many experiments have shown that the cross-sections for producing more than two pions in the final state, and those for the associated production of strange particles, are very small (5); the predominant inelastic channel is to $\pi\pi N$ final states, although the S11 partial wave is a notable exception, decaying preferentially to ηN states (27).

Suppose, then, that the inelastic contributions of the five isotopic spin 1/2 waves known to be important in this region (see Fig.4.9 - the S11, P11, D13, D15 and F15 waves) are combined using equation (5.1).

To accomplish this, a particular set of solutions of η as a function of incident pion momentum must be selected from the various different analyses available (9). Because the difficulties inherent in such analyses are legion, the results are to some extent subjective (4); thus the exact shape of a plot of $\sigma^{I = \frac{1}{2}}_{in}$ against momentum will depend on which particular set of solutions of η is chosen. However, the values of the analysis by KIRSOPP (18) have been chosen quite arbitrarily for this calculation, since the conclusions drawn from it, deduced below, are not particularly sensitive to this choice.

Now the inelastic cross-section for π^-p scattering is given by

$$\sigma_{in}(\pi^- p) \;=\; (2/3)\,.\,\sigma^{I\,=\,1/2}_{in} \;+\; (1/3)\,.\,\sigma^{I\,=\,3/2}_{in} \quad .$$

So by inserting a factor of 2/3 into the summation of equation (5.1) for the five partial waves of interest, the cross-section for the reaction

$$\pi^- + p \xrightarrow{I\,=\,1/2} (S11 + P11 + D13 + D15 + F15) \xrightarrow{\quad} \begin{matrix}\text{essentially}\\ \pi\pi N \text{ states}\end{matrix}$$

can be obtained as a function of incident momentum (where 85 % of the S11 contribution is removed to allow for its ηN decay (5)).

This curve can then be directly compared with that for the sum of the experimentally measured cross-sections for the single pion production channels available in π^-p scattering:

$$\sigma_{in}\,(\pi^- + p \longrightarrow \pi^0\pi^0 n \;+\; \pi^+\pi^- n \;+\; \pi^-\pi^0 p\,).$$

The comparison is shown in Fig.5.1, where the sum of the experimentally measured cross-sections is obtained by the addition of three fits by eye to each of the cross-sections shown in Fig.1.5; the nominal errors shown in Fig.5.1 assume errors of $\pm$ 0.5 mbarn. on each fit at each momentum. It is clear that, for $\pi^- p$ scattering at these incident momenta, the five I = 1/2 partial waves largely account for the total single pion production cross-section. It therefore seems reasonable that any interpretation of the gross features of the yield curves must be in terms of these waves (at least in a first approximation). This result was indeed anticipated in section 4.4.1, where it was seen that the very large enhancement (equivalent to a total cross-section of $\simeq$ 6 mbarn.) observed in the $\pi^-\pi^0 p$ yield curve was produced by purely s-channel effects, and not by meson production.

Recently, partial wave analyses have been extended to the study of the 3-body $\pi\pi N$ final state produced by πN scattering (22,24,28,29,30). In order to extract the maximum amount of information from the data, specific assumptions concerning the structure of the 3-body final state must be made. To this end, the phenomenological "isobar model" has been developed (31). The model assumes that the most important amplitudes for single pion production processes are those in which a pair of particles (called an "isobar") interact in the final state. Thus the total amplitude is represented by the coherent addition of individual amplitudes for reactions of the form

$$\pi + N \rightarrow \pi + \Delta \quad , \Delta \rightarrow \pi + N$$
$$\pi + N \rightarrow \rho + N \quad , \rho \rightarrow \pi + \pi$$

FIG. 5.1

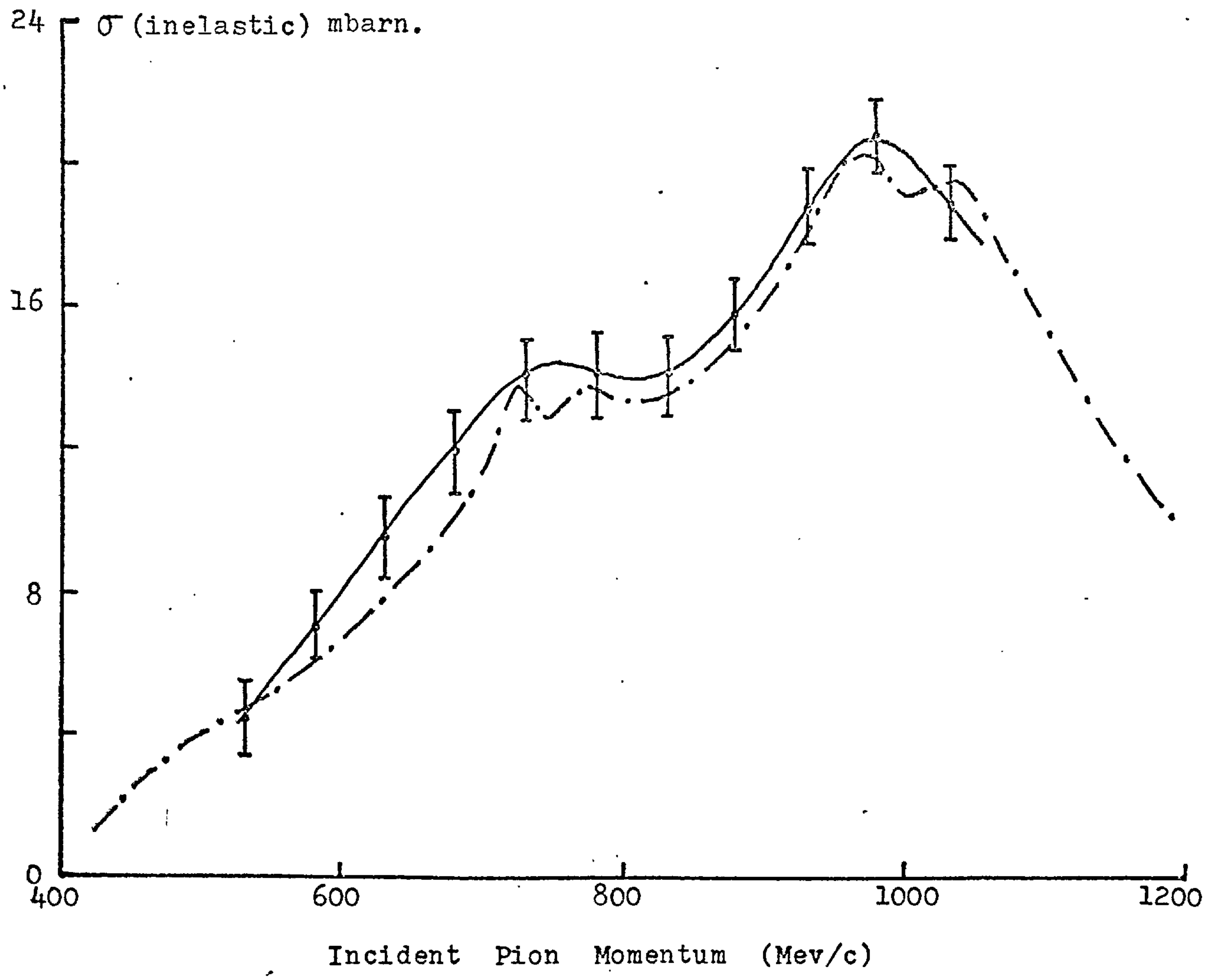

The sum of the cross-sections for the three single pion production channels in π^- p scattering (solid line); this curve is compared with the sum of the total inelastic cross-sections for the five I = 1/2 partial waves, the S11 ($\pi\eta$ contribution excluded), P11, D13, D15 and F15, in π^- p scattering (broken line).

Diagramatically,

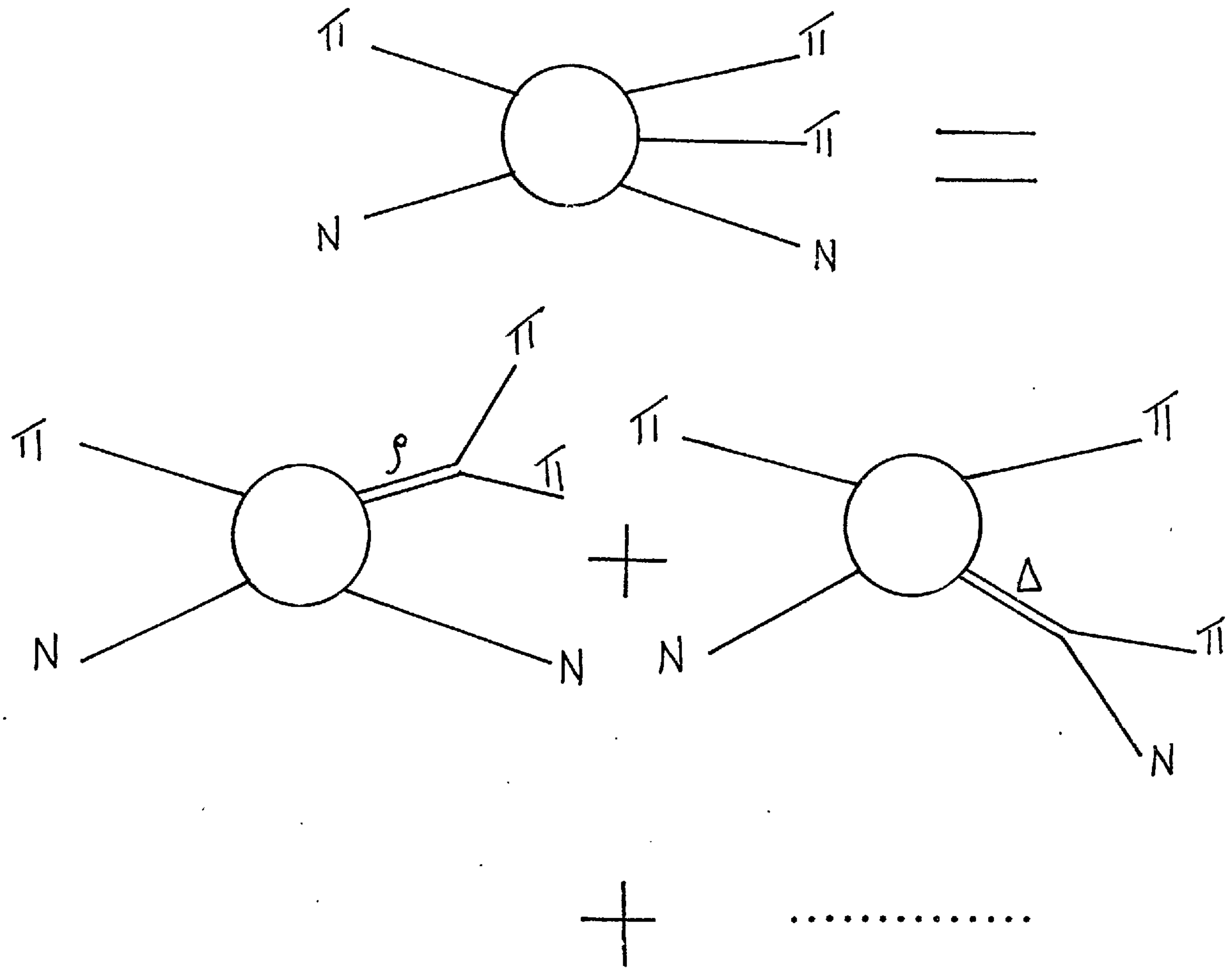

For the production of each quasi two body system, a large number of partial waves are included in the model (represented by the 'bubbles' in the above diagram). Finally, Bose symmetry is ensured for the two pions.

For π^-p interactions, the following "isobars" are typically included in the total amplitude:

isobar	decay mode	I	J^P
$\Delta(1236)$	πN	3/2	$3/2^+$
σ (?)	$\pi\pi$	0	0^+
$\rho(765)$	$\pi\pi$	1	1^-

The production amplitude would then have the form

$$T = T(\pi\Delta) + T(\sigma N) + T(\rho N).$$

Generally, five parameters are necessary to describe a 3-body final state. These are normally taken to be

i) $s^{\frac{1}{2}} = E^*$, the invariant mass of the system;

ii) $\cos\theta$ and ϕ, where θ and ϕ are the polar and azimuthal angles which relate the direction of the incident pion beam to that of the normal to the plane containing the 3 final-state particles (in the overall c-system);

iii) M_{12} and M_{23}, the invariant masses of particles 1 and 2, and of 2 and 3 respectively, which specify the relative positions of the 3 particles in the plane.

The differential cross-section (following SAXON[32]) can then be written as

$$\frac{d^4\sigma}{dM_{12}^2 dM_{23}^2 d\cos\theta d\phi} \propto \sum_{M,M_s} |T|^2$$

where M and M_s are the initial and final nucleon spin states.

As a specific example, the production of the $\Delta(1236)$ isobar is considered (the D13 resonance of mass 1520 Mev/c^2 is thought to couple strongly to $\Delta\pi$ states):

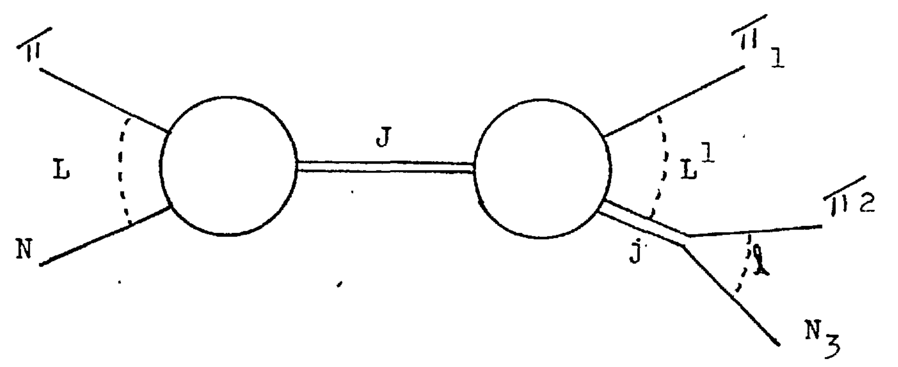

Here,

L = the orbital angular momentum of the initial state;

L^1 = the orbital angular momentum of the (quasi two body) final state;

and J = the total angular momentum.

Also,

j = the spin of the Δ = 3/2;

and ℓ = the relative orbital angular momentum of the $\pi_2 N_3$ system = 1.

The model assumes that the transition amplitude can be expressed as the product of two factors; the first represents the production amplitude, and the second the decay amplitude of the Δ resonance. The transition amplitude from an initial spin state M to a final state M_s is then finally given by (32)

$$T(\pi\Delta) \propto \sum_{J,L,L^1} T^{JLL^1}(s^{\frac{1}{2}}, M_{23}) \cdot f^{JLL^1}_{M\,M_s}(M^2_{12}, M^2_{23}, \theta, \emptyset)$$

where,

$f^{JLL^1}_{M\,M_s}$ is a complex quantity (32) representing the decomposition of the transition into spherical harmonics;

and,

$$T^{JLL^1} = A^{JLL^1}(s^{\frac{1}{2}}) \cdot \frac{1}{(M_{23} - M_\Delta) + i\Gamma_\Delta/2}$$

where A^{JLL^1} are complex amplitudes representing the relative weights of the partial waves $(L, L^1, 2J)$, and M_Δ and Γ_Δ are the mass and width of the Δ resonance.

A special case arises if only one wave $q = (L, L^1, 2J)$ is dominant at a particular value of s. If this wave couples strongly to the $\pi\Delta$ state, then,

$$d^4\sigma \quad \propto \quad \sum_{M,M_s} \left| T^q \, . \, f^q_{M,M_s}(M_{12}, M_{23}, \theta, \phi) \right|^2$$

$$\propto \quad \left| T^q \right|^2 \, . \, \sum_{M,M_s} \left| f^q_{M,M_s} \right|^2$$

Integrating over the solid angle gives the representation of the density of states in the Dalitz plot:

$$\frac{d^2\sigma}{dM_{12}{}^2 dM_{23}{}^2} \quad \propto' \int_\Omega \left| T^q \right|^2 . \sum_{M,M_s} \left| f^q_{M,M_s} \right|^2 \; d\cos\theta . d\phi$$

$$\propto \quad \left| T^q \right|^2 . \quad F(M_{12}{}^2, M_{23}{}^2) \quad \ldots\ldots\ldots\ldots (5.2)$$

where,

$$F = \int_\Omega \sum_{M,M_s} \left| f^q_{M,M_s} \right|^2 . \; d\cos\theta . d\phi$$

To make further progress, the model must now be related to the data from this experiment. To accomplish this, the kinematics of the reaction $\pi + N \longrightarrow \pi_1 + \pi_2 + N_3$ peculiar to this experiment are considered.

If the detected nucleon has a time-of-flight within the cms gate, then it must be produced very close to rest in the c-system; this is true at each incident pion momentum, p . If $s^{\frac{1}{2}}(p) = E^*(p)$ is the invariant mass of the system, the effective mass of the dipion, M_{12}, is known uniquely:

$$M_{12} = E^* - m_N = M_{12max} = m_{12} \text{ (say)},$$

where m_N is the mass of the nucleon. In other words, as mentioned earlier in section 1.3, the kinematic region of the cms gate is equivalent to that at the tip of the Dalitz plot with $M_{12}{}^2$ as ordinate.

Moreover, if the nucleon is produced at rest in the c-system, the energies E^*_π and momenta $\underline{p}^*_\pi$ of the two pions are equal. Now as before it is assumed that the final state is produced via the quasi two body $\pi\Delta$ state. So if the Δ is constrained to decay into a stationary nucleon and a pion of energy E^*_π , the invariant mass M_{23} is given by

$$M_{23}{}^2 = (E^*_\pi + m_N \, , \, \underline{p}^*_\pi)^2$$

$$= m_\pi{}^2 + m_N{}^2 + 2E^*_\pi m_N \qquad \ldots\ldots\ldots\ldots(5.3)$$

The invariant mass $s^{\frac{1}{2}} = E^*$ of the system is given by

$$E^*(p) \quad = \quad 2E^*_{\pi} \quad + \quad m_N \qquad \ldots\ldots\ldots\ldots\ldots\ldots(5.4)$$

So that at each incident momentum p , corresponding to a fixed value of $E^*(p)$, equations (5.3) and (5.4) show that there exist unique values of the invariant mass $M_{23} = m_{23}$ (say).

Now the yield in the cms gate is directly related to the integral over the density of states (equation 5.2) at the tip of the Dalitz plot:

$$\begin{matrix}\text{yield in} \\ \text{cms gate}\end{matrix} \quad \propto \quad \iint\limits_{\substack{\text{cms gate} \\ \text{limits}}} \left| T^q(s^{\frac{1}{2}}, M_{23}) \right|^2 . \; F(M_{12}{}^2, M_{23}{}^2).dM_{12}{}^2 .dM_{23}{}^2$$

$$\ldots\ldots\ldots\ldots\ldots\ldots\ldots\ldots(5.5)$$

assuming that only one partial wave q is important at s. In an exact analysis this integral would need to be evaluated, but at present this has not been attempted. However, recalling that over the region of integration $M_{12} \simeq m_{12}$ and $M_{23} \simeq m_{23}$, in an obvious simplification,

$$\begin{matrix}\text{yield in} \\ \text{cms gate}\end{matrix} \quad \approx \quad \left| T^q(s^{\frac{1}{2}}, m_{23}) \right|^2 . \; F(m_{12}{}^2, m_{23}{}^2) \iint dM_{12}{}^2 .dM_{23}{}^2$$

$$\ldots\ldots\ldots\ldots\ldots\ldots\ldots(5.6)$$

where,

$$\left| T^q(s^{\frac{1}{2}}, m_{23}) \right|^2 = \left| A^q(s^{\frac{1}{2}}) \cdot \frac{1}{(m_{23} - M_\Delta) + i\Gamma_\Delta/2} \right|^2$$

$$= \left| A^q(s^{\frac{1}{2}}) \right|^2 \cdot BW_\Delta(m_{23})$$

If the function $F(m_{12}^2, m_{23}^2) \cdot \iint dM_{12}^2 dM_{23}^2$ in equation (5.6) is a smooth, well-behaved function of the incident pion momentum, p , then the shape of the yield curve $Y(p, t_{cms})$ generated from yields in the cms gate will be governed by the product of the terms

$$\left| A^q(s^{\frac{1}{2}}) \right|^2 \cdot BW_\Delta(m_{23}).$$

Further, if the partial wave $q = (L, L^1, 2J)$ is resonant (at a mass $E^*(p) = M_s$, and with a width Γ_s), then an appropriate choice for its amplitude squared $\left| A^q(s^{\frac{1}{2}}) \right|^2$ as a function of incident momentum p will be

$$\left| A^q(s^{\frac{1}{2}}(p)) \right|^2 \propto \frac{1}{(E^*(p) - M_s)^2 + (\Gamma_s/ 2)^2}$$

$$\propto BW_s(p)$$

where $s^{\frac{1}{2}}(p) = E^*(p).$

So finally the form of the yield curve $Y(p,t_{cms})$ is given by

$$Y(p,t_{cms}) \approx BW_s(p) \,.\, BW_\Delta(\, m_{23}(p)\,) \qquad \ldots\ldots\ldots\ldots\ldots\ldots(5.7)$$

(Digressing for a moment to suppose that the amplitude A^q of the partial wave q were independent of incident momentum, p . The yield curve predicted by this analysis would peak at $m_{23} = M_\Delta$ - that is at the peak of $BW_\Delta(m_{23})$. Now from πN scattering at low energies it is known that this happens (for a nucleon at rest) when the pion has a kinetic energy of about 200 Mev. Using equation (5.4) with $E^*_\pi = 340$ Mev, it is seen that such a peak would occur at a centre-of-mass energy $E^* = 1620$ Mev. Thus the observed peak in the $\pi^-\pi^0p$ yield curve, at a momentum of 755 Mev/c (corresponding to a value of $E^* = 1520$ Mev), cannot simply be interpreted as a kinematic reflexion of $\Delta(1236)$ production associated with an extra pion.)

How equation (5.7) works in practice is illustrated in Fig.5.2. Here the term $BW_s(p)$ is generated using the mass and width parameters of the D13(1520) resonance - namely, $M_s = 1520$ and $\Gamma_s = 120$ Mev/c^2 (5). The curve is compared with the observed data, normalizing at the data point at 755 Mev/c, and with the predicted yield curve $Y(p,t_{cms})$ assuming the interaction $\pi^- + p \rightarrow \pi^-\pi^0p$ proceeds via $\pi\Delta$ states. For the latter, the mass and width of the $\Delta(1236)$ were taken from the

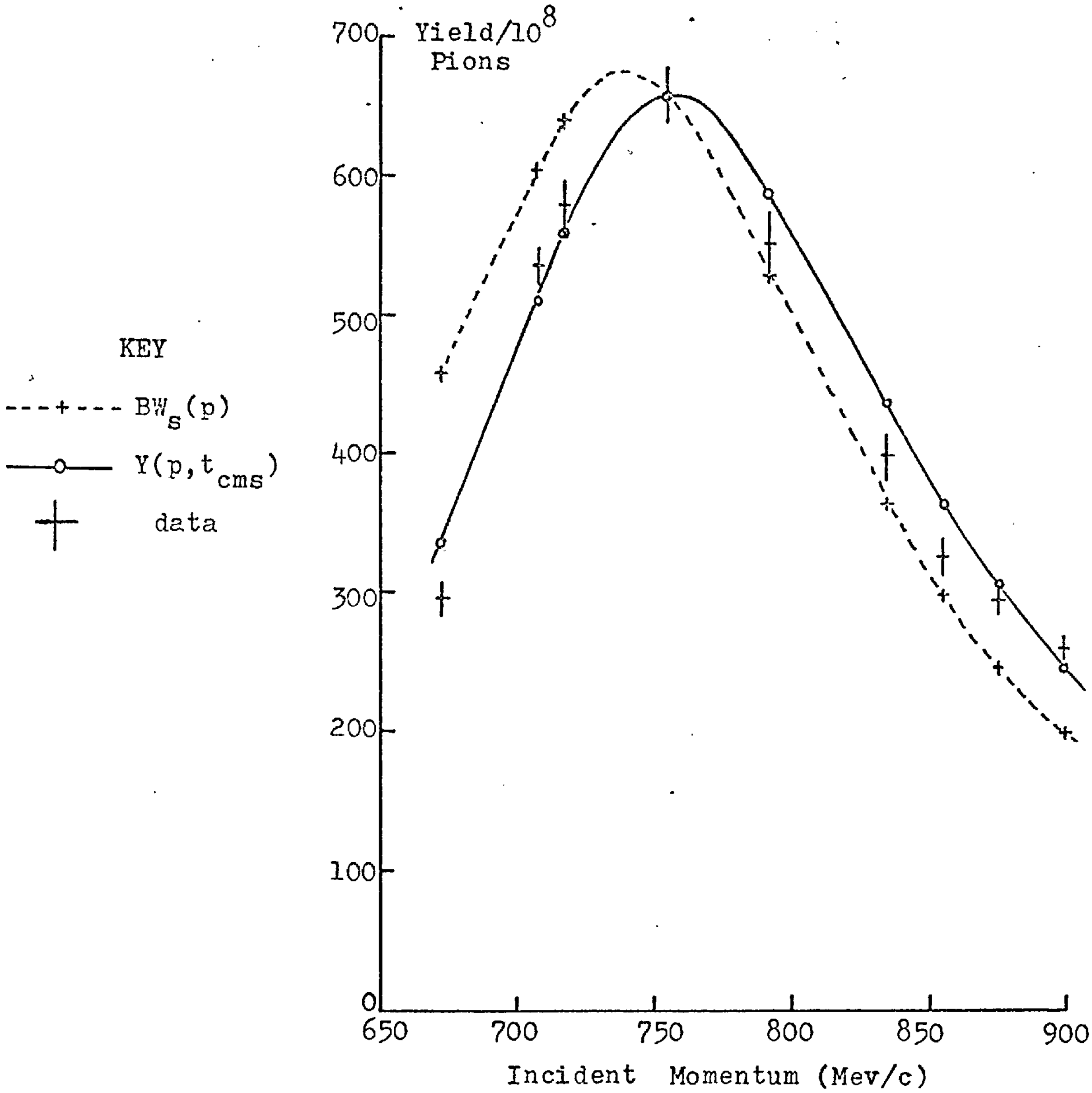

FIG. 5.2

Fit to the $\pi^-\pi^o$ p yield curve generated from the cms gate; by (i) a single Breit-Wigner resonance, $BW_s(p)$, of mass 1520 and width 120 Mev/c^2; and by (ii) the function $Y(p,t_{cms}) = BW_s(p).BW_\Delta(\ m_{23}(p)\ )$.

current listings (5). Obviously including the factor $BW_{\Delta}(m_{23})$ has shifted the original curve $BW_s(p)$ to higher momenta and introduced a slight asymmetry. This is the same sort of effect as seen in the data, although the predicted curve has 'over-compensated' at higher momenta. Nevertheless, the fit to the observed data provided by the curve $Y(p, t_{cms})$ compares very favourably with that for the best fit obtained for a single Breit-Wigner resonance (Fig.4.10).

Recapitulating, it has been shown that a single, resonant, inelastic partial wave q , decaying via a $\pi\Delta$ state into $\pi^-\pi^0 p$, could be expected to produce the same sort of effect as actually observed in the yield curve. But in reality many partial waves are expected to be present at these incident momenta. So it seems reasonable to see if there exists evidence from a more generalized form of the isobar model which could account for the general features of the yield curves in terms of these waves. In particular, the emergence of the large enhancement at $E^* = 1520$ Mev (at an incident momentum of 755 Mev/c) in the proton channel (with no equivalent in the total cross-section), and the differences in the shapes of the yield curves of the neutron and proton channels, must be explained.

In a full treatment of the reaction $\pi^+ + p \rightarrow \pi^+\pi^0 p$ via $\pi\Delta$ quasi two body states, DELER and VALLADAS (33) have calculated the theoretical density of states in the Dalitz plot at two incident momenta in the range discussed here. The calculations were done for each partial wave up to incident orbital angular momentum of L = 3 (up to F waves). Using an amplitude which allows for the effects of interference between the two possible Δ states, they have related the reactions

$$\pi^+ + p \longrightarrow \pi^+ + \Delta^+ \quad \hookrightarrow \pi^0 + p$$

and

$$\pi^+ + p \longrightarrow \pi^0 + \Delta^{++} \quad \hookrightarrow \pi^+ + p$$

by the appropriate product of I-spin Clebsch-Gordan coefficients c_1 and c_2 . Thus for each partial wave $q = (L, L^1, 2J)$

$$\left\langle \pi^+ \pi^0 \; p \;\middle|\; T^q \;\middle|\; \pi^+ \; p \right\rangle = c_1 . T^q(\Delta^+ \pi^+) + c_2 . T^q(\Delta^{++} \pi^0)$$

and the density of states is of the form

$$d^2\sigma \quad \propto \int_{\Omega} \left| \left\langle \pi^+ \pi^0 p \;\middle|\; T^q \;\middle|\; \pi^+ \; p \right\rangle \right|^2 .d\cos\theta \,.\, d\phi \qquad \text{.........(5.8)}$$

The effect of the interference between the two channels $(p\pi^+)\pi^0$ and $(p\pi^0)\pi^+$ is very marked at the tip of the Dalitz plot - that is, in just that region to which this experiment is sensitive, at $M_{12} = m_{12}$ and $M_{23} = m_{23}$. For example, for partial waves with total angular momentum J = 1/2, the quasi two body final state is produced in either a P or a D wave (L^1 = 1 or 2), and the Δ decays with an angular distribution of 1 + 3cosθ. Now the effective mass of the dipion is such that $M_{12}^2 \propto \cos\theta$ (32), so that the projection of the Dalitz plot on the M_{12}^2 axis is peaked at high and low masses. For the SD1 wave (notation $LL^1 2J$) the effect of the interference between the two 'Δ-bands' on the Dalitz plot is to enhance the peaking at high dipion masses; but for the PP1 wave the reverse is true, and in fact the tip of the Dalitz plot is completely depopulated. Other striking examples are provided by the DS3 and DD3 waves. For both of these the interference produces a strong enhancement at high dipion masses, where none exists without the interference. For the FP5 wave, on the other hand, production at high dipion masses is strongly suppressed; the same is true, to a lesser degree, for the DD5 wave.

The isotopic spin Clebsch-Gordan coefficients c_1 and c_2 (Table 5.1) show that for the reaction $\pi^+ + p \rightarrow \pi^+\pi^0 p$ and the I = 1/2 component of $\pi^- + p \rightarrow \pi^-\pi^0 p$, the sign of the product $c_1.c_2$ governing the interference term is the same, although, for the latter, the magnitude is smaller. Hence the same pattern of behaviour for the partial waves producing the $\pi^-\pi^0 p$ channel could be expected to occur. Conversely, Table 5.1 shows that for the reaction $\pi^- + p \rightarrow \pi^+\pi^- n$ the sign of $c_1.c_2$ for the I = 1/2 component is reversed; this implies that destructive effects on the Dalitz plot will become constructive, and vice-versa.

Now by relating the I = 1/2 inelastic partial waves ($LL^1 2J$) to the five I = 1/2 elastic partial waves (L2I2J), important in this momentum region, there is an obvious correspondence:

inelastic	elastic	incident pion momentum Mev/c
SD1	S11(1535)	760
PP1	P11(1470)	660
DP3) DD3	D13(1520)	740
DD5	D15(1670)	1000
FP5	F15(1690)	1030

A pattern emerges that can be tentatively used to explain the general features of the observed yield curves (Fig.4.1).

Thus the inelastic partial waves SD1, DP3 and DD3 all have differential cross-sections which enhance the production of high ($\pi^-\pi^0$) masses in the momentum range discussed here. Their amplitudes A^q would be expected to resonate at centre-of-mass energies equal to the masses of their corresponding elastic partial waves, the S11(1535) and the D13(1520). If there were no other waves present, this effect would produce structure in the $\pi^-\pi^0 p$ yield curve at incident momenta $\approx$ 755 Mev/c, as in fact observed. But there are other inelastic waves present - namely the DD5 and the FP5; and for these, the amplitudes A^q could be expected to resonate at the slightly higher energies equal to the masses of their corresponding resonant elastic partial waves, the D15(1670) and the F15(1690). However, for these inelastic waves the differential cross-sections

TABLE 5.1

The Isotopic Spin Clebsch - Gordan Coefficients.

	$I = 1/2$	$I = 3/2$
$\pi^+ + p \rightarrow \pi^+ + \Delta^+$		
$\quad \hookrightarrow \pi^0 + p$	0	$-\frac{2}{\sqrt{15}}$
$\rightarrow \pi^0 + \Delta^{++}$		
$\quad \hookrightarrow \pi^+ + p$	0	$\sqrt{\frac{3}{5}}$
$\pi^- + p \rightarrow \pi^- + \Delta^+$		
$\quad \hookrightarrow \pi^0 + p$	$-\frac{1}{3}\sqrt{\frac{2}{3}}$	$\frac{4}{3\sqrt{15}}$
$\rightarrow \pi^0 + \Delta^0$		
$\quad \hookrightarrow \pi^- + p$	$\frac{1}{3}\sqrt{\frac{2}{3}}$	$-\frac{1}{3\sqrt{15}}$
$\rightarrow \pi^- + \Delta^+$		
$\quad \hookrightarrow \pi^+ + n$	$-\frac{1}{3\sqrt{3}}$	$\frac{2}{3}\sqrt{\frac{2}{15}}$
$\rightarrow \pi^+ + \Delta^-$		
$\quad \hookrightarrow \pi^- + n$	$-\sqrt{\frac{1}{3}}$	$-\sqrt{\frac{2}{15}}$

suppress the production of high ($\pi^-\pi^o$) masses. So that no corresponding enhancement is seen in the $\pi^-\pi^o p$ yield curve, at momenta around 1000 Mev/c.

On the other hand, for the $\pi^+\pi^- n$ channel, the roles are reversed. Thus, the differential cross-sections for the production of high ($\pi^+\pi^-$) masses are enhanced for the DD5 and FP5 waves, but suppressed for the SD1, DP3 and DD3 waves. So in the $\pi^+\pi^- n$ yield curve the peak at around 755 Mev/c is very much less pronounced, while there is a broad structure at higher momenta which is not present in the $\pi^-\pi^o p$ yield curve.

In a similar spirit, the ratio

$$dR = \left(\frac{d\sigma\,(\pi^+\pi^-)}{d\sigma\,(\pi^-\pi^o)} \right) \text{ for high dipion masses}$$

(section 4.4.3 and Fig.4.12) is greater than the corresponding ratio of the total cross-sections

$$R = \frac{\sigma\,(\pi^+\pi^-)}{\sigma\,(\pi^-\pi^o)}$$

at incident momenta greater than 755 Mev/c because of the same effect.

Of course to explain an experimentally observed Dalitz plot, the sum over all the inelastic partial waves would have to be made. Only waves with the same J and L will interfere in such a plot, but the DD3 and DP3 provide two such waves in this momentum region. This effect has been ignored, as has that of the σ (the I = J = 0 state, not necessarily a Breit-Wigner resonance, but a useful way of describing the $\pi\pi$ interaction with these quantum numbers as given by $\pi\pi$ phase shifts (34)). Several authors (22,28,35) have observed the need for such an effect in this momentum region to account for the peaking at high dipion masses in the $\pi^+\pi^-$ n channel. While there is still no consensus on the exact mass and width of the σ, widths of the order of 200 Mev/c^2 are favoured, to which this experiment would be insensitive. The σ would not of course affect the $\pi^-\pi^0$ p channel. The contribution of the I = 3/2 inelastic partial waves has also been ignored. Finally, and probably of most importance, the effect of the angular acceptance of the neutron counters has not been included in the arguments. In a full treatment, this would require that the integration of equation (5.8) be restricted to that range of solid angle in the c-system to which the neutron counters are sensitive. The effect of introducing such a restriction is, as yet, uncertain. However, the Monte-Carlo phase space calculations show that the angular acceptance of the counters is independent of incident momentum in this region, so the integration would be restricted to the same range at each momentum.

5.2 The Region Above 1 Gev/c.

It is worthwhile summarizing briefly the salient results for this momentum range, as derived in chapter four.

In what were essentially two quite independent experiments using the same 'yield curve technique', a narrow enhancement was observed in the $\pi^-\pi^0$ p channel (Figs.4.1 and 4.2); in neither was there a corresponding effect discernible in the $\pi^+\pi^-$ n channel.

The weight of evidence supported the contention that the enhancement was due to meson resonance production; its behaviour was certainly inconsistent with its interpretation as the formation of a nucleon resonance (Fig.4.16). The best mass and width for the resonance when produced close to its threshold ($p^* \simeq 30$ Mev/c) were found to be 765 and 35 Mev/c^2 respectively.

An understanding of this effect is still far from clear; in the following discussion several possibilities are examined.

The ρ is the well-established member of the nonet of vector mesons ($J^P = 1^-$) with isotopic spin 1. The negatively charged state has a branching ratio of almost exactly 100 % to $\pi^-\pi^0$, and could be expected to be detected in this experiment. However, the current listings (5) show that the ρ, although having a mass of 765 $\pm$ 10 Mev/c^2, has a width of 125 $\pm$ 20 Mev/c^2. The question naturally arises, therefore, as to whether what is observed in this experiment is the ρ meson, for some reason appearing narrow at its production threshold; or alternatively, is the enhancement due to a new, narrow meson resonance?

The ρ meson was first discovered in strong interactions of the type $\pi + p \rightarrow \rho + p$, $\rho \rightarrow \pi\pi$, at incident pion momenta (< 2 Gev/c) not very much greater than the minimum required for its production. In some of these experiments, at the lowest momenta, narrow structure has been observed in the effective mass of the dipion (36,37), at masses close to that accepted for the ρ meson. The difficulty here is that, for the 'conventional' ρ meson, with a mass of 765 and width 125 Mev/c^2, the effective mass of the meson would extend close to the limit available from phase space at these momenta. It is reasonable to suppose that, together with the accompanying problem of background subtraction (37), the effect of the phase space 'cut-off' is likely to make the ρ appear narrower than accepted. As higher incident momenta became available, the ρ meson was detected in many experiments with a width of about 125 Mev/c^2, although occasionally smaller values have been reported (38).

More indirect information concerning the production of the ρ meson close to its threshold has been furnished recently in attempts to understand single pion production with the 'isobar model' (31).

Thus two recent experiments (22,28) have been performed to investigate the reactions $\pi^- + p \rightarrow \pi^-\pi^0 p$ and $\pi^+\pi^- n$ at several incident momenta in the range 456 to 761 Mev/c (corresponding to centre-of-mass energies in the range 1337 to 1535 Mev) - that is well below the threshold for ρ -production, which occurs at an incident momentum of 1070 Mev/c (equivalent to 1710 Mev). Considering the production of only two isobars, the authors used a coherent addition of amplitudes of the form

$$\left| T \right|^2 = \left| T(\sigma \; n) + T(\pi^+\Delta^-) + T(\pi^-\Delta^+) \right|^2$$

for the neutron channel, and

$$\left| T \right|^2 = \left| T(\Delta^+\pi^-) + T(\Delta^0\pi^0) \right|^2$$

for the proton channel, where σ is an I = J = 0 object, and Δ is the $\Delta(1236)$ I = J = 3/2 nucleon resonance.

Their fits to the observed ($\pi^+\pi^-$) effective mass distribution were good, and in particular were able to account for the peaking at high dipion masses, first observed by KIRZ et al (35). However, there was a marked discrepancy between the data and the fit for the proton channel at incident momenta greater than 550 Mev/c.

This suggested that the inclusion of a P-wave amplitude was required in the model. The introduction of the ρ meson (I = J = 1) was an obvious candidate. This would affect the charged rather than the neutral dipion mass spectrum for two main reasons:

(1) from purely isotopic spin arguments, if the incident π^- p state

is dominated by the I = 1/2 component (expected to be valid in this momentum region (23)), then the ratio of the production cross-sections is

$$R = \frac{\sigma(\rho^{0} n)}{\sigma(\rho^{-} p)} = \frac{1}{2} = \frac{\sigma(\pi^{+}\pi^{-} n)}{\sigma(\pi^{-}\pi^{0} p)}$$

(for the I = 3/2 component this ratio R = 2);

(2) again from purely isotopic spin arguments, for production of the isobars via the I = 1/2 component, the interference effects between the ρ^{-} and the Δ^{+} and the Δ^{0} add for the proton channel, while for the neutron channel, the effects between the ρ^{0} and the Δ^{+} and the Δ^{-} subtract (for the I = 3/2 component, these interference effects both subtract).

In fact the Saclay Group re-analysed their results for the proton channel including an amplitude for ρ-production, obtaining considerably better fits to the data (22A).

The main conclusion from these analyses seems to be that the effects of the ρ^{-} meson are (indirectly) apparent at incident pion momenta well below its threshold.

Currently BRODY et al (24) are analysing data from the same reactions, in a centre-of-mass energy range of 1400 to 2000 Mev. The authors use a total amplitude involving the incoherent addition of four individual terms to fit the data from the neutron channel - namely T(ρ^{0} n), T($\pi^{+}\Delta^{-}$), T($\Delta^{+}\pi^{-}$), and T($\pi^{+}\pi^{-}$n), where the latter represents the phase space amplitude. Fig.5.3 shows the fraction of ρ^{0} required for their best fit to the data. As can be seen, at the threshold for ρ^{o} production (a centre-of-mass energy of 1710 Mev, or an incident momentum of 1070 Mev/c) a fraction compatible with 0 % is required: at 1740 Mev or 1126 Mev/c only 5.7 $\pm$ 1.7 % is needed.

The incoherent addition of similar individual amplitudes for the proton channel failed to produce satisfactory fits to the data.

On the basis of all these results (22,24,28), it seems reasonable to suppose that at incident pion momenta up to that required to produce the $\rho(765)$ at rest in the c-system, the production of the ρ^{o} is suppressed relative to the ρ^{-}, and the ratio R = 1/2 favoured.

Knowing the ratio of the production cross-sections, R, it is possible to predict the number of events, Y^{n}, expected in the neutron channel to correspond to the number, Y^{p}, seen at the centre of the enhancement in the $\pi^{-}\pi^{o}$ p yield curve generated from the cms gate (Fig.4.13), assuming ρ production to be its cause.

Thus assuming R = 1/2,

$$R = \frac{1}{2} = \frac{Y^{n} . f_2^{\,p} . 4}{Y^{p} . f_2^{\,n}}$$

or,

$$Y^{n} = \frac{1}{2} . \frac{1}{4} . \frac{f_2^{\,n}}{f_2^{\,p}} . Y^{p}$$

where $f_2^{\,n}/f_2^{\,p}$ is the ratio of the detection efficiencies for

FIG. 5.3

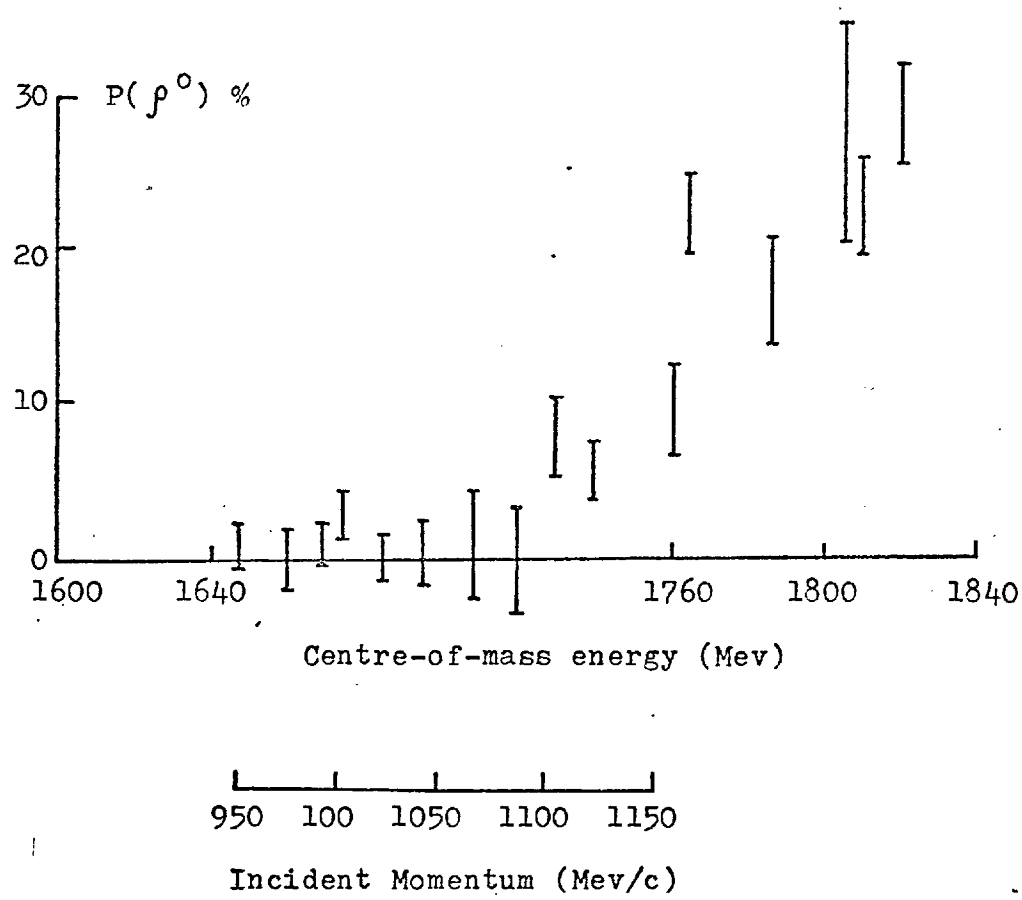

The percentage P(ρ^o) of ρ^o in the $\pi^+\pi^-$ n final state (from BRODY et al (24)).

the ($\pi^+\pi^-$) and ($\pi^-\pi^o$) systems in the decay array. A factor of 4 is included to compensate for the detection efficiencies of the neutrons (25 % compared to the assumed value of 100 % for proton detection).

From the Monte-Carlo (section 3.3) the ratio $f_2^n/f_2^p = 223/175$, and from the data (Fig.4.13) $Y^p \simeq 50$ events, giving $Y^n \simeq 8$ events. This number of events would be extremely difficult to detect with the present level of statistics. (On the other hand, if R = 2, then $Y^n \simeq 32$ events, a number which should be detectable).

Two main conclusions can be drawn from the arguments presented so far in this section. Thus, assuming that the enhancement in the proton channel is due to a resonance with I = 1, and produced such that R = 1/2, (likely for the ρ^-), it is quite plausible that no corresponding effect is discernible in the neutron channel; however, since the tail of the ρ^- has been (indirectly) detected at energies well below its threshold, the observed enhancement, if due to ρ^- production, should appear much broader.

In view of this, some further tests have been made. Firstly, to ensure that results available from other channels did not provide convincing evidence that the observed enhancement was due to instrumental effects, the yield curves of various other final states were examined.* For example, the conservation of g-parity in strong interactions prevents a

* The selections of classifications used for the various final states are discussed in works in ref. 1.

resonance from decaying into both ($\pi^-\pi^0$) and ($\pi^-\pi^+\pi^-$) or ($\pi^-\pi^0\pi^0$). Thus Fig.5.4A shows the comparison between the yield curves for the $\pi^-\pi^0$ p and the ($\pi^-\pi^0\pi^0$ + $\pi^-\pi^+\pi^-$)p final states. No significant enhancement is seen in the curve for the three pion channels, and instrumental effects seem unlikely to be the cause of the enhancement in the $\pi^-\pi^0$ p channel.

Secondly, to ensure that the enhancement was not due to a resonance decaying into $\pi^-\eta$, the yield curve of the $\pi^-\eta$ p channel was examined. This channel has the same signature in the decay array as $\pi^-\pi^0$ p , except for the differences in the azimuthal cuts applied to the raw data during analysis, as discussed in section 3.4.1. If a resonance decays into $\pi^-\eta$, there should be a large enhancement in the $\pi^-\eta$ p channel. Fig.5.4.B shows the yield curve, and there is a small enhancement at the same momentum as in the $\pi^-\pi^0$ p curve. But recalling from section 3.4.1 that some 10 % of $\pi^-\pi^0$ events 'feed-through' into the classification of $\pi^-\eta$ during analysis, the observed small enhancement is compatible with this effect. It is clear that the enhancement in the $\pi^-\pi^0$ p yield curve is not due to a $\pi^-\eta$ resonance.

Thirdly, the $\pi^0\pi^0$ n channel was studied. From isotopic spin arguments, an I = 1 resonance cannot decay into two neutral pions. Fig.5.4C shows the yield curve of this channel; the data points in the momentum channels where the ω meson is produced have been removed. (This is because during analysis the classification 000030 (three gamma-rays

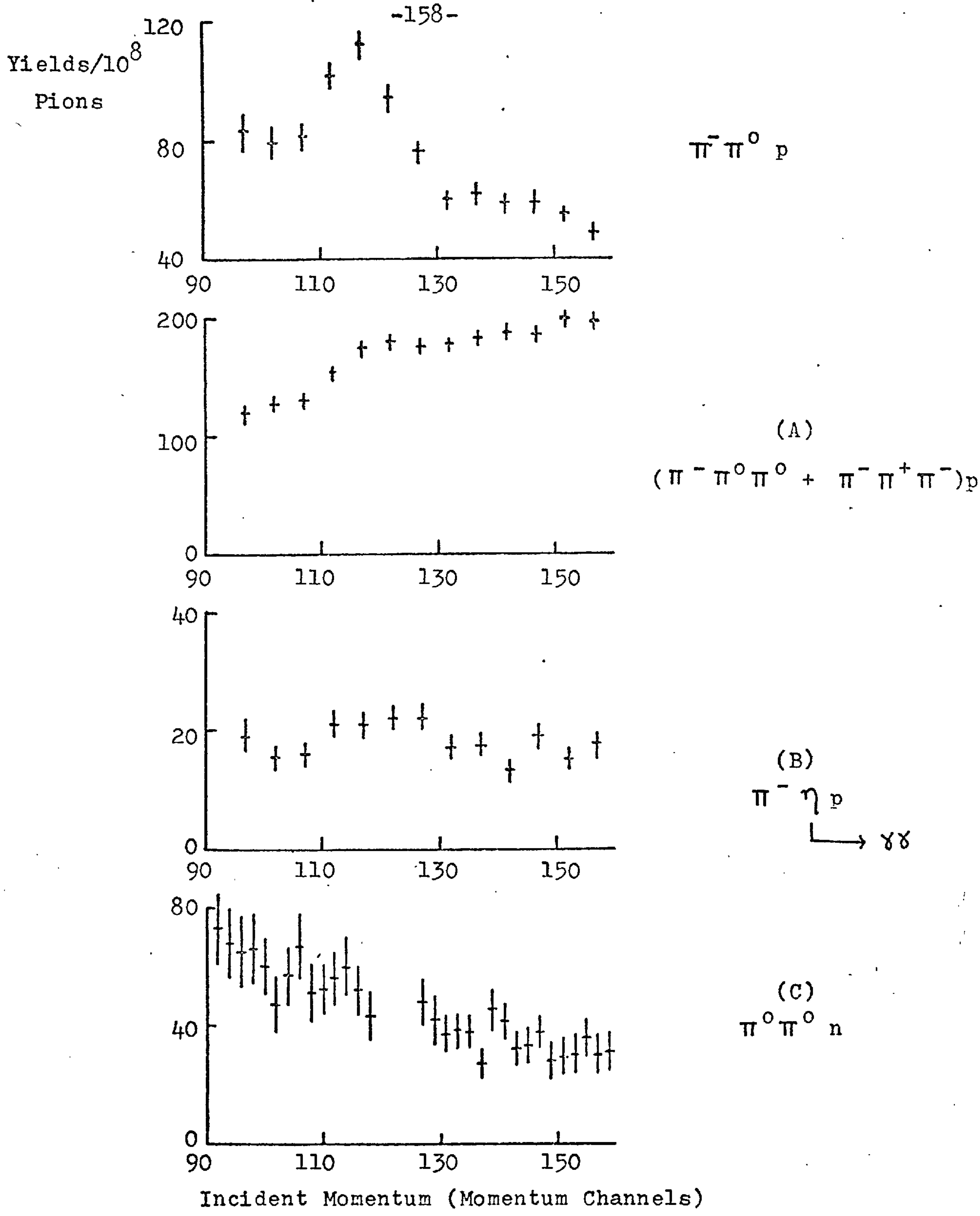

FIG. 5.4

Yield Curves generated from the cms gate for various final states.

detected) is used since it includes events from the $\pi^0\pi^0$ decay, as there is a significant probability that only three of the four gamma-rays are detected in the decay array: since the meson has approximately a 10 % branching ratio to $\pi^0\gamma \longrightarrow 3\gamma$, it appears in the $\pi^0\pi^0$ n yield curve.) But again, as can be seen, there is no discernible enhancement in this channel.

So from such tests on the data, it seems reasonable to assert that the observed enhancement is a genuine resonant effect in the $\pi^-\pi^0$ p channel.

Finally, mechanisms have been sought which could explain possible narrowing effects of the width of the ρ meson.

ADAIR (39) has investigated how final state interactions might affect the measured values of resonance parameters such as mass and width. Such interactions are likely to be important when, if c = 1,

$$\frac{p^*}{M} \cdot \frac{\hbar}{\Gamma} = \frac{n\,\hbar}{m_\pi} \qquad \text{for } n \simeq 1$$

where $\hbar / m_\pi$ is the typical interaction length, M is the mass, Γ the width, and p^* the momentum in the c-system of the resonance. In the cms gate, $p^* \simeq 30$ Mev/c , and for a mass and width of 765 and 125 Mev/c^2 respectively, then it follows that $n < 1$. So this experiment is sensitive to just that kinematic region where final state interactions might be important. However, as ADAIR (39) points out, the effect of this would seem to broaden the observed width of the resonance, in direct contrast to what is actually seen here, assuming ρ production.

As yet, no satisfactory explanation has been established to account for the observation of such a narrow width, if the enhancement is in fact due to the production of the ρ meson (although it has been claimed (though not explicitly calculated) that interference effects between resonances and coherent backgrounds can sometimes lead to the observation of narrower widths than expected (40)). In view of this, the presence of a new, narrow meson resonance, although unlikely, cannot be discounted.

5.3 Conclusions.

It is worthwhile to draw together the main conclusions from this work.

In the momentum region below 1 Gev/c, the behaviour of the enhancement seen in the $\pi^-\pi^0 p$ channel was able to be adequately explained by purely 's-channel' effects, using a 'phase space model'; it was inconsistent with meson production.

The enhancement was fitted by (i) a single Breit-Wigner resonance; and by (ii) a Breit-Wigner resonance and a straight-line background: the best fit was obtained by (ii) for a mass of 1520 Mev/c^2 , and a width of 120 Mev/c^2.

It was therefore tempting to associate this enhancement with the well-established D13(1520) nucleon resonance, which has a branching ratio of about 50 % to $\pi\pi N$ final states (5).

To explain the emergence of the enhancement (which is not seen in the total $\pi^-\pi^0 p$ cross-section), a simplified adaptation of the 'isobar model' (31) was used, assuming that the final states were produced via intermediate $\pi\Delta$ states. The enhancement was therefore fitted by the function $Y(p, t_{cms})$, representing a single Breit-Wigner resonance (of mass 1520 and width 120 Mev/c^2, the D13(1520) parameters) which was assumed to decay with a 100 % branching ratio into $\pi\Delta$ in its inelastic channel. Although this fit compared favourably with that for (i) above, it was poorer than that for (ii). Reasons for this might include both the neglect of any background present, and the fact that the D13(1520) almost certainly does not have a branching ratio of 100 % to $\pi\Delta$ states in its inelastic channel. However, the emergence of the observed enhancement could tentatively be explained using this model, since it required the suppression of the production of high dipion masses in the proton channel for the inelastic contribution of the D15(1670) and F15(1690) partial waves (it is high dipion masses to which this particular experiment is sensitive). In a similar spirit, the general features of the yield curves could tentatively be explained.

At this stage it has not been possible to distinguish between the D13(1520) and the S11(1535) resonances, both of which have enhanced inelastic cross-sections for the production of high $\pi^-\pi^0$ masses according to this model. The fact that the best fit to the enhancement was obtained for a mass of 1520 Mev/c^2

was thought to reflect the fact that the D13(1520) resonance has a 50 % branching ratio to $\pi\pi N$ states, while the S11(1535) decays predominantly to ηN final states in its inelastic channel (27).

The interpretation of the enhancement seen in the $\pi^- \pi^0 p$ channel in the momentum region above 1 Gev/c is still uncertain. Although the weight of evidence supported the fact that the enhancement was due to meson production, there were inconsistencies with this interpretation. If the cause is in fact meson production, the observed narrow width of the enhancement needs further investigation. While an explanation in terms of the ρ meson, for some reason appearing narrow at its threshold, is a possibility, the presence of a new, narrow meson, although unlikely, cannot at present be discounted.

Clearly there is a need for further data to be taken, to determine whether the present inconsistencies are the results of statistical variations, or whether the observed effect is more complicated than currently believed.

REFERENCES

1. a. D.M. Binnie et al, Phys. Letters 36B (1971) 257; (A_2^-).

   b. D.M. Binnie et al, Phys. Letters 36B (1971) 537; (A_2^-).

   c. D.M. Binnie et al, Paper presented at the Amsterdam Conference on Elementary Particles (1971); (ω).

   d. P.N. Upadhyay, Ph.D. Thesis, Physics Department, Imperial College, London University (1971); (δ^-).

   e. I. Siotis, Ph.D. Thesis, Physics Department, Imperial College, London University (1971); (A_2^-).

   f. M. Lewis, Ph.D. Thesis, Physics Department, Imperial College, London University (1971); (A_2^-).

2. B.C.Maglic, Spring School of Elementary Particle Physics, Yerevan, U.S.S.R. (1965);
   B.C. Maglic and G. Costa, Phys. Letters 18 (1965) 185.

3. W.G. Jones, Ph.D. Thesis, Physics Department, Imperial College, London University (1966).

4. R.J. Plano, Rapporteur's Review Talk, International Conference on High Energy Physics, Kiev, U.S.S.R. (1970).

5. Particle Properties, Reviews of Modern Physics, 43 No. 2 (1971).

6. W.G. Jones et al, Phys. Letters 23 (1966) 597.

7. A. Donnachie, Proceedings of the CERN School of Physics, Loma-Koli, Finland (1970).

8. M.G. Olsson and G.B. Yodh, Phys. Rev. 145 No. 4 (1966) 1309; a compilation of experimental data is given in this reference;
M. De Beer et al, Nuc. Phys. B12 (1969) 599;
N.M. Cason et al, Phys. Rev. 150 (1966) 1134;
S. Fermino et al, Nuovo Cimento 52A (1967) 892;
L. Bertanza et al, Nuovo Cimento 44A (1966) 712;
F. Bulos et al, Phys. Rev. 187 No. 5 (1969) 1827.

9. Particle Data Group, UCRL-20030 (1970); a compilation of N Partial Wave Amplitudes.

10. R.D. Field, Jr., UCRL-20616 (1971); submitted to Phys. Lett. B.

11. S.W. Kormanyos et al, Phys. Rev. 164 No. 5 (1967) 1661;
P.J. Duke et al, Phys. Rev. 149 (1966) 1077.

12. 'Tramp', NIRL/M/21 and NIRL/M/44; 'Ipso Facto', RHEL/R/103, Rutherford Laboratory.

13. J.G. Wilson, Ph.D. Thesis, Physics Department, Imperial College, London University (1970).

14. D.M. Binnie and A. Duane, Nucl. Inst. and Meth. 77 (1970) 329.

15. D.G. Crabb et al, Nucl. Inst. and Meth. 48 (1967) 87.

16. M.E. Kay, Internal Paper, Imperial College.

17. See, for example, G. Stephenson, Mathematical Methods (Longman) pg. 232.

18. R.G. Kirsopp, Ph.D. Thesis, Department of Physics, University of Edinburgh (1968).

19. D. Morgan, Phys. Rev. 166 No. 5 (1968) 1731.

20. A. Brandstetter, Program MIXFIT, Rutherford Laboratory.

21. C. Vittitoe et al, Phys. Rev. 135B (1964) 232.

22. M. De Beer et al, Nuc. Phys. B12 (1969) 599;

22.A. Nguyen Thuc Diem et al, Paper 5a-8, Part I, presented at the International Conference on High Energy Physics, Kiev, U.S.S.R. (1970).

23. M.G. Olsson and G.B. Yodh, Phys. Rev. 145 No. 4 (1966) 1309.

24. A.D. Brody et al, SLAC-PUB UCRL-2085 (1971).

25. Program LSQFIT, E202, CERN Program Library.

26. See, for example, P. Bareyre et al, Phys. Rev. 165 (1968) 1730; further references are also given here.

27. See, for example, B. Carreras and A. Donnachie, Nuc. Phys. 168 (1970) 35;
A. Davies and R. Moorhouse, presented at the International Conference on High Energy Physics, Vienna, Austria (1968).

28. D.H. Saxon et al, Phys. Rev. 2D (1970) 1790.

29. M. De Beer et al, Nuc. Phys. B12 (1969) 617;
P. Chavanon et al, Paper 5a-8, Part II, presented at the International Conference on High Energy Physics, Kiev, U.S.S.R. (1970).

30. M.G. Bowler and R.J. Cashmore, Nuc. Phys. B17 (1970)

31. S.J. Lindenbaum and R.J. Sternheimer, Phys. Rev. 123 (1961) 333;

31. cont. M.G. Olsson and G.B. Yodh, Phys. Rev. Lett. 10, (1963) 353; and Phys. Rev. 145 (1966) 1309;
B. Deler and G. Valladas, Nuovo Cimento 45A (1966) 559;
P. Chavanon et al, Nuovo Cimento 63A (1969) 1035.

32. D.H. Saxon, Ph.D. Thesis, Jesus College, University of Oxford.

33. B. Deler and G. Valladas, Nuovo Cimento 45A (1966) 559.

34. J.P. Baton et al, Nuc. Phys. B3 (1967) 349.

35. J. Kirz et al, Phys. Rev. 130 (1963) 2481;
R.A. Burnstein et al, Phys. Rev. 137B (1965) 1044;
J.D. Oliver et al, Phys. Rev. 147 (1966) 932;
M. Banner et al, Phys. Rev. 166 No. 5 (1968) 1346.

36. E. Pickup et al, Phys. Rev. Lett. 7 (1961) 192.

37. H. Foelsche et al, Paper presented at the International Conference on High Energy Physics, CERN, Geneva, Switzerland (1962).

38. N.M. Cason, Phys. Rev. 148 (1966) 1282;
A. Accensi et al, Phys. Lett. 20 (1966) 557.

39. R.K. Adair, Rev. Mod. Phys., 37 No. 3 (1965) 473.

40. R.K. Adair, Rev. Mod. Phys., 33 (1961) 406.